

DOCTORAL THESIS

Thermal Stability and Electrical Resistivity of Ag Thin Films with  
Various Surface and Interface Layers

(種々の表界面層を用いた Ag 薄膜の熱的安定性と電気抵抗率)



KITAMI INSTITUTE OF TECHNOLOGY

DEPARTMENT OF MATERIALS SCIENCE AND ENGINEERING

ZHANG ZIYANG

(張 子洋)

March, 2013

# Contents

Chapter 1 Introduction.....	1
1.1 Characteristics of Ag.....	1
1.2 Application of Ag thin films in electronic devices.....	2
1.2.1 Application in metallization for ULSI.....	2
1.2.2 Application in transparent electrodes .....	4
1.3 Agglomeration of Ag thin film.....	5
1.3.1 Agglomeration behavior of Ag thin film .....	5
1.3.2 Agglomeration mechanism of Ag thin film .....	8
1.4 Previous solutions to agglomeration suppression .....	9
1.5 Purpose of this study.....	13
Chapter 2 Experimental Procedure.....	15
2.1 Preparation method of specimen.....	15
2.1.1 Film deposition .....	15
2.1.2 Annealing.....	16
2.2 Characterization methods.....	16
2.2.1 Film thickness.....	16
2.2.2 Surface morphology .....	19
2.2.3 Electrical resistivity .....	21
2.2.4 Chemical bonding state .....	22
2.2.5 Adhesion strength .....	23
2.2.6 Crystal structure.....	25
Chapter 3 Effects of Ti Surface Layer and Interface Layer on Thermal Stability and Electrical Properties of Ag Thin Film.....	27
3.1 Introduction.....	27
3.2 Experimental procedure .....	27
3.3 Ag film with Ti surface layer (Ti/Ag film).....	28
3.3.1 Surface morphology .....	28
3.3.2 Electrical resistivity .....	31

3.3.3 Chemical bonding state of the surface.....	32
3.3.4 Crystal structure.....	34
3.4 Ag film with Ti interface layer (Ag/Ti film) .....	37
3.4.1 Surface morphology .....	37
3.4.2 Electrical resistivity .....	39
3.4.3 Adhesion Strength of Ag/Ti Film to SiO <sub>2</sub> Substrate.....	39
3.4.4 Crystal structure.....	40
3.5 Ti/Ag/Ti triple-layer film .....	46
3.5.1 Surface morphology .....	46
3.5.2 Electrical resistivity .....	47
3.6 Summary .....	48
Chapter 4 Effects of Nb Surface Layer and Interface Layer on Thermal Stability and Electrical Properties of Ag Thin Film and Optimization for Multilayered Structure of Ag Thin Film .....	49
4.1 Introduction.....	49
4.2 Experimental procedure .....	49
4.3 Ag film with Nb surface layer (Nb/Ag film).....	50
4.3.1 Surface morphology .....	50
4.3.2 Electrical resistivity .....	52
4.3.3 Mechanism of agglomeration suppression caused by Nb surface layer .....	53
4.3.4 Crystal structure.....	56
4.4 Ag film with Nb interface layer (Ag/Nb film) .....	59
4.4.1 Surface morphology .....	59
4.4.2 Electrical resistivity .....	61
4.4.3 Adhesion strength of Ag/Nb film to SiO <sub>2</sub> substrate.....	62
4.4.4 Crystal structure.....	63
4.5 Nb/Ag/Nb triple-layer film .....	68
4.5.1 Surface morphology .....	68
4.5.2 Electrical resistivity .....	69
4.6 Optimization for triple-layer structure .....	70
4.7 Summary .....	72

Chapter 5 Effects of Pd Surface Layer and Interface Layer on Thermal Stability and Electrical Properties of Ag Thin Film.....	73
5.1 Introduction.....	73
5.2 Experimental procedure .....	74
5.3 Ag film with Pd surface layer (Pd/Ag film).....	75
5.3.1 Surface morphology .....	75
5.3.2 Electrical resistivity .....	76
5.3.3 Chemical bonding state of the surface.....	77
5.3.4 Morphological stability of Pd .....	78
5.3.5 Solid solubility of Pd in Ag film.....	79
5.4 Ag film with Pd interface layer (Ag/Pd film) .....	81
5.4.1 Surface morphology .....	81
5.4.2 Electrical resistivity .....	82
5.4.3 Adhesion strength of Ag/Pd film to SiO <sub>2</sub> substrate .....	83
5.4.4 Crystalline orientation of Ag(111) for Ag/Pd film.....	84
5.4.5 Solid solubility of Pd in Ag film.....	85
5.5 Summary .....	87
Chapter 6 Effects of Ni Surface Layer and Interface Layer on Thermal Stability and Electrical Properties of Ag Thin Film.....	89
6.1 Introduction.....	89
6.2 Experimental procedure .....	90
6.3 Ag film with Ni surface layer (Ni/Ag film) .....	91
6.3.1 Surface morphology .....	91
6.3.2 Electrical resistivity .....	92
6.3.3 Chemical bonding state of the surface.....	93
6.3.4 Cohesive energy and morphological stability of Ni .....	95
6.3.5 Crystal structure.....	96
6.4 Ag film with Ni interface layer (Ag/Ni film).....	97
6.4.1 Surface morphology .....	97
6.4.2 Electrical resistivity .....	98
6.4.3 Adhesion strength of Ag/Ni film to SiO <sub>2</sub> substrate .....	100

6.4.4 Crystal structure.....	101
6.6 Summary .....	104
Chapter 7 Appropriate Surface Layer and Interface Layer for Structure-Modification of Ag Thin Film .....	105
7.1 Introduction.....	105
7.2 Appropriate surface layers .....	105
7.2.1 Comparison of surface layers .....	105
7.2.2 Prediction of appropriate surface layer.....	109
7.2.3 Verification of the prediction .....	110
7.2.4 Summary.....	113
7.3 Appropriate interface layers .....	114
7.3.1 Comparison of interface layers.....	114
7.3.2 Summary.....	118
Chapter 8 Research Summary and Conclusion .....	119
8.1 Research summary .....	119
8.2 Conclusion .....	121
References .....	123
Achievements of this research.....	133
Acknowledgments .....	135

# Chapter 1 Introduction

## 1.1 Characteristics of Ag

Ag is a very ductile, malleable, monovalent metal, with a brilliant white metallic luster. Some physical properties is listed in Table 1.1.<sup>1-3)</sup> As for the chemical properties, Ag is very difficult to be oxidized in the atmosphere at room temperature, and a thin layer of Ag oxide can not form in the atmosphere until the heating temperature reaches 200 °C.<sup>3)</sup> However, among the noble metals, the chemical activity of Ag is the highest, because it is easy to be corroded by some acid, such as HCl and H<sub>2</sub>S.<sup>1, 4)</sup>

Table 1.1 Some physical properties of Ag.

Atomic number	47
Atomic weight	107.87
Melting point	961.9 °C
Boiling point	2260 °C
Electrical resistivity (293 K)	1.59 μΩ cm
Thermal conductivity	419 Wm <sup>-1</sup> K <sup>-1</sup>
Crystal structure	face-centered cubic (fcc)
Interplanar spacing of the close-packed plane (111)	0.29 nm

Here, we are going to highlight the extreme properties of Ag, which determine the superiority of its application in electronic devices and optical devices. One is that Ag has the lowest resistivity of any metal. Therefore, the application of Ag thin films in the electrode and metallization materials has attracted much attention.<sup>5-18)</sup> The other is that Ag has the highest reflectance of any metal from the short wavelength region of visible to the far IR, and introduce less polarization into an optical system than do other metal.<sup>19, 20)</sup> Thus, Ag thin films are widely employed in various optical applications, such as low-emissivity coatings.<sup>21-27)</sup>

Unfortunately, the agglomeration of the Ag thin film (formation of separate parts

from a continuous film) occurring at high temperature, which loses its superior electrical and optical properties, is a severe obstacle for the application of the Ag thin films.<sup>28-33)</sup> Therefore, the improvement in the thermal stability of the Ag thin film has become the key point for the development of Ag thin film in electronics industry.

## 1.2 Application of Ag thin films in electronic devices

### 1.2.1 Application in metallization for ULSI

Since the mid-1980s, large-scale integrated circuits (LSI), very large-scale integrated circuits (VLSI), and ultralarge-scale integrated circuits (ULSI) have been rapidly developing.<sup>34)</sup> It follows that the application of metals and metal-like layers, which is called metallization, has become more important and stricter than ever.<sup>35)</sup>

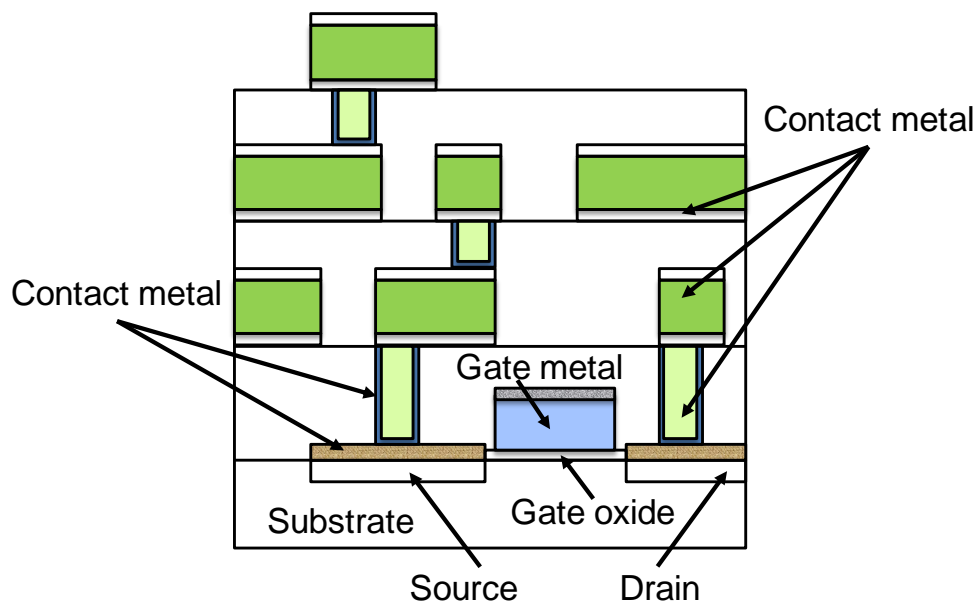


Fig. 1.1 Schematic cross section of a typical LSI.

Figure 1.1 shows a schematic cross section of a typical LSI.<sup>36)</sup> The metallization in LSI application is usually divided in two groups: (1) gate and (2) contact.<sup>37, 38)</sup> The characteristics of a LSI depend on several parameters of the metallization materials, among which the resistance-capacitance (RC) delay time is the most important.<sup>38~ 40)</sup>

The higher is the RC value, the lower is the operating speed of the device. The R and C are effective total resistance and capacitance of the device at the gate and interconnection level. S. P. Murarka has confirmed that the RC value is mainly dependent on the sheet resistance of conductor, the permittivity and the thickness of insulation layer, as shown in Eq. 1.1,<sup>38)</sup>

$$RC \propto R_s \varepsilon / t \quad (1.1)$$

where  $R_s$ ,  $\varepsilon$ , and  $t$  are the sheet resistance of conductor, the permittivity and the thickness of insulation layer, respectively. It is clear that the decrease in the thickness of insulation layer can increase the RC delay time with the sheet resistance of conductor being constant. In other words, the miniaturization of device scaling for the development of ULSI will bring about the RC delay time, but the most effective solution is to use the metallization materials with low resistivity.

In addition, resistance of the metal interconnections and contacts plays other indirect undesirable roles.<sup>35, 38)</sup> The lower is the resistance, the lower are the heat generation and the electromigration. Both of these phenomena are becoming key issues in devices and circuits where further miniaturization is pushing current densities upward. Current densities are expected to be at least an order of magnitude higher compared to those experienced today. They affect both the device performance and their reliability.

The above considerations show that, for the best results, the low-resistivity metal should be used as the metallization material. Al has been used as metallization materials for LSI for a long time, caused by its low resistivity of 2.65  $\mu\Omega$  cm at 293 K, the excellent adhesion to insulating substrates, and high oxidation resistance by the ease of forming passivation layer. However, it has become apparent that aluminum metallization can no longer provide the required performance as it suffers from electromigration, stress induced migration, high resistance, and the use of low temperature environment.<sup>37, 41)</sup> Since the mid-1990s, the trend to replace the metallization materials of Al and Al-Cu with Cu has become apparent for ULSI applications, because of the lower resistivity of Cu ( $\rho = 1.67 \mu\Omega$  cm at 293 K), higher resistance to electromigration and stress induced migration, and higher upper limit of operating temperature.<sup>11, 37, 42)</sup> With the downscaling of ULSI, the demand for the resistivity of the metallization materials is going up. Taking into account the arguments

supporting from the change from Al to Cu, Ag also appears to be a promising candidate, because Ag possesses a higher oxidation resistance and an even lower resistivity than Cu, and has high resistance to electromigration and stress induced migration as well as Cu.<sup>37, 43)</sup>

### 1.2.2 Application in transparent electrodes

Transparent conducting oxides (TCOs) are a unique class of material that exhibits both high transparency and high conductivity.<sup>44)</sup> TCO layers are essential components for a large variety of photosensitive electronic devices, mainly acting as transparent electrodes in flat panel display, touch screens, thin film solar cells, and electrochromic devices.<sup>45, 46)</sup>

At present, tin-doped indium oxide (ITO), dominates the market in high-end electronics, and it constitutes the most common usage of indium. This is due to the extraordinary combination of optical and electrical properties of ITO: low resistivity ( $\sim 1 \times 10^{-4} \Omega \text{ cm}$ ) and high optical transmittance ( $\sim 85\%$ ).<sup>47)</sup> However, the limited resources of indium on earth and the expensive cost of this material lead to the reduction of the quantities employed for films fabrication or even the replacement of ITO by other materials with equivalent properties. The thickness of ITO thin films used as transparent electrodes for optoelectronic devices ranges from 150 nm to 700 nm in general. The reduction of the thickness under 150 nm is not possible in the case of single oxide films, due to the increase of the sheet resistance with the thickness decrease caused by the classical size effect.

To solve this problem, it has been proposed that a significant drop in indium consumption by reduction of the ITO layer thickness could be obtained by combination with intermediate layers of other very thin metal films, namely ITO/metal/ITO multilayered structures.<sup>48-51)</sup> Ag, of course, has become the first choice for the intermediate layer, owing to the lowest resistivity of Ag among all the metals and the excellent transmittance of very thin Ag films.<sup>49, 52)</sup> Indeed, ITO/Ag/ITO structures have allowed the achievement of sheet resistances below  $5 \Omega/\text{square}$  and a visible transmittance above 85% with overall thickness below 100 nm.<sup>8, 50, 53)</sup>

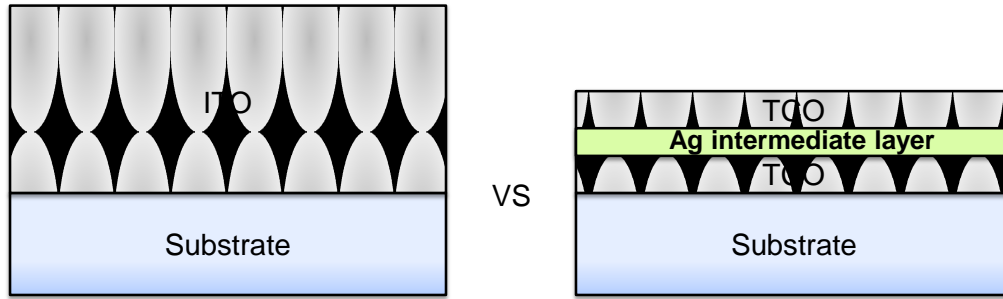


Fig. 1.2 Schematic illustration of ITO and TCO/Ag/TCO.

In addition, other TCO/Ag/TCO structures with less than 100 nm thickness, such as ZnO/Ag/ZnO, Al:ZnO/Ag/Al:ZnO, InZnO<sub>x</sub>/Ag/InZnO<sub>x</sub>, and InZnSnO<sub>x</sub>/Ag/ InZnSnO<sub>x</sub>, have also achieved the sheet resistance below 5 Ω/square and the transmittance above 85%.<sup>7, 9, 54-56)</sup> Therefore, the substitution of ITO by alternative TCOs becomes easier by using TCO/Ag/TCO structures, because the very thin Ag intermediate layer can decrease the overall resistivity even though the resistivity of these TCOs is not as low as that of ITO. Figure 1.2 presents the schematic diagrams of ITO and TCO/Ag/TCO.

### 1.3 Agglomeration of Ag thin film

#### 1.3.1 Agglomeration behavior of Ag thin film

The agglomeration behavior of Ag thin film is mainly represented by the formation and growth of the voids and hillocks. The severe agglomeration will make the film discontinuous, and then significantly change the electrical and optical properties of the Ag thin films. The following describes the agglomeration behavior and its effect on the electrical resistivity.

Figure 1.3 shows the SEM images of the Ag (100 nm) film before and after annealing. The as-deposited Ag film exhibits a smooth surface. After annealing at 500 °C, a lot of small voids and hillocks are formed, and distributed evenly on the surface. With increasing the annealing temperature to 600 °C, it is found that the Ag film has been suffering from a severe agglomeration. The number of the voids increases, and the size becomes larger. Most of the voids have joined with each other to form islands, and complete agglomeration has ultimately resulted.

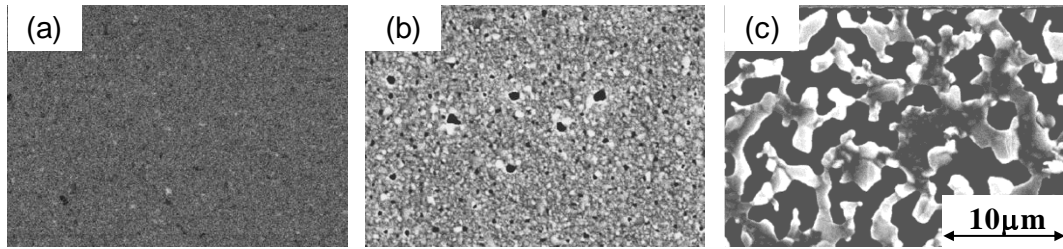


Fig. 1.3 SEM images of the Ag (100 nm) films before and after annealing. (a) As-deposited Ag film, (b) Ag film after annealing at 500 °C, and (c) Ag film after annealing at 600 °C.

Then, AFM observation has been carried out to further study the depth of the voids and the rms surface roughness of the agglomerated Ag film. Figure 1.4 gives AFM line profiles of the voids in the Ag (100 nm) films after annealing at 500 °C and 600 °C. The depth of the voids formed at 500 °C and 600 °C is about 40 and 100 nm, respectively. The height of the hillocks formed at 500 °C and 600 °C is about 40 and 100 nm, respectively. It is suggested that the agglomeration during annealing at 500 °C is not dramatic so that the voids are not deep enough to reach to the substrate. However, after annealing at 600 °C, the serious agglomeration makes the substrate partially exposed.

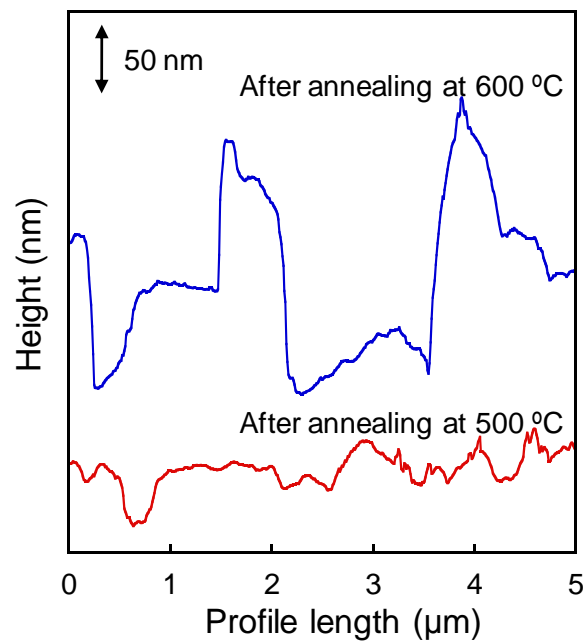


Fig. 1.4 AFM line profiles of the Ag (100 nm) films after annealing at 500 °C and 600 °C.

Table 1.2 shows the rms roughness of the surfaces of the Ag (100 nm) film before and after annealing. It is indicated that the surface of the Ag film has become rougher owing to the development of agglomeration with increasing the annealing temperature.

Table 1.2 The surface roughness of the Ag (100 nm) films before and after annealing.

	Rms roughness (nm)		
	As-deposited	500 °C	600 °C
Pure Ag film	4.7	12.2	29.0

Figure 1.5 shows the change in the resistivity of the Ag (100 nm) film as a function of annealing temperature. The resistivity of the Ag film decreases from 2.7 to 1.9  $\mu\Omega$  cm, which is close to the bulk resistivity of Ag. This reduction of resistivity is due to the still-continuous surface and the improvement in crystallinity. However, the severe agglomeration occurring at 600 °C, as show in Fig. 1.3, reduces the conduction area for electrons, which leads to the abrupt increase of resistivity. Therefore, in order to make good use of the Ag thin films in electronics industry, it is necessary to solve the agglomeration problem of Ag thin films.

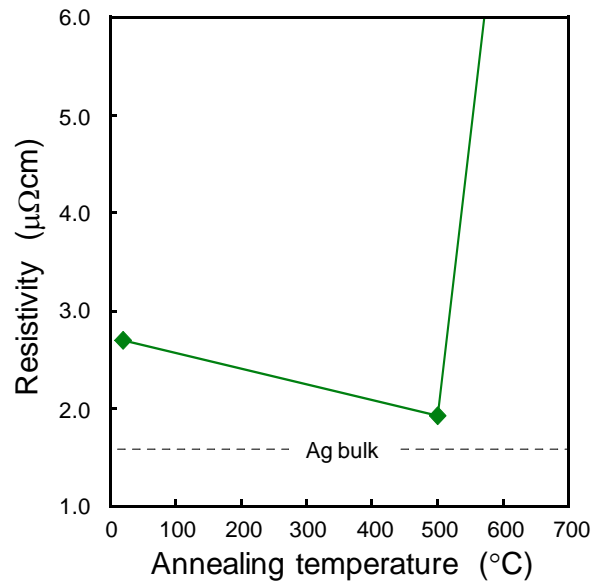


Fig. 1.5 Resistivity of the Ag (100 nm) film as a function of annealing temperature.

### 1.3.2 Agglomeration mechanism of Ag thin film

The agglomeration mechanism of Ag thin film has been discussed for decades.<sup>57-66)</sup> Although the process of Ag agglomeration is complicated, the key factors in causing the agglomeration of Ag thin film are summarized as follows.

Firstly, the surface diffusion dominates the occurrence and development of the agglomeration of Ag film. Early in the late 1970s and early 1980s, S. K. Sharma<sup>57-59)</sup> presented that hillock growth as a result of thermal stress relaxation by diffusion creep and by the surface diffusion of silver atoms, and void growth is a process of achieving a minimum energy configuration by surface diffusion. Over the past decades, this viewpoint has also been confirmed by other groups. R. Dannenberg<sup>60, 61)</sup> used the in-situ TEM, in which the heating stage was capable of reaching 1300 °C and stored in high vacuum, to observe the microstructural change of Ag thin film with increasing the heating temperature. Their results support surface diffusion as the mass transport mechanism for grooving, void formation, and grain growth. H. C. Kim<sup>62)</sup> worked out an activation energy ( $0.32 \pm 0.02$  eV) for the onset of agglomeration in Ag thin films on SiO<sub>2</sub> ramped at a rate of 0.1 °C /s, using an Arrhenius relation in terms of onset temperature and film thickness. The value is consistent with the activation energy for surface diffusion of Ag in a vacuum, which is believed to be the dominant mechanism for agglomeration of Ag thin film. Therefore, the ease of Ag atom migration at high temperature causes the ease of Ag agglomeration.

Secondly, the poor adhesion of the Ag thin film to the silicon dioxide (SiO<sub>2</sub>) or glass substrate is considered to be another major cause of agglomeration. It is well known that the higher is the free energy of oxide formation for the metal films, the stronger is the adhesion between the films and the SiO<sub>2</sub> or glass substrates.<sup>67)</sup> Indeed, Ag with low free energy for oxide formation ( $\Delta_f G^\circ_{\text{Ag}_2\text{O}} = -11.2$  kJ/mol)<sup>68)</sup> presents very poor adhesion to the SiO<sub>2</sub> substrate. T. L. Alford<sup>62-64)</sup> has pointed out that the agglomeration is also driven by the minimization of the interfacial energy. The interfacial energy could be decreased by the improvement of the adhesion at the interface so that the driving force of agglomeration would reduce. This viewpoint has been confirmed by other research groups.<sup>65, 69)</sup> They inserted the highly oxidizable metal as interface layer, such as Al and Ti, to improve the adhesion strength of the Ag film to the SiO<sub>2</sub> substrate, and then it was

observed that the degree of agglomeration was reduced after annealing. Therefore, the improvement in the adhesion of the Ag thin film to the SiO<sub>2</sub> or glass substrate is helpful to improve the thermal stability of the Ag thin film.

Thirdly, the existence of non-(111) oriented grains in the Ag films deposited on the amorphous SiO<sub>2</sub> substrate promotes the growth of (111) oriented grains and the disappearance of non-(111) oriented grains at high temperature, followed by the growth of hillocks and voids. D. L. Smith<sup>70)</sup> has explained that the minimization of total surface energy is a driving force for the growth of the grains oriented with the close-packed plane. As we know, the close-packed plane of Ag is Ag(111), which has the lowest surface energy. Therefore, the atoms from non-(111) oriented Ag grains will be transferred to the grains which are oriented with (111) parallel to the substrate. This process reduces the energy of the system by reducing the surface energy of the Ag thin film, and results in agglomeration. H. C. Kim,<sup>66)</sup> Y. Minamide,<sup>31)</sup> and Z. Wang,<sup>65)</sup> have confirmed that highly (111) oriented Ag films obtain much higher thermal stability than the Ag films with random orientation.

#### **1.4 Previous solutions to agglomeration suppression**

Previously, alloying Ag thin films with other metallic elements has ever been a popular solution to improve the thermal stability of the Ag thin films.<sup>29-33, 71-74)</sup> This is, indeed, an effective way to suppress the agglomeration, and the preparation of alloy films is simple. Figure 1.6 shows the SEM images of the Ag (100 nm) films alloyed with different metal elements after annealing at 600 °C, which are selected from our previous data.<sup>29-31, 75)</sup> In comparison with the change in surface morphology of the pure Ag film as a function of annealing temperature, as shown in Fig. 1.3, it is found that the significant improvement in thermal stability of the Ag films has been achieved owing to the alloying elements.

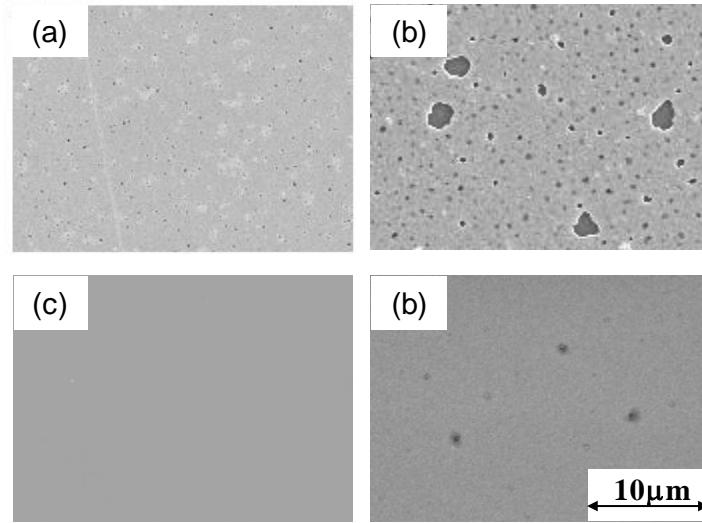


Fig. 1.6 SEM images of the films after annealing at 600°C. (a) Ag-Al (2.2 at%), (b) Ag-Cu (2.1 at%), (c) Ag-Nb (3.9 at%), and (d) Ag-Ti (1.4 at%).

By the AES or XPS analysis, it has been found that the alloying Al, Nb, and Ti, which are easy to be oxidized,<sup>68)</sup> formed oxide surface layers to suppress the surface diffusion of Ag atoms.<sup>29-31, 75)</sup> Especially, the alloying Al also formed oxide interface layer to improve the adhesion of the Ag film and SiO<sub>2</sub> substrate.<sup>29)</sup> By the XRD analysis, it has been found that, just like the Ag-Al films prepared by H. C. Kim,<sup>66)</sup> the Ag-Cu films also shows an extremely high volume fraction of Ag(111) and almost no change in crystalline orientation upon annealing.<sup>30, 31)</sup> These behaviors are considered to contribute to the agglomeration suppression, as discussed in Section 1.3.2.

However, a problem caused by alloying elements in Ag films has been discovered. Figure 1.7 shows the resistivity of the pure Ag film and the alloy films as a function of annealing temperature.<sup>29-31, 75)</sup> It is clear that a relative low content of other metals in the Ag films can cause an increase in resistivity. This phenomenon is considered to be attributed to the impurity scattering effect.<sup>76, 77)</sup> In general, the resistivity of an alloy film,  $\rho_{\text{film}}$ , is described by Eq. 1.2,<sup>77)</sup>

$$\rho_{\text{film}} = \rho_b + \rho_i \quad (1.2)$$

Where  $\rho_b$  is the bulk resistivity of the metal, and  $\rho_i$  is the resistivity caused by impurity scattering effect. Therefore, Ag film alloyed with other elements might lose the

low-resistivity superiority of Ag. When this solution is adopted, we need to be careful in the content of alloying elements to meet the growing requirement of resistivity.

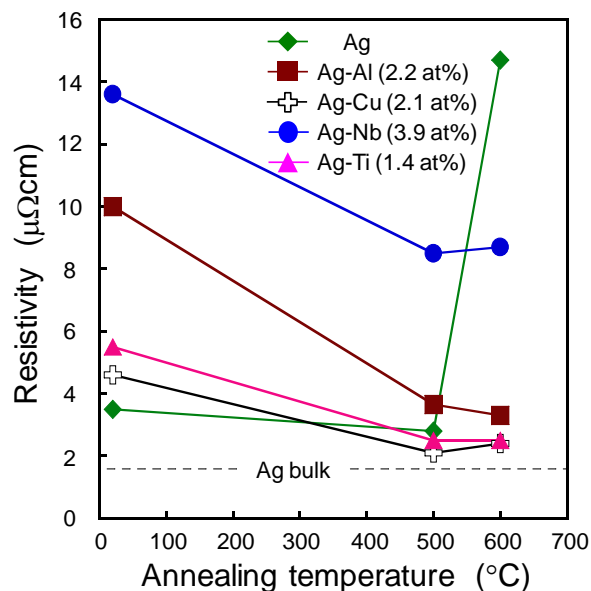


Fig. 1.7 Resistivity of the alloy films as a function of annealing temperature.

Recently, our group has reported that a multilayered structure of a pure Ag film sandwiched between very thin Al layers at the film surface and the interface with the SiO<sub>2</sub> substrate, namely Al/Ag/Al film, can obtain both high thermal stability and very low resistivity simultaneously.<sup>69, 78)</sup> Fig. 1.8 shows the SEM image of the Al (1 nm)/Ag (95 nm)/Al (1 nm) film after annealing at 600 °C. It is found that this annealed film exhibits a very smooth surface, which indicates the agglomeration of Ag film has been effectively suppressed.

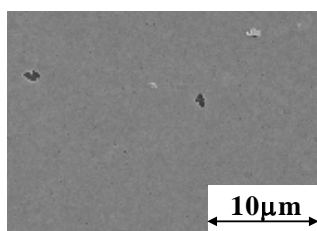


Fig. 1.8 SEM image of the Al (1 nm)/Ag (95 nm)/Al (1 nm) film after annealing at 600 °C.

Fig. 1.9 shows the resistivity of the Al (1 nm)/Ag (95 nm)/Al (1 nm) film as a function of annealing temperature. The as-deposited Al (1 nm)/Ag (95 nm)/Al (1 nm) film shows almost the same low resistivity as the as-deposited pure Ag film, which is much lower than the Ag-Al (2.2 at%) alloy film. This is because the main part of Ag in the multilayered film has not suffered from the impurity scattering effect. This multilayered film exhibits the same degree of lower resistivity after annealing at 500 °C and 600 °C, because of its high thermal stability and the improvement in crystallinity of Ag.

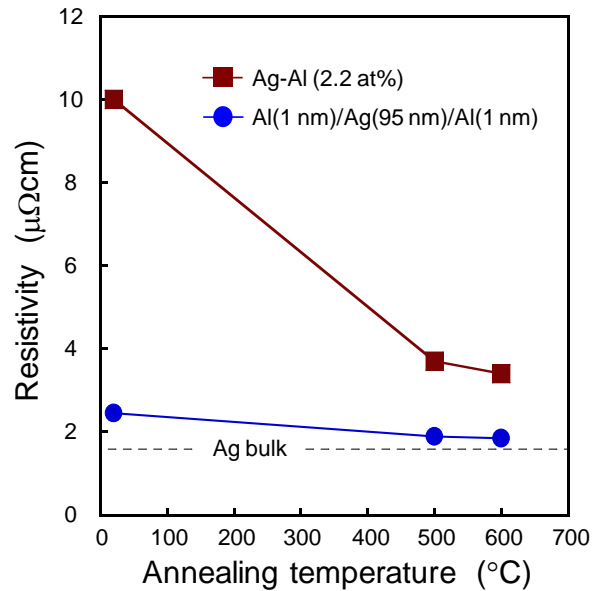


Fig. 1.9 Resistivity of the Ag-Al (2.2 at%) and Al (1 nm)/Ag (95 nm)/Al (1 nm) films as a function of annealing temperature.

This idea actually came from the agglomeration suppression mechanism of Ag-Al alloy film, as mentioned above. The Al surface layer and interface layer of the multilayered film not only improve the thermal stability of the Ag film, but also keep the main part of Ag layer chemically pure to maintain its low resistivity. This solution has provided a valuable reference for the development of Ag thin film technology.

## **1.5 Purpose of this study**

Since Al/Ag/Al film has shown excellent thermal stability and extremely low resistivity simultaneously, it is expected that some other metals, instead of Al, are also capable of achieving this goal with the same strategy. This dissertation focuses on improving the thermal stability of the Ag thin films and maintaining their low resistivity by modifying the Ag thin films with surface and interface layers, and then concludes the categories of metallic elements which are appropriate for the surface layer and interface layer of the Ag thin film.

Firstly, the effects of various metals as surface layer and interface layer on the thermal stability and electrical resistivity of the Ag thin films are investigated. The roles of various metals will certainly change owing to their different properties. After ascertaining their roles and effectiveness in the improvement of thermal stability and the maintenance of low resistivity, the appropriate surface layers and interface layers are selected, respectively, to compare their properties. Finally, the essential properties for appropriate surface layers and interface layers are summarized, and these properties can be used to categorize what elements are suitable to the surface layer or interface layer of the Ag thin film.



## Chapter 2 Experimental Procedure

### 2.1 Preparation method of specimen

#### 2.1.1 Film deposition

The films were deposited by RF magnetron sputtering apparatus (ANELVA L-250S-FH). A Si (001) wafer with a 100-nm-thick thermally grown SiO<sub>2</sub> layer was used as the substrate, and deposition was carried out without substrate heating during sputtering. The targets of Ag (purity 99.99%), Ti (purity 99.9%), Nb (purity 99.9%), Pd (purity 99.99%), Ni (purity 99.99%), and W (purity 99.99%) were used for sputtering. Figure 2.1 illustrates the internal structure of the sputtering chamber. Because there are three available cathodes inside the chamber, it is possible to sequentially prepare a double-layer film or a triple-layer film without breaking vacuum. The specific deposition condition for each layer has been described in Table. 2.1. The deposition procedure is as follows.

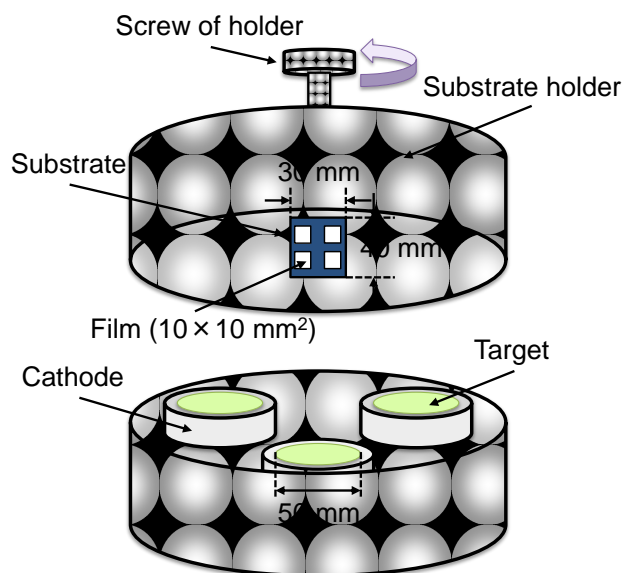


Fig. 2.1 Internal structure of sputtering chamber.

After the system was evacuated to below  $1.0 \times 10^{-5}$  Torr by the HiPace 300 turbo molecular pump, the substrate and chamber were baked at 450 °C for 6 hours to exclude the adsorbed gas.<sup>79)</sup> After cooling, gettering sputtering was carried out for 20 min with a Ti target to improve vacuum quality.<sup>80, 81)</sup> After the evacuation below  $1.8 \times 10^{-7}$  Torr, the Ar gas was introduced at a flow rate of 0.76 ml/min. Before the film deposition, pre-sputtering was implemented for 20 min to clean the surface of the target and stabilize the plasma. After pre-sputtering, the shutter was opened for the film deposition at room temperature.

Table 2.1 Deposition conditions for the layers of Ag, Ti, Nb, Pd, Ni, and W.

	Ag	Ti	Nb	Pd	Ni	W
RF power (W)	30	20	20	15	100	15
Ar gas pressure ( $\times 10^{-2}$ Torr)	1.0	1.0	1.0	1.0	2.8	1.0
Distance between target and substrate (mm)	55	55	55	55	40	55
Thickness (nm)	100	1~10	1~10	1~5	1~10	5

## 2.1.2 Annealing

Annealing of the films, at 500 or 600 °C, was carried out in a lamp-heating furnace under vacuum for 1 h after evacuation below  $1.0 \times 10^{-7}$  Torr. The heating rate and cooling rate were both set to 10 °C/min.

## 2.2 Characterization methods

### 2.2.1 Film thickness

#### 2.2.1.1 Thickness of surface layer or interface layer (Multiple reflection interference method)

The thickness of a thick film can be calculated by multiple reflection interference method.<sup>82)</sup> Figure 2.2 shows (a) a film masked with an Al reflective layer for thickness measurement, and (b) interference fringes observed by the method. The Al reflective layer on the sample was deposited by vacuum evaporation. Then, the interference

fringes were observed at the edge of the sample through ANELVA 911-9150 Nanoscope, as show in Fig 2.2. The thickness was calculated by Eq. 2.1,<sup>83)</sup>

$$t = (a / b) \cdot (\lambda / 2) \quad (2.1)$$

where  $a$  represents the spacing between two neighboring fringes,  $b$  represents the shift distance of a fringe caused by the step at the film edge, and  $\lambda$  represents the wavelength of the monochromatic light ( $\lambda = 546 \text{ nm}$ ), respectively.

The thickness of the surface layer or interface layer of the Ag film has been determined by multiplying the sputtering time by its deposition rate. The deposition rate of a film (more than 60 nm in this study) is calculated by dividing the thickness by the sputtering time.

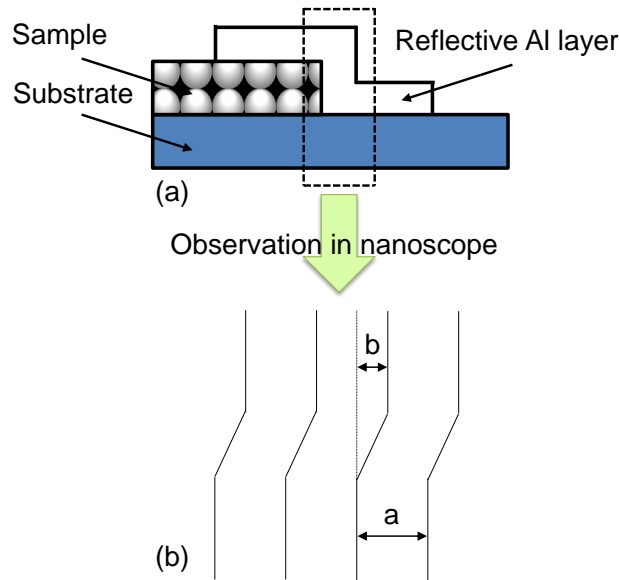


Fig. 2.2 Schematic diagram of multiple reflection interference method for thickness measurement. (a) an Al layer deposited on a testing film, and (b) interference fringes observed by the method.

### 2.2.1.2 Thickness of Ag film (XRF)

Although the thickness of the Ag film in every multilayered film is fixed to 100 nm for deposition according to the deposition rate, the Ag film can not be absolutely the same as thick as 100 nm for every deposition. Because the resistivity of the Ag films is

extra sensitive to the thickness of the Ag films, the thickness of the Ag part in every film has to be measured after sputtering in order to ensure the accuracy of the resistivity. Since the X-ray Fluorescence Analysis (XRF) is nondestructive testing,<sup>84)</sup> and it has been reported that the thickness of more than 100 nm thick films can also be accurately measured using XRF,<sup>85)</sup> XRF has been used to measure the thickness of the Ag films in this study.

When the X-ray with a certain wavelength irradiates the solid film, the fluorescent X-ray with the characteristic wavelength belonging to the element in the film radiates. According to the wavelength and intensity of the fluorescent X-ray, the thickness of the film that consists of the element can be accurately calculated by the fundamental-parameter (FP) method.<sup>86)</sup> In this study, the XRF apparatus model is BRUKER S8 TIGER, and the analysis conditions have been shown in Table 2.2. The concentration of Ag in the Ag parts of the multilayered films is set to 100%, and the density of Ag is set to 10.5 g/cm<sup>3</sup>. In the case of our study, K $\alpha$  radiation was used for the measurement of the thickness of the approximately 100-nm-thick Ag films. After XRF measurement, the FP quantitative analysis software automatically calculated the thickness of the Ag films. The values calculated through XRF analysis have been confirmed to be coincident with the values calculated by multiple reflection interference method.

Table 2.2 Measurement conditions for XRF.

	K $\alpha$
Target	Rh
Tube voltage	60 kV
Tube current	50 mA
Analyzing crystal	LiF 220
Collimator mask	Scintillation Counter
Atmosphere	Vacuum
Analysis mode	FP

## 2.2.2 Surface morphology

### 2.2.2.1 Scanning Electron Microscopy (SEM)

The surface morphology of the films was firstly observed using SEM (Model: JEOL JSM-5800). The basic components of the SEM are the lens system, electron gun, electron collector, cathode ray tubes, and the electronics associated with them.<sup>87)</sup> Figure 2.3 shows the schematic diagram of SEM. The SEM focuses an electron beam at a point on the surface of the sample, and then measures the resulting electrons with a detector. By doing this in a raster pattern across the surface, an image is formed, pixel by pixel. The column at the top of Fig. 2.3 mainly consists of the electron gun and lens system, where the electron beam is generated and focused. The electron beam coming from the column is also called the primary electrons. When the primary electrons impact the surface, they generate secondary electrons, backscattered electrons, Auger electrons, X-ray and cathode luminescence. In this study, the accelerating voltage was set to 20 keV, and the magnification varied from  $500 \times$  to  $10000 \times$  for observation.

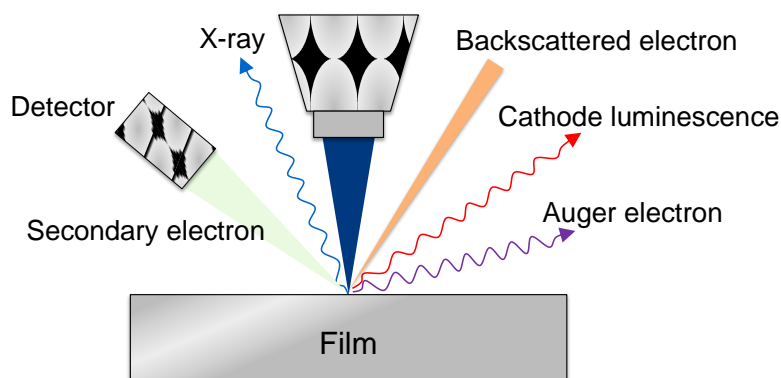


Fig. 2.3 Schematic diagram of SEM.

### 2.2.2.2 Atomic Force Microscopy (AFM)

The further observation of the surface morphology was carried out using AFM (Model: SHIMAZU SPM-9500J3), and then the rms surface roughness of the films was figured out. Figure 2.4 shows the schematic diagram of AFM. AFM is a powerful form of scanning probe microscopy (SPM) that performs its imaging function by measuring a local property of the surface, such as its height. AFM employs a probe or tip that is

positioned very close to surface to get these measurements. When the tip is brought into proximity of a sample surface, forces between the tip and the sample lead to a deflection of the cantilever according to Hooke's law.<sup>88)</sup> Depending on the situation, forces that are measured in AFM include mechanical contact force, van der Waals forces, capillary forces, chemical bonding, electrostatic forces, magnetic forces, etc. Then, the deflection is measured using a laser spot reflected from the top surface of the cantilever into an array of photodiodes. AFM operates in two modes, namely, contact mode imaging and non-contact mode imaging.<sup>89)</sup> In this study, the contact mode was selected, where the force between the tip and the surface is kept constant during scanning by maintaining a constant deflection.

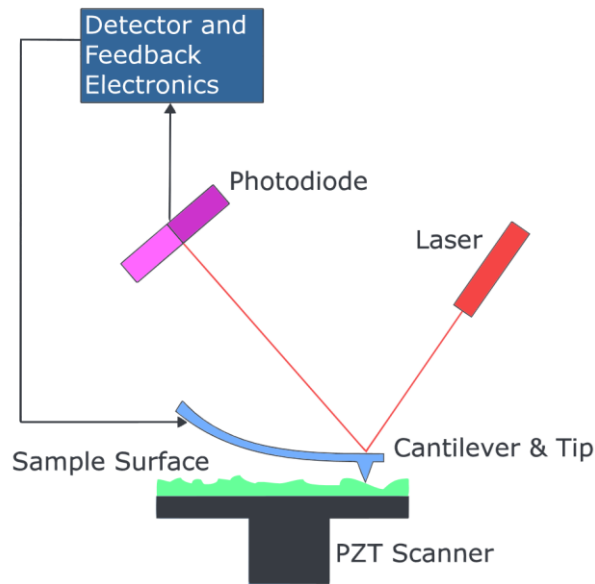


Fig. 2.4 Schematic diagram of AFM.

The rms surface roughness was calculated by Eq. 2.2,

$$Rms = \sqrt{\frac{\sum(Y_i - Y)^2}{N}} \quad (2.2)$$

where  $Y_i$  represents the height of the measured point at the surface,  $Y$  represents the average height of all the measured points, and  $N$  represents the amount of the measured points, respectively.

### 2.2.3 Electrical resistivity

For metals, the basic electrical property is the resistivity,  $\rho$  ( $\mu\Omega$  cm), of the bulk material, which is defined as the resistance,  $R$  ( $\mu\Omega$ ), of a 1-cm<sup>3</sup>-cubic material between the opposite faces. With thin films, it is more convenient to think in terms of the resistance of a film between the opposite edges, as shown in Fig. 2.5. As we know, the relationship between the resistance and the resistivity is shown as Eq. 2.3,

$$R = \frac{\rho y}{A} = \frac{\rho y}{bh} \quad (2.3)$$

where  $\rho$  is the resistivity of the film,  $y$  is the length of the film,  $A$  is the cross-sectional area of the conduction path,  $h$  is the film thickness, and  $b$  is the width of the film. If  $y = b$ , Eq 2.3 becomes

$$R_s = \frac{\rho}{h} \quad (2.4)$$

The resistance of a square of film is known as the “sheet resistance”,  $R_s$ , and is given in  $\mu\Omega/\text{square}$ .<sup>90)</sup> Therefore, if the film thickness  $h$  is known, and the sheet resistance  $R_s$  is measured, the resistivity  $\rho$  of the film will be calculated from Eq. 2.4.

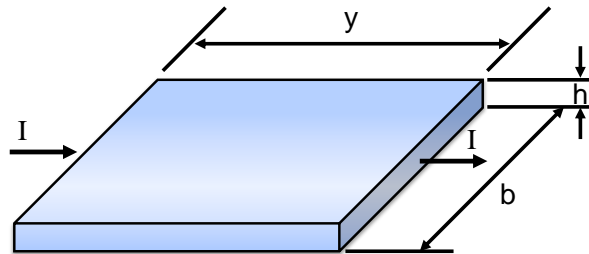


Fig. 2.5 Geometry defining the sheet resistance of a film of thickness  $h$ .

The value of  $R_s$  is conveniently measured with the four-point probe. Figure 2.6 shows the four-point probe for sheet resistance measurement. In this study, the  $\text{SiO}_2$  substrate is insulating so that the current,  $I$ , passes through the film. By measuring the voltage,  $V$ , with a different pair of probes than the pair used for current flow, the voltage associated with current flow through the contacts is removed from the measurement, and only the voltage drop across a distance  $d$  of film is measured. A correction coefficient,  $C$ , is added to Eq. 2.5 for the calculation of  $R_s$ .

$$R_s = C (V/I) \quad (2.5)$$

As shown in Fig. 2.6, if  $y$  and  $b$  are much longer than  $d$ ,  $C = \pi/\ln 2 = 4.53$ . If the relationship of  $y$ ,  $b$ , and  $d$  meets with  $y = b = 10d$ ,  $C$  is equal to 4.22.<sup>91)</sup> In the present study,  $C$  is 4.22.

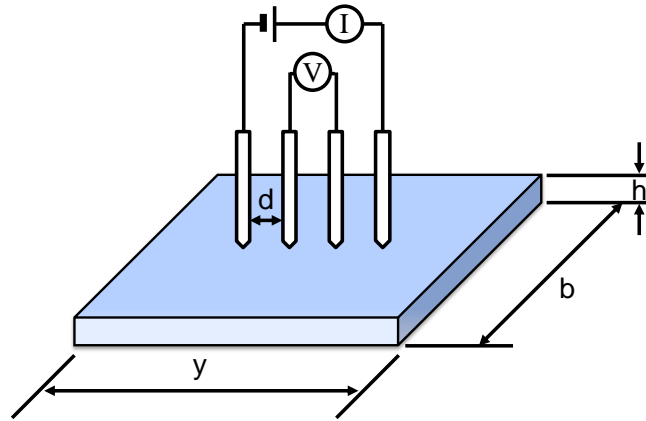


Fig. 2.6 Four-point probe for sheet-resistance measurement of a film on an insulating substrate.

### 2.2.4 Chemical bonding state

The chemical bonding state of the surfaces of the Ag films with the surface layers was investigated by X-ray photoelectron spectroscopy (XPS). The model of the XPS apparatus is PerkinElmer MODEL 1600, and the analysis conditions are listed in Table 2.3.

Table 2.3 Analysis conditions for XPS.

X-ray source	Monochromatic Al K $\alpha$ radiation ( $h\nu = 1486.6$ eV)
Power	150 W
Voltage	1.4 kV
Analysis area	$\Phi$ 800 $\mu$ m
Acceptance angle for signal	65 $^\circ$
Pass energy	23.5 eV

Photoelectron spectroscopy works by directing a beam of monoenergetic photons in

the direction of a sample. The photons have certain energy,  $h\nu$ , that when they hit electrons in the atoms of the sample, the electrons are ejected from the atoms with kinetic energy,  $E_{kin}$ . The electrons ejected are analyzed in the XPS detector by measuring electrons kinetic energy, which provides the information to determine the chemical bonding state of the elements at the surface, as shown in Eq. 2.6, <sup>92)</sup>

$$E_b = h\nu - E_{kin} - \phi_{sp} \quad (2.6)$$

where  $E_b$  is the bonding energy of bound electron, and  $\phi_{sp}$  is the work function of the spectroscope. Figure 2.7 illustrates the schematic representation of X-ray photoelectron process.

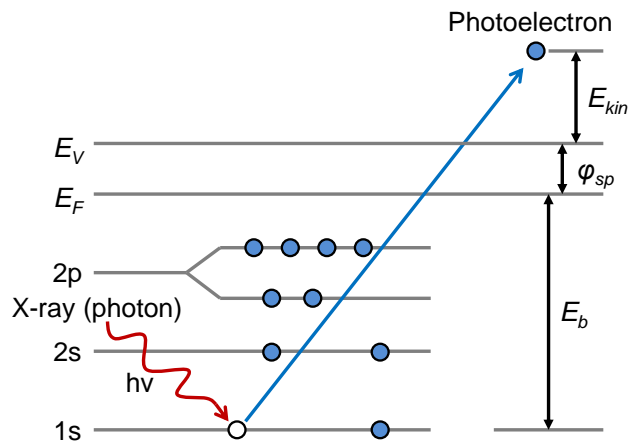


Fig. 2.7 Schematic diagram of XPS.

### 2.2.5 Adhesion strength

Micro-scratch testing was performed to evaluate the adhesion strength of the Ag films to the  $\text{SiO}_2$  substrates using RHESCA CSR-2000 tester at room temperature. Figure 2.8 shows the schematic diagram of the micro-scratch testing. <sup>93)</sup> The cartridge body is forced to swing, instead of the stylus being forced to swing as in the playback system. A diamond stylus on the free end of the cantilever touches the sample surface and slides, following the swing of the cartridge body. The forces working on the stylus are mainly elastic restoration force of the cantilever and the friction from the material surface. The friction hampers the trailing motion of the stylus, and makes a phase delay to the body swing. This difference of the motion between the stylus and the cartridge body

generates a voltage signal in the cartridge. The type of the voltage generation is a moving magnet in a fixed coil unit. As the magnitude of the friction increases with increasing the stylus load, the stylus motion becomes delayed and the signal grows. Finally, the film will be completely peeled by the moving stylus with a specific critical load, and the critical load is used to quantify the adhesion strength of film to substrate. The measurement conditions of this study are listed in Table 2.4.

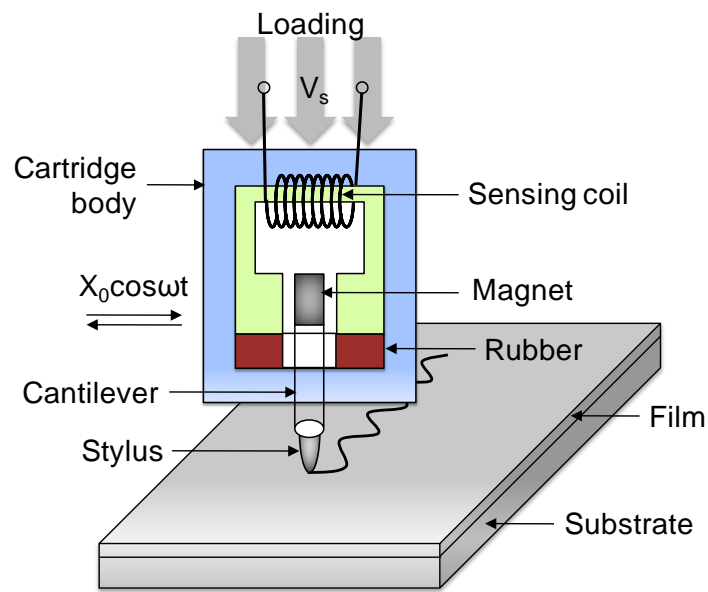


Fig. 2.8 Schematic diagram of micro-scratch testing.

Table 2.4 Measurement conditions for micro-scratch testing.

Radius of the diamond stylus	25 $\mu\text{m}$
Spring constant of the stylus	100 g/mm
Loading speed	2.67 mN/s
Scratch speed	10 $\mu\text{m/s}$
Frequency of the swing	45 Hz
Amplitude of the swing	100 $\mu\text{m}$

## 2.2.6 Crystal structure

The crystal structure of the films before and after annealing was investigated using RIGAKU RINT2000 X-ray diffractometer by the  $\theta$ - $2\theta$  scan method. Figure 2.9 shows the schematic diagram of the  $\theta$ - $2\theta$  scan. The  $\theta$ - $2\theta$  scan maintains the same angle  $\theta_i$  between the sample and detector as the one between the sample and X-ray source during scanning. By comparing the JCPDS (Joint Committee on Powder Diffraction Standards) cards, the crystal structure can be identified.

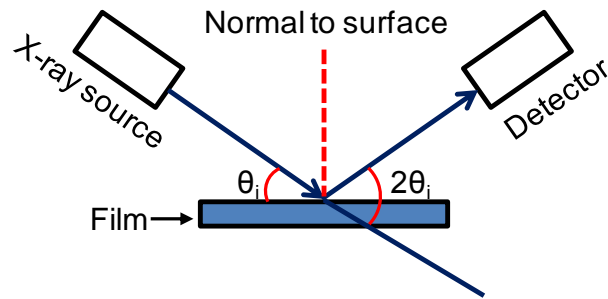


Fig. 2.9 Schematic diagram of  $\theta$ - $2\theta$  scan.

Precision  $\theta$ - $2\theta$  scan was carried out to accurately measure the interplanar spacing and the grain size of Ag(111). From the  $\theta$ - $2\theta$  XRD pattern, the interplanar spacing of the detected lattice plane can be figured out by the Bragg's law,<sup>94)</sup>

$$n\lambda = 2d_{hkl}\sin\theta \quad (2.7)$$

where  $\lambda$  is the wavelength of the X-ray,  $d_{hkl}$  is the interplanar spacing, and  $\theta$  is the incident angle.

It is well known that grain size is usually calculated using Scherrer's formula,<sup>95,96)</sup> as shown in Eq. 2.8,

$$D = \frac{0.9 \lambda}{B \cos\theta} \quad (2.8)$$

where  $D$  is the grain size (nm),  $\lambda$  is the wavelength of the X-ray (nm),  $B$  is the full width at half maximum (FWHM) of the broadened diffraction line on the  $2\theta$  scale (rad), and  $\theta$  is the diffraction angle (deg). Note that  $B$  is an angular width, in terms of  $2\theta$  (not  $\theta$ ), and not a linear width. In addition, the units for  $B$  and  $\theta$  are different.

In order to investigate the crystalline orientation of Ag(111), rocking curve measurement was also employed. By fixing the detector at the center of the expected Bragg reflection, at the angle  $2\theta_{\text{fixed}}$ , and following the diffracted intensity as the sample is independently rotated, as shown in Fig. 2.10, a rocking curve is gained. The sharper the rocking curve, the higher the crystalline perfection.<sup>97)</sup> Thus, FWHM of the rocking curve is used to evaluate the crystalline orientation.<sup>98)</sup>

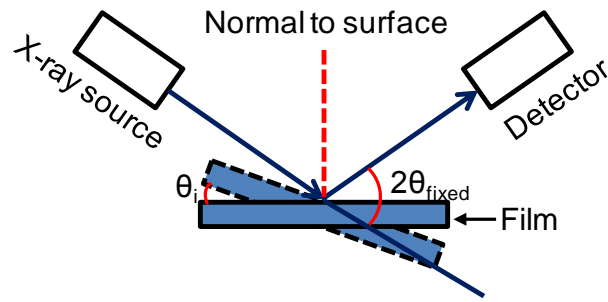


Fig. 2.10 Schematic diagram of rocking curve testing.

The measurement conditions and instrument parameters for the XRD analysis in this study are listed in Table 2.5.

Table 2.5 Measurement conditions and instrument parameters for XRD.

	Standard $\theta$ - $2\theta$ scan	Precision $\theta$ - $2\theta$ scan	Rocking curve
Tube	Cu $K\alpha$	Cu $K\alpha$	Cu $K\alpha$
Tube voltage	40 kV	40 kV	40kV
Tube current	20 mA	30 mA	20 mA
Goniometer	Wide angle	Wide angle	Wide angle
Sampling width	0.020 °	0.002 °	0.020 °
Scan angle	$2\theta_i = 30\sim 75$ °	$2\theta_i = 36\sim 40$ °	$\theta_i = 10\sim 25$ °
Scan speed	4 °/min	0.4 °/min	2 °/min
Divergence slit	1 °	1 °	0.05 mm
Scattering slit	1 °	1 °	1/2 °
Receiving slit	0.3 mm	0.15 mm	0.3 mm

## **Chapter 3 Effects of Ti Surface Layer and Interface Layer on Thermal Stability and Electrical Properties of Ag Thin Film**

### **3.1 Introduction**

As mentioned in Chapter 1, we have reported the improvement of the thermal stability and the maintenance of the low resistivity of Ag thin films by the modification of the film structure, where very thin Al layers are introduced at the top and bottom of the Ag films. Because Al with large free energy for Al-oxide formation is easy to be oxidized, the oxidation of the Al surface layer can provide a passivation layer to suppress the surface diffusion of the Ag film, meanwhile, the oxidation of the Al interface layer can improve the adhesive strength between the Ag film and the SiO<sub>2</sub> substrate, which brings about the agglomeration suppression of the Ag film. Simultaneously, because Al is difficult to dissolve into Ag, the part of the Ag layer keeps pure, in which no impurity scattering occurs. The resistivity of the multilayered film maintains very low before and after annealing. In the present chapter, we attempted the same strategy using Ti instead of Al, owing to their both large free energies for the oxide formation,<sup>99)</sup> at -884.5 kJ/mol (TiO<sub>2</sub>) and -1582.3 kJ/mol (Al<sub>2</sub>O<sub>3</sub>), respectively. It is expected that a similar effect to that of Al on agglomeration suppression may also result using Ti.

### **3.2 Experimental procedure**

In order to investigate the effects of the Ti surface layers and interface layers on the thermal stability and electrical resistivity of the multilayered Ag films, the films of Ag (100 nm), Ti (1~10 nm)/Ag (100 nm), and Ag (100 nm)/Ti (1~10 nm) were deposited using RF magnetron sputtering in an Ar atmosphere and then annealed in the lamp-heating furnace under vacuum. Then, the triple-layer structure, namely Ti/Ag/Ti film, was prepared and annealed to study the combined effects of the Ti surface layers and interface layers on agglomeration suppression. The structure of the multilayered

films is shown in Fig. 3.1. The preparation conditions, heat treatment conditions, and evaluation methods have been described in details in Chapter 2.

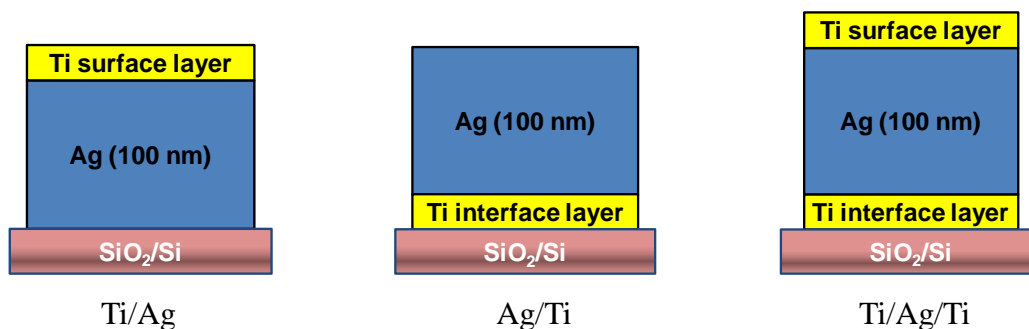


Fig. 3.1 Structure of the multilayered films deposited using RF magnetron sputtering. (a) Ti/Ag film, (b) Ag/Ti film, and (c) Ti/Ag/Ti film.

### 3.3 Ag film with Ti surface layer (Ti/Ag film)

#### 3.3.1 Surface morphology

Generally speaking, the degree of Ag agglomeration can be judged by the amount and size of the voids and hillocks and the roughness of the surface through the observation of SEM and AFM.<sup>29-31, 57, 58)</sup> In this study, the SEM and AFM analyses were used to evaluate the thermal stability of the Ag films with Ti surface layers. Figure 3.2 shows the SEM images of the Ti (1~10 nm)/Ag films before and after annealing. It is difficult to find out the difference in the surface morphology among the as-deposited Ti/Ag films, because they are all very flat. Next, the surface morphology of the films after annealing at 500 °C is compared. Although the size and amount of the voids at the surface of the Ti (1 nm)/Ag film are similar to the Ag single layer film, the hillocks of the Ti (1 nm)/Ag film are fewer than the Ag film, as shown in Fig 1.3. In other word, the parts of this film without voids keep smooth. With increasing the thickness of the Ti surface layers to 3 nm and above, the films show similar surface morphology with less voids and no hillock, which are better than the Ti (1 nm)/Ag film. After annealing at 600 °C, it is observed that Ti (1 nm)/Ag film is agglomerated, though the dewetted area (the exposed part of the substrate) is smaller than the Ag film without Ti surface layer. With increasing the thickness of the Ti surface layer, the severe agglomeration is suppressed,

and only small voids are observed in the Ti (3~10 nm)/Ag films. On the whole, the Ti (3~10 nm)/Ag films show almost the same smooth surface after annealing.

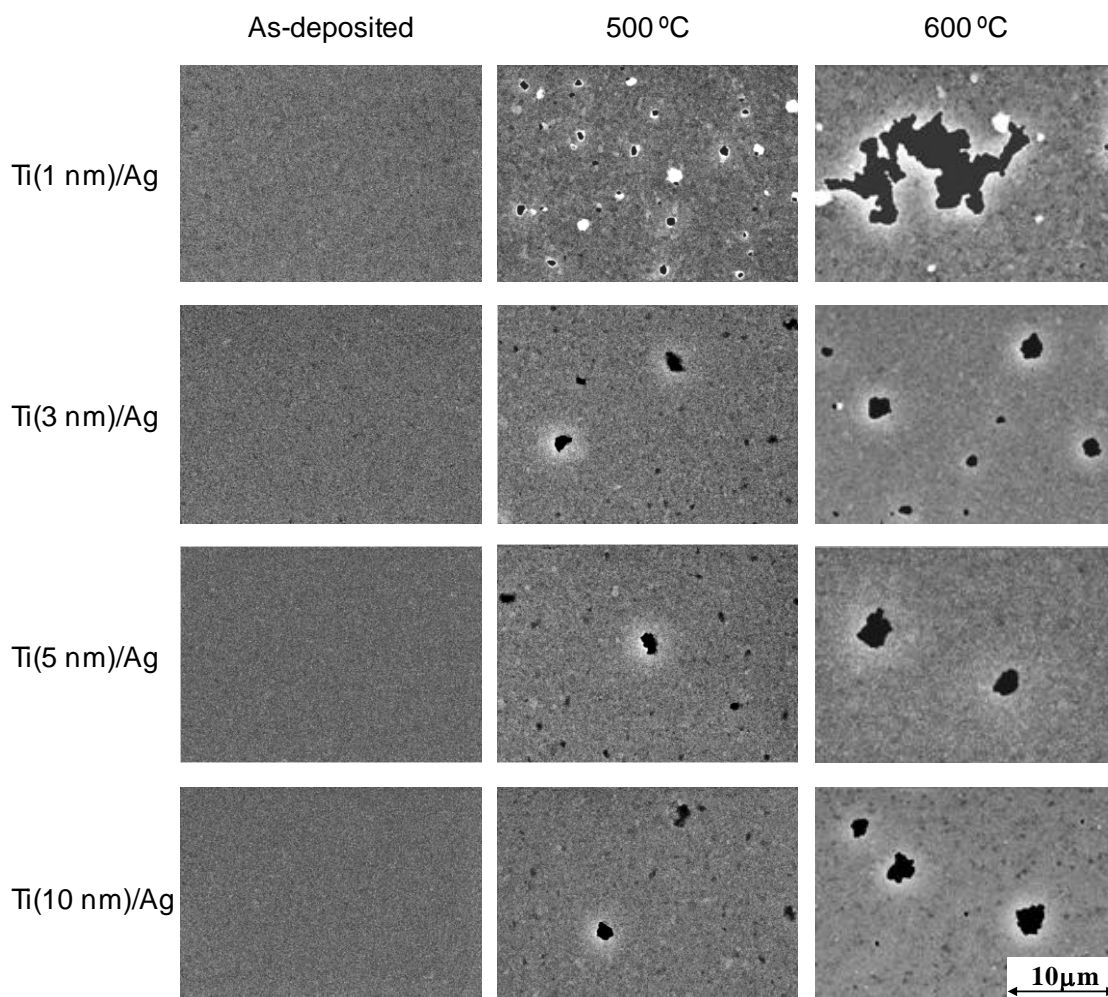


Fig. 3.2 SEM images of the Ti (1~10nm)/Ag films before and after annealing.

Figure 3.3 gives the AFM line profiles of the voids in the Ti (3 nm)/Ag films after annealing at 500 °C and 600 °C. The depth of the voids formed after annealing at 500 °C and 600 °C is approximately 10 and 15 nm, respectively. It is illustrated that the void did not become much deeper with increasing the annealing temperature from 500 °C to 600 °C, which indicates the progress of Ag agglomeration was slow. In addition, because the thickness of Ag films is about 100 nm, the voids in the Ti (3 nm)/Ag films have not reached to the substrate surface. Consequently, it is indicated

that the agglomeration of the Ag films is effectively suppressed by the Ti surface layers with the thickness of 3 nm and above.

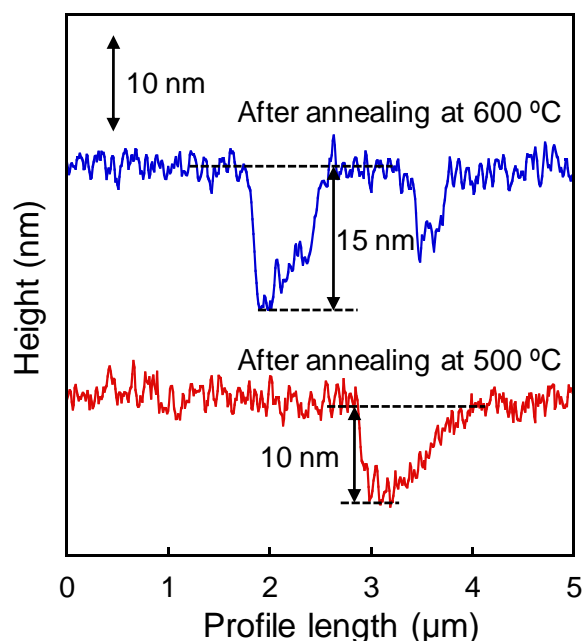


Fig. 3.3 AFM line profiles of the Ti (3 nm)/Ag films after annealing at 500 °C and 600 °C.

Table 3.1 The surface roughness of the Ti (1~10 nm)/Ag films after annealing at 500 °C and 600 °C.

	Rms roughness (nm)	
	500 °C	600 °C
Ti (1 nm)/Ag	1.6	2.8
Ti (3 nm)/Ag	1.5	2.6
Ti (5 nm)/Ag	1.6	2.7
Ti (10 nm)/Ag	1.7	2.9

The rms roughness of the surfaces of Ti (1~10 nm)/Ag films after annealing at 500 °C and 600 °C, except where there are voids, is listed in Table 3.1. The results suggest that the surface of all the Ti/Ag films, except where there are voids, is very flat. Even if the annealing temperature was increased from 500 °C to 600 °C, the rms roughness only

increased to less than 3.0 nm. The improvement in the thermal stability of the Ag films has been proved further.

### 3.3.2 Electrical resistivity

Low resistivity is another important feature that is required for the electrodes and metallization materials. Figure 3.4 shows the change in the resistivity of the Ag (100 nm) and Ti (1~10 nm)/Ag films as a function of annealing temperature. The resistivity of the as-deposited Ti/Ag films slightly increases from 2.9 to 3.5  $\mu\Omega$  cm with increasing the thickness of the Ti surface layer from 1 to 10 nm. The influence of the thickness of the Ti surface layers on the resistivity is caused by the much higher resistivity of bulk Ti ( $\rho = 42.0 \mu\Omega$  cm at 293 K) than that of Ag ( $\rho = 1.59 \mu\Omega$  cm at 293 K).<sup>3)</sup> However, as compared to Fig.1.7, the change in the resistivity of Ti/Ag films with increasing the thickness of the Ti surface layer is much smaller than that of the Ag-Ti alloy films with increasing Ti content. This is because the Ti surface layers are very thin and the main parts of the films for electronic conduction should be pure Ag. Unlike the alloy films, the main part of the pure Ag in the multilayered films has not suffered from the impurity scattering effect.<sup>69)</sup> Thus, It is indicated that the character of low resistivity is not lost by coating a thin Ti surface layer.

After annealing at 500 °C, the resistivity of all the films decreases. This phenomenon is considered to be due to no occurrence of serious agglomeration and the improvement in the crystallinity of the Ag films, which will be explained in detail in the later section of this chapter. In addition, the effect of the thickness of the Ti surface layers on the resistivity does not disappear, and is almost the same to that of the as-deposited ones. By the way, it has been reported that the surface roughness of the films could influence the resistivity.<sup>100)</sup> By comparing with the surface roughness (as shown in Table 1.2 and Table 3.1) and the resistivity (as shown in Fig. 3.4), the influence of surface roughness on the resistivity is scarcely observed in this study. After annealing at 600 °C, the resistivity of the Ag (100 nm) single layer film increases remarkably caused by partial film dewetting, which reduces the conduction area for electrons. The degree of the agglomeration happened in the Ti (1 nm)/Ag film is smaller than that of the Ag single layer film, therefore, the increase of the resistivity of the Ti (1 nm)/Ag film is not very

abrupt. In contrast, the resistivity of the Ti (3~10 nm)/Ag films remains at a very low level after annealing, because void formation was negligible.

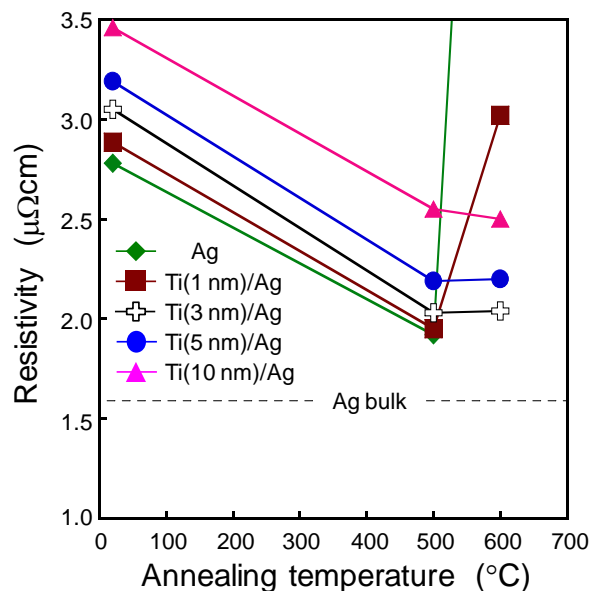


Fig. 3.4 Resistivity of the Ag (100 nm) and Ti (1~10 nm)/Ag films as a function of annealing temperature.

In summary, it is indicated that the thickness of 1 nm for the Ti surface layer is not enough to suppress the agglomeration of the Ag films satisfactorily, but 3 nm is quite sufficient because of no obvious difference occurring with further increasing the thickness of the Ti surface layers. However, the resistivity of the Ti (3~10 nm)/Ag films becomes a little higher with increasing the thickness of the Ti surface layers. Therefore, from the viewpoints of the surface morphology and the resistivity, it is clearly demonstrated that the use of Ti surface layer is helpful to the inhibition of Ag agglomeration and the maintenance of low resistivity, and 3 nm is the optimum thickness.

### 3.3.3 Chemical bonding state of the surface

In order to explore the mechanism of agglomeration suppression brought by the Ti surface layers, the chemical bonding state of the surface was analyzed firstly. Figure 3.5

shows the XPS spectra of the surface of the Ti (3 nm)/Ag film before and after annealing at 500 °C. The binding energy for the main peaks of Ti 2p<sub>3/2</sub> in both as-deposited and annealed samples is 458.7 eV, which is the same as the reference of TiO<sub>2</sub> (458.8eV).<sup>101)</sup> The dissimilarity is that there is a weak peak of 454.0 eV only in the as-deposited film, and the peak belongs to the Ti metal according to the reference value of 454.1 eV.<sup>101)</sup> It is considered that, because the free energy of TiO<sub>2</sub> formation is very large, the Ti surface layer is easy to be oxidized even at room temperature. It is indicated that TiO<sub>2</sub> was formed partly by the natural oxidation before annealing, and the residual Ti was oxidized completely after annealing at 500 °C.

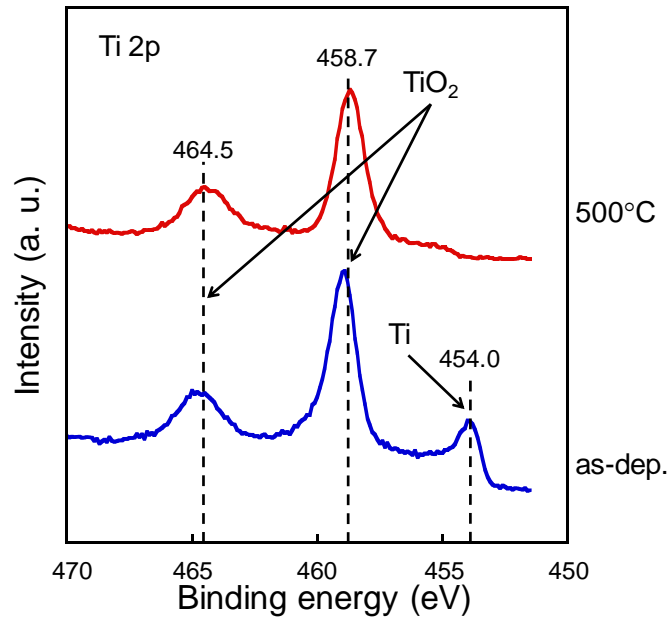


Fig. 3.5 Ti 2p XPS spectra for the surfaces of the Ti (3 nm)/Ag films before and after annealing at 500 °C.

In addition, it is difficult for Ti to dissolve in Ag at high temperature judging from the phase diagram,<sup>102)</sup> as shown in Fig. 3.6, so the residual Ti metal at the surface would not diffuse to the inside of the film but react with the residual O<sub>2</sub> in the furnace during annealing. The mechanism of Ag agglomeration has been discussed in Chapter 1. It has been confirmed that the agglomeration of the Ag thin films is mainly dominated by surface diffusion mass transport.<sup>60, 61)</sup> As is well-known, TiO<sub>2</sub> has got high thermal stability.<sup>103)</sup> Just like the role of the Al oxide surface layers in Ag-Al alloy films and

Al/Ag multilayered films,<sup>29, 66, 69, 104)</sup> the Ti oxide surface layer is considered to play an important role as a passivation layer in suppressing the surface diffusion of Ag atoms, which leads to the suppression of Ag agglomeration.

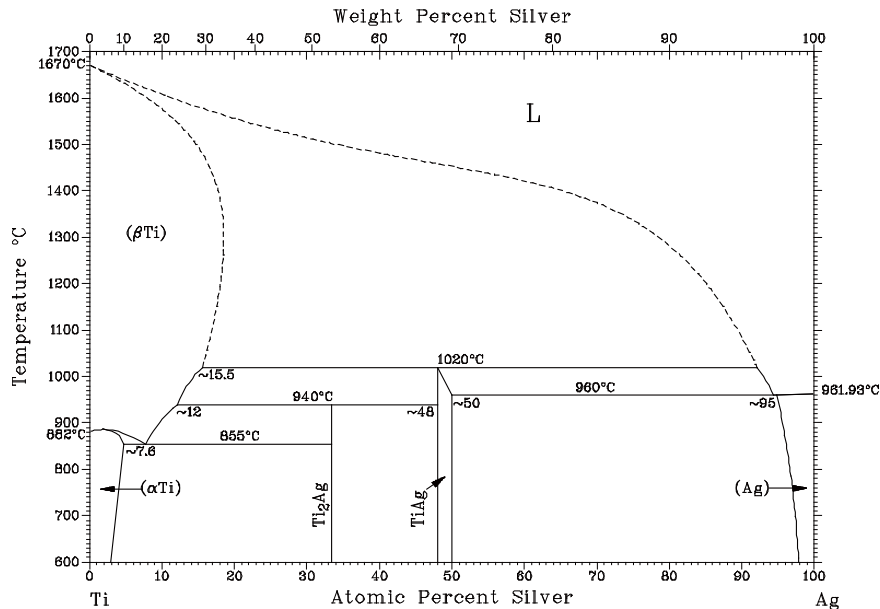


Fig. 3.6 Ag-Ti binary phase diagram.<sup>102)</sup>

### 3.3.4 Crystal structure

Figure 3.7 shows XRD patterns of the as-deposited Ag (100 nm) and Ti (1~10 nm)/Ag films. The Ti surface layer is too thin to be detected by the XRD apparatus. All the patterns consist of the Ag(111) and Ag(200) peaks, and the peaks of the Ag(111) which is the closest-packed plane of fcc crystal structure are extremely strong. Because it is difficult to clearly distinguish the differences among these as-deposited films after inspecting the intensity (approximately 2000 cps), full width at half maximum (FWHM) (approximately 0.22~0.25 °), and position (approximately 38.06 °) of every Ag(111) peak, it is considered that the Ti surface layers have little influence on the structure of the underlying Ag films during the process of sputtering.

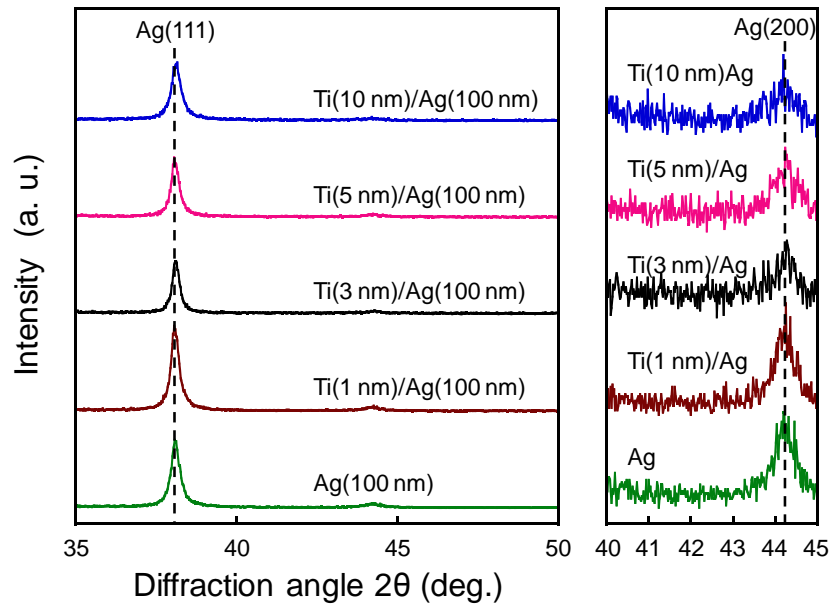


Fig. 3.7 XRD patterns of the as-deposited Ag (100 nm) and Ti (1~10 nm)/Ag films.

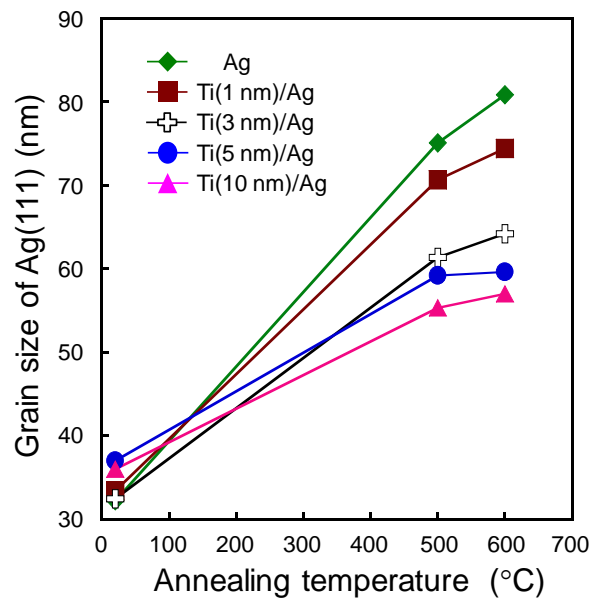


Fig. 3.8 Grain size of Ag(111) for the Ag (100 nm) and Ti (1~10 nm)/Ag films as a function of annealing temperature.

Figure 3.8 shows the grain size of Ag(111) in the Ag (100 nm) film and Ti (1~10 nm)/Ag films as a function of annealing temperature. By annealing at 500 °C, the

Ag(111) grains in all the films rapidly grow up, which results in the reduction of grain boundaries and defect concentration. This could be used to explain the sharp decline in resistivity. After annealing at 600 °C, the Ag(111) grains in the Ag and Ti (1 nm)/Ag films continue to grow greatly. On the contrast, the overgrowth of the Ag(111) grains in Ti (3~10 nm)/Ag films is restrained, which adequately reflects the effective suppression of Ag agglomeration owing to the Ti surface layers with the thickness of 3 nm and above.

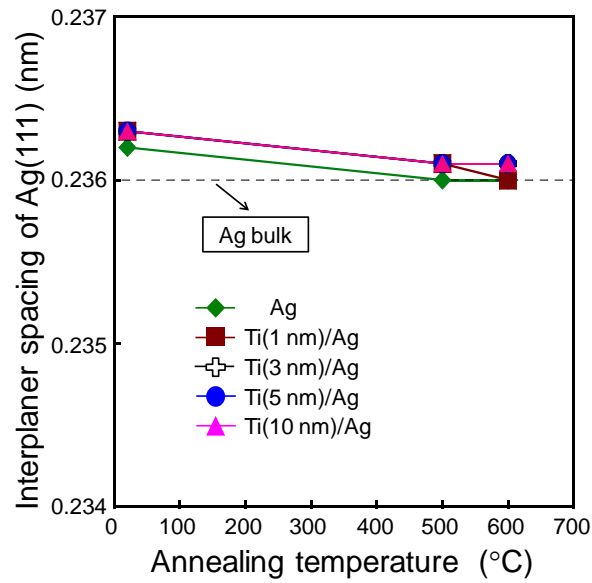


Fig. 3.9 Interplanar spacing of Ag(111) for the pure Ag (100 nm) and Ti (1~10 nm)/Ag films as a function of annealing temperature.

Interplanar spacing of Ag(111) for the pure Ag (100 nm) and Ti (1~10 nm)/Ag films as a function of annealing temperature is shown in Fig. 3.9. Before annealing, the interplanar spacing of Ag(111) for the Ag single layer film is a little larger than that of the bulk Ag. Then, it is closed to that of the bulk Ag owing to the improvement of the crystallinity with increasing the annealing temperature. Because some interplanar spacing values for different films are identical, some marks are overlapped and can not be seen clearly. By introducing the Ti surface layers, no difference in the change of the interplanar spacing is recognized. It is indicated that Ti at the surfaces did not dissolve into the Ag parts during annealing, as predicted from the phase diagram (Fig. 3.6). It is

also accordant with the resistivity of the Ti/Ag films, which did not suffer from the impurity scattering effect, as shown in Fig. 3.4.

### **3.4 Ag film with Ti interface layer (Ag/Ti film)**

#### **3.4.1 Surface morphology**

Figure 3.10 shows the SEM images of the Ag/Ti (1~10 nm) films before and after annealing, and the rms roughness of the parts without voids in the Ag/Ti (1~10 nm) films after annealing is shown in Table 3.2. The SEM images of all the as-deposited films show their smooth surface. After annealing at 500 °C, the Ag/Ti films except the Ag/Ti (1 nm) film still show flat surface. The Ag/Ti (1 nm) film seems slightly rough, which is confirmed from the larger roughness value in Table 3.2.

The annealing temperature of 600 °C promoted the agglomeration of Ag. However, the Ag/Ti films have not exhibited very severe agglomeration, as shown Fig. 3.10. Although the Ag/Ti (1 nm) film shows some voids at the surface, the voids are not big enough to connect with each other and to make the film discontinuous. It is thought that 1-nm-thick Ti interface layer deposited on the substrate is too thin to become continuous so that its influence is not enough. Then, with increasing the thickness of the Ti interface layers to 3 nm and above, the amount of voids greatly reduces, and the Ag/Ti (3~10 nm) films show the similar surface morphology. From the Table 3.2, it is known that, after annealing, the surface roughness decreases with increasing the thickness of the Ti interface layers, and that of the Ag/Ti (3~10 nm) films seems the same, which is in agreement with the results of the SEM analysis. From the analysis of surface morphology, the agglomeration suppression is benefited from the Ti interface layers, and 3-nm-thick Ti interface layer is considered to be sufficient.

On the other hand, it is found that the effect of the Ti interface layer on the thermal stability of the Ag film is inferior to that of the Ti surface layer by comparing with the results of the previous section. It is suggested that the surface diffusion should be the major cause of Ag agglomeration, and the effect of the Ti surface layer is more outstanding. Even so, the good effect of the Ti interface layer should not be ignored.

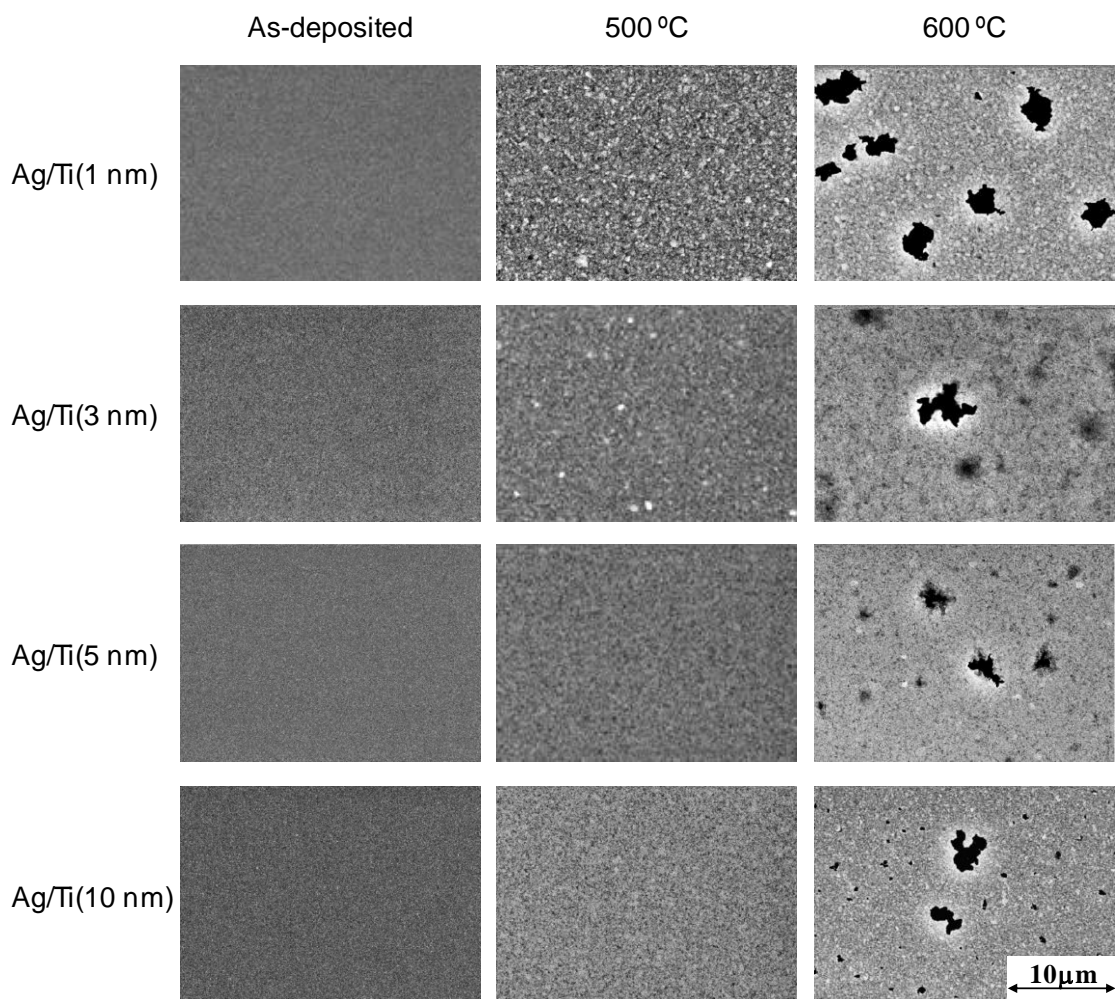


Fig. 3.10 SEM images of the Ag/Ti (1~10nm) films before and after annealing.

Table 3.2 The surface roughness of the Ag/Ti (1~10 nm) films after annealing at 500 °C and 600 °C.

Rms roughness (nm)		
	500 °C	600 °C
Ag/Ti (1 nm)	8.4	8.2
Ag/Ti (3 nm)	3.3	3.6
Ag/Ti (5 nm)	3.4	3.4
Ag/Ti (10 nm)	3.6	3.8

### 3.4.2 Electrical resistivity

Figure 3.11 shows the electrical resistivity of the Ag (100 nm) and Ag/Ti (1~10 nm) films as a function of annealing temperature. The resistivity of all the Ag/Ti (1~10 nm) films certainly comes down after annealing at 500 °C, but slightly increases with increasing the annealing temperature to 600 °C caused by agglomeration occurring to some extent. At the same time, an interesting phenomenon is noticed that the resistivity of the as-deposited Ag/Ti (3~10 nm) films is similar and approximately 0.2  $\mu\Omega$  cm lower than that of the Ag film. The possible reason will be explained in the following. From the results of the resistivity, the good effects of the Ti interface layers on the suppression of Ag agglomeration and the maintenance of low resistivity at high temperature are appreciated.

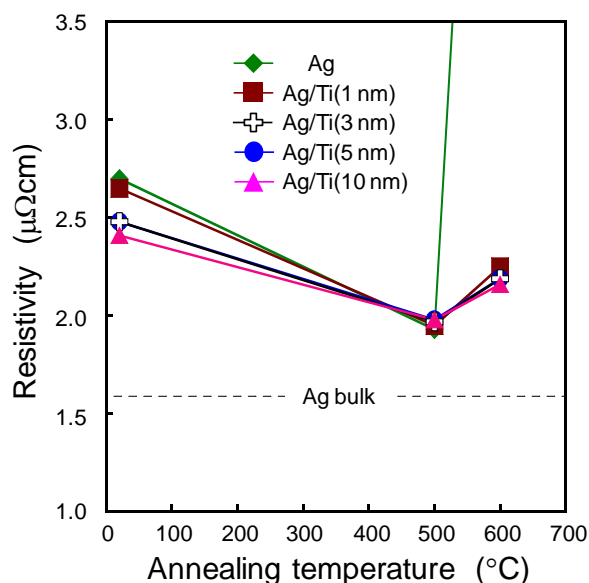


Fig. 3.11 Resistivity of the Ag (100 nm) and Ag/Ti (1~10 nm) films as a function of annealing temperature.

### 3.4.3 Adhesion Strength of Ag/Ti Film to $\text{SiO}_2$ Substrate

The roles of the Ti interface layer are discussed in the following two sections. Ti has been often used as an underlying material to enhance the adhesion of other films to the  $\text{SiO}_2$  substrates,<sup>105-107)</sup> resulting from a large affinity for Ti and oxygen, which is

expected to give a good influence on agglomeration suppression of Ag films. In this study, the adhesive strength of Ag and Ag/Ti films on the SiO<sub>2</sub> substrates was evaluated by means of the critical delamination load measurement using the micro-scratch test, and the results are shown in Fig. 3.12. By inserting the Ti interface layers with 1 nm and above, the adhesion strength increases to about four times stronger than that of the pure Ag film on the SiO<sub>2</sub> substrate. It is considered that, instead of the weak bonding interface of Ag to the SiO<sub>2</sub> substrate, the Ti interface layer forms both strong metallic bonds to the Ag film and strong covalent bonds with the SiO<sub>2</sub> substrate. As discussed in Chapter 1, one possible cause for the agglomeration of the Ag films is considered to be that the Ag films are less adhesive on the SiO<sub>2</sub> or glass substrates, so the improvement of the adhesion between the Ag film and the SiO<sub>2</sub> substrate should be an important reason for the suppression of Ag agglomeration.

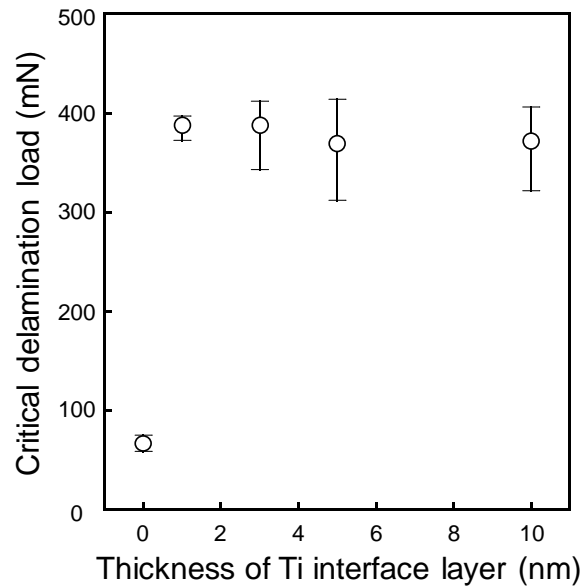


Fig. 3.12 Critical delamination load of the as-deposited Ag (100 nm) and Ag/Ti (1~10 nm) films.

### 3.4.4 Crystal structure

Figure 3.13 shows XRD patterns of the as-deposited Ti (60 nm), Ag (100 nm) and Ag/Ti (1~10 nm) films. It is interesting that the intensity of Ag(111) peak increases

abruptly with increasing the thickness of the Ti interface layers to 3 nm and above. However, the FWHM of these peaks does not distinctly change, which suggests that the grain size does not change with changing the thickness of the Ti interface layers. Then, it is also found that the Ag(200) peaks disappear with increasing the thickness of the Ti interface layers to 3 nm and above. It is indicated that the Ag/Ti (3~10 nm) films display preferential orientation of Ag(111).

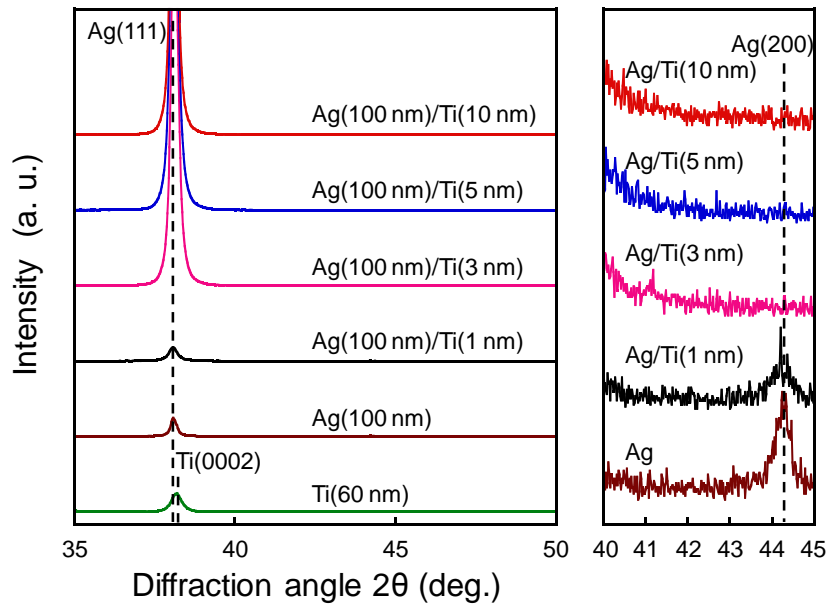


Fig. 3.13 XRD patterns of the as-deposited Ag (100 nm) and Ag/Ti (1~10 nm) films.

Then, the FWHM of XRD rocking curve was further investigated to evaluate the crystalline orientation of Ag(111) in the as-deposited Ag and Ag/Ti films, as shown in Fig. 3.14. Because the Ag and Ag/Ti (1 nm) films are not oriented single-crystal, the Ag(111) peak could not be clearly pointed out in Fig. 3.14. The Ag/Ti (3~10 nm) films show equally higher crystalline orientation of Ag(111) judging from the much smaller FWHM of the peaks in the rocking curves, which leads to the enhancement of the peak intensity for Ag(111) in the XRD patterns of  $\theta$ -2 $\theta$  scan and the disappearance of Ag(200) peaks.

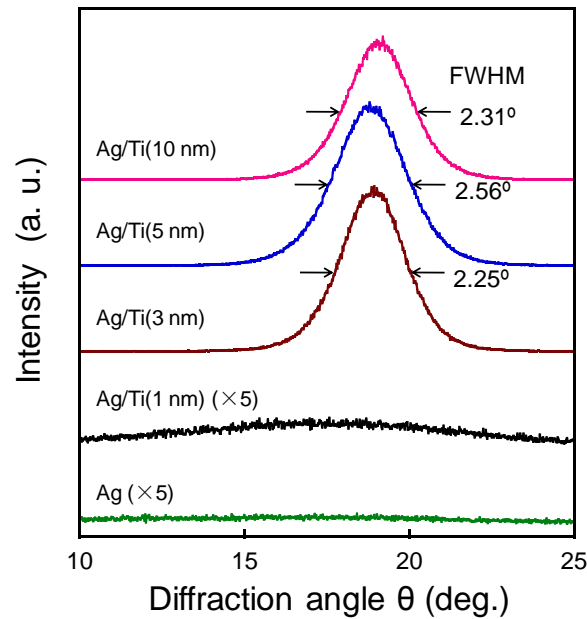


Fig. 3.14 XRD rocking curves of the as-deposited Ag (100 nm) and Ag/Ti (1~10 nm) films.

The above phenomenon could be explained by the local epitaxial growth of Ag(111) on the Ti interface layers. XRD pattern of the pure Ti film deposited on SiO<sub>2</sub> substrate shows that hexagonal close packed Ti film mainly grew towards <0002> preferentially, as shown in Fig. 3.13. It is well known that any three neighboring atoms closely link and form an equilateral triangle at the closest-packed plane of hexagonal (hcp) and face-centered cubic (fcc) structures. The distances between two neighboring atoms at closest-packed Ti(0001) and Ag(111) planes are 0.2944<sup>108)</sup> and 0.2888 nm<sup>2)</sup>, respectively, and the mismatch of axial length for Ag(111)/Ti(0001) is only 1.9%. Therefore, it might be easy for Ag(111) plane to arrange on the Ti(0001) plane. The lattice diagrams of Ti(0001) and Ag(111) are shown in Fig 3.15. The peaks of the Ag and Ag/Ti (1 nm) films in the rocking curves are hardly observed, which means the poorer preferred orientation of Ag(111). It is considered that 1-nm-thick Ti layer is not continuous on the flat SiO<sub>2</sub> substrate to affect the growth of the overcoating Ag film. Therefore, Ag/Ti (1 nm) exhibits no remarkable improvement of crystalline orientation of Ag(111). In contrast, the substrate could be completely covered by the Ti layer with the thickness of 3 nm or above judging from the shallower profile depth than the thickness of Ti layer, as shown in Fig. 3.16, which contributed to the improvement of

crystalline orientation of Ag(111).

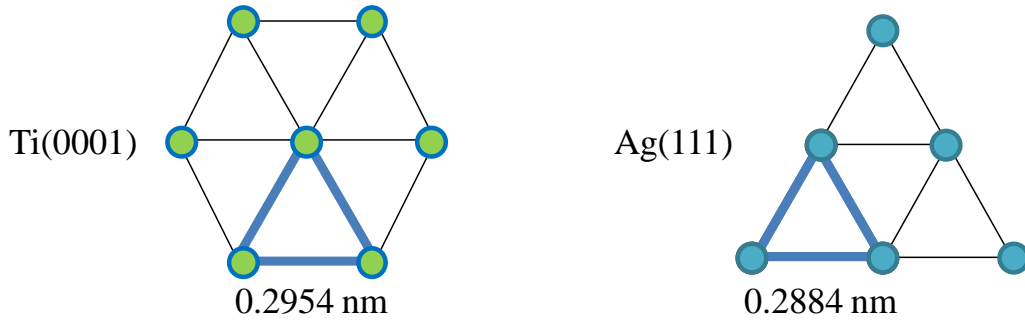


Fig. 3.15 Lattice diagrams of Ti(0001) and Ag(111).

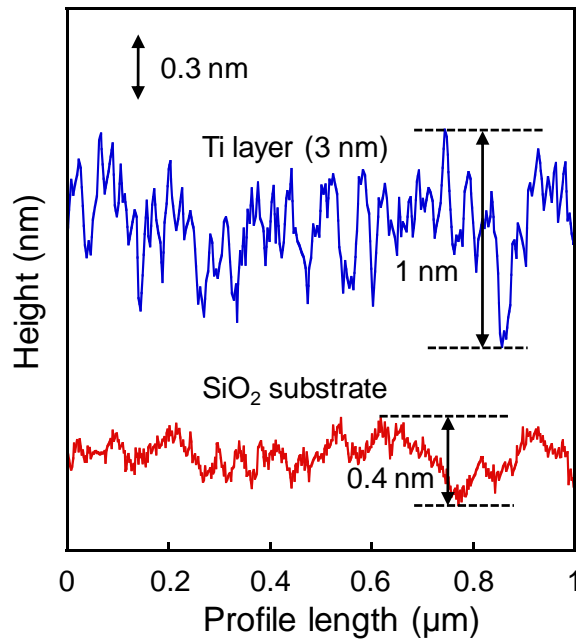


Fig. 3.16 AFM line profiles of the SiO<sub>2</sub> substrate and Ti (3 nm) single layer.

Table 3.3 shows the surface energies of various crystal planes of Ag.<sup>109)</sup> Because Ag(111) is the closest-packed plane with minimum surface energy, the structure of the Ag film with high orientation of Ag(111) is stable. And the enhancement of Ag(111) orientation has been found to be an important factor for the improvement in the thermal stability of Ag films, as mentioned in Chapter 1. Therefore, the other role of the Ti interface layer is to enhance the orientation of Ag(111). On the other hand, because

there is no significant change in the surface roughness and the grain size of Ag(111), and no impurities inside the pure Ag and Ag/Ti films, a remarkable coincidence is found that the resistivity of the as-deposited Ag/Ti films decreases with increasing the orientation of the close-packed plane of Ag(111). The same phenomenon has been observed by other groups, too.<sup>50, 110-112)</sup> Arbab<sup>110)</sup> argued that this reduction of resistivity resulted from less grain boundary scattering effect. Tsuda et al.<sup>111)</sup> thought that it was attributed to the less crystallographic defect in the highly oriented Ag films. We suppose that the electrical conductivity of different crystal planes parallel to the substrate is different, and the sheet resistance of the closest-packed plane Ag(111) should be the lowest in the crystal Ag film. In conclusion, the improvement of the orientation of Ag(111) contributes to the improvement of the thermal stability and the reduction of the resistivity, and 3-nm-thick Ti interface layer is competent enough for the original aim.

Table 3.3 surface energies of various crystal planes of Ag.

Face (hkl)	Surface energies (J/m <sup>2</sup> )
110	1.238
100	1.200
111	1.172

Figure 3.17 shows the grain size of Ag(111) in the Ag (100 nm) film and Ag/Ti (1~10 nm) films as a function of annealing temperature. With inserting the Ti interface layers, the growth of the grain size of Ag(111) noticeably slows down after annealing. Especially, the effect of the Ti interface layers with 3 nm and above is more remarkable. The grain size of the Ag/Ti (3~10 nm) films does almost not change with increasing the annealing temperature from 500 °C to 600 °C. It is indicated that the Ti interface layer is beneficial to the reduction of the growth rate of the Ag(111) grain, which contributes to the agglomeration suppression.

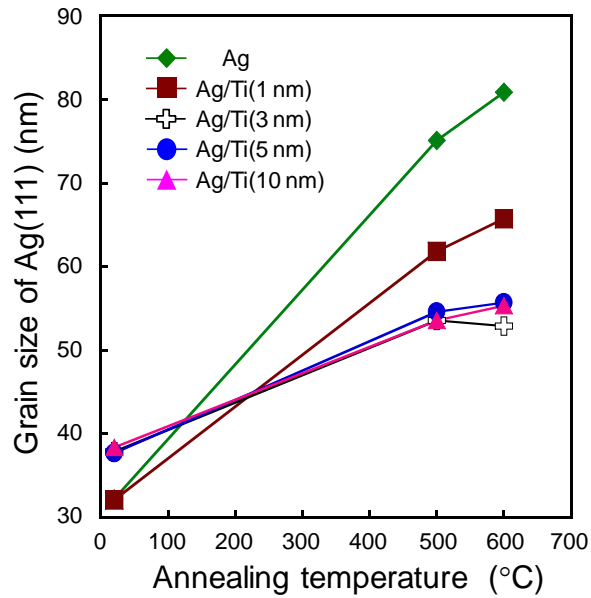


Fig. 3.17 Grain size of Ag(111) for the pure Ag (100 nm) and Ag/Ti (1~10 nm) films as a function of annealing temperature.

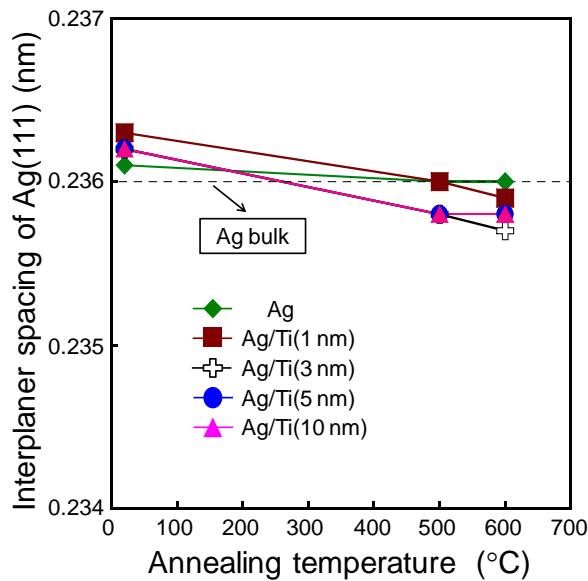


Fig. 3.18 Interplanar spacing of Ag(111) for the pure Ag (100 nm) and Ag/Ti (1~10 nm) films as a function of annealing temperature.

Figure 3.18 shows the interplanar spacing of Ag(111) for the Ag (100 nm) and Ag/Ti (1~10 nm) films as a function of annealing temperature. As expected, the existence of

the Ti interfaces does not influence the interplanar spacing of Ag(111) after annealing. It is suggested that there is no Ti diffusion from the interface layer into the upper Ag body even after annealing at 600 °C. Therefore, after annealing at a certain temperature, the resistivity of the Ag/Ti (3~10 nm) films did not change with increasing the thickness of the Ti interface layer, as shown in Fig. 3.11.

### 3.5 Ti/Ag/Ti triple-layer film

As discussed above, the thickness of 3 nm has been confirmed to be sufficient for both Ti surface layer and Ti interface layer to adequately complete their tasks. Then, the contribution of the combination of Ti surface layer and Ti interface layer to the improvement of thermal stability and the maintenance of low resistivity is expected.

#### 3.5.1 Surface morphology

Figure 3.19 shows the SEM images of the Ti (3 nm)/Ag/Ti (3 nm) film after annealing at 500 °C and 600 °C. Only a very few voids forms after annealing at 500 °C, and thus the surface appears very smooth. After annealing at 600 °C, the amount of voids does not increase, but only the size of some voids become a little bigger. The rms roughness of the surface, except where there were voids, does not change after annealing at 500 °C and 600 °C, as shown in Table 3.4. They appear very flat. In addition, by comparing with the surface morphology of this triple-layer film and the double-layer films, it is found that the thermal stability of the Ag films is further improved owing to the combined effects of the Ti surface layer and interface layer.

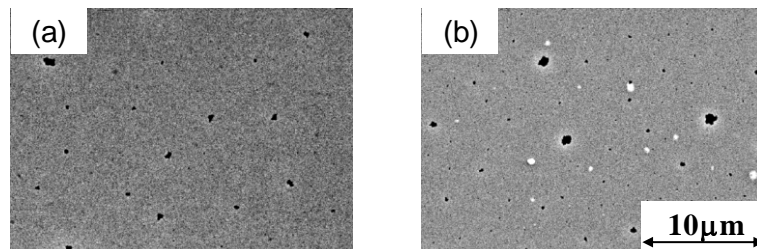


Fig. 3.19 SEM images of the Ti (3 nm)/Ag/Ti (3 nm) films after annealing at 500 °C (a) and 600 °C (b).

Table 3.4 Rms roughness (nm) of the surfaces of the Ti (3 nm)/Ag/Ti (3 nm) films after annealing at 500 °C and 600 °C.

Rms roughness (nm)		
	500 °C	600 °C
Ti (3 nm)/Ag/ Ti (3 nm)	1.1	1.1

### 3.5.2 Electrical resistivity

The change in the resistivity of the Ti (3 nm)/Ag, Ag/Ti (3 nm), and Ti (3 nm)/Ag/Ti (3 nm) films as a function of annealing temperature is shown in Fig. 3.20. The as-deposited Ti (3 nm)/Ag/Ti (3 nm) film does not show the same high resistivity as the Ti (3 nm)/Ag film although they have the same thick surface layer. This is because the Ti interface layer has lowered the resistivity of the triple-layer Ti (3 nm)/Ag/Ti (3 nm) film. The resistivity decreases after annealing at 500 °C, and kept the low value after annealing at 600 °C, owing to the improvement of the crystallinity and the suppression of Ag agglomeration. The resistivity of the Ti (3 nm)/Ag/Ti (3 nm) film after annealing at 600 °C shows the lowest value among all the annealed films, which is 2.0  $\mu\Omega$  cm and close to the resistivity of the Ag bulk.

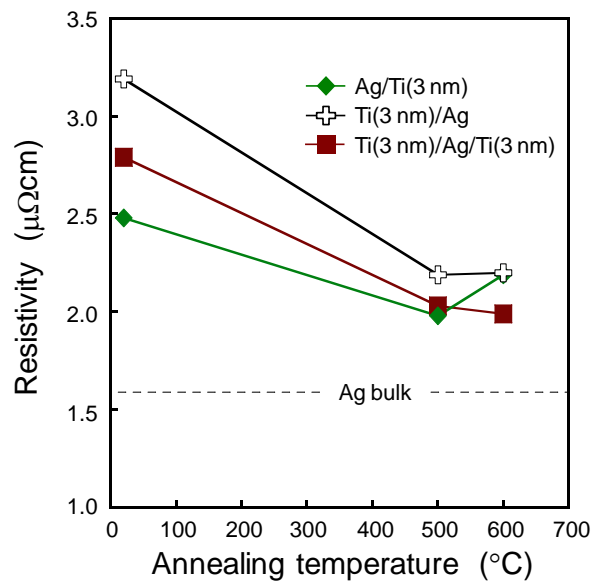


Fig. 3.20 Resistivity of the films as a function of annealing temperature.

### 3.6 Summary

The Ti nano-surface layers with high free energy of oxide formation are easy to be oxidized to form passivation layers, which contribute to the agglomeration suppression of the Ag films. 1-nm-thick Ti surface layer is discontinuous, but 3 nm and above are confirmed to be sufficient for Ti surface layer to effectively suppress the agglomeration of the Ag films. The resistivity of the as-deposited Ti/Ag films slightly increases with increasing the thickness of the Ti surface layers owing to the higher bulk resistivity of Ti. The resistivity of Ti (3~10 nm)/Ag films decreases after annealing at 500 °C, and maintains low after annealing at 600 °C. From the viewpoint of thermal stability and electrical resistivity, a 3-nm-thick Ti layer is an appropriate surface layer.

The Ti interface layers not only improve the adhesion between Ag films and SiO<sub>2</sub> substrates but also induce the growth of (111) single oriented Ag film. Therefore, Ag/Ti (3~10 nm) films exhibit low resistivity and relatively good thermal stability.

Finally, by combining the roles of both the Ti surface layer and interface layer, the triple-layer film of Ti (3 nm)/Ag/Ti (3 nm) is superior to the double-layer films in achieving both good thermal stability and low electrical resistivity simultaneously.

# **Chapter 4 Effects of Nb Surface Layer and Interface Layer on Thermal Stability and Electrical Properties of Ag Thin Film and Optimization for Multilayered Structure of Ag Thin Film**

## **4.1 Introduction**

In the present chapter, Nb nano-layer is selected as the object of study because of its similar characteristics to Ti. For example, the Gibbs free energy of formation of NbO<sub>2.5</sub> ( $\Delta_f G^\circ = -883.1$  kJ/mol) is almost the same to that of TiO<sub>2</sub> ( $\Delta_f G^\circ = -884.5$  kJ/mol);<sup>68)</sup> Nb is very difficult to dissolve in Ag or react with Ag, so that there is no available phase diagram for the Ag-Nb system.<sup>113)</sup> These properties are beneficial for the surface layer and interface layer to suppress the agglomeration of the Ag film. In addition, the lower bulk resistivity of Nb ( $\rho = 12.5$   $\mu\Omega$  cm at 293 K) than that of Ti ( $\rho = 42.0$   $\mu\Omega$  cm at 293 K)<sup>3)</sup> would reduce the influence of the thickness of the surface layers on the sheet resistance of multilayered films, so Nb surface layer is considered to be superior to the Ti surface layer. Thus, the Nb nano-layers are expected to exhibit good effects as surface layers and interface layers of the Ag films. Then, by comparing with the effects of the Nb nano-layers and the Ti nano-layers on the thermal stability and the electrical properties of the Ag films, optimization for the triple-layer structure with the superior surface layer and interface layer is discussed.

## **4.2 Experimental procedure**

Firstly, the Nb (1~10 nm)/Ag (100 nm), Ag (100 nm)/Nb (1~10 nm), and pure Nb (60 nm) films were deposited using RF magnetron sputtering and annealed in a lamp-heating furnace to study the usefulness of the Nb surface layers and interface layers. Next, the triple-layer structure of Nb (5 nm)/Ag (100 nm)/Nb (3, 5 nm) was prepared to investigate the combined effects of both the Nb surface layer and interface layer. Finally, by the comparison between the effects of the Nb nano-layers and the Ti nano-layers, the Nb (3 nm)/Ag (100 nm)/Ti (3 nm) film was fabricated for the

optimization of the triple-layer structure. The structure of all the multilayered films deposited in this study is shown in Fig. 4.1. The details of the preparation conditions, heat treatment conditions, and evaluation methods have been described in Chapter 2.

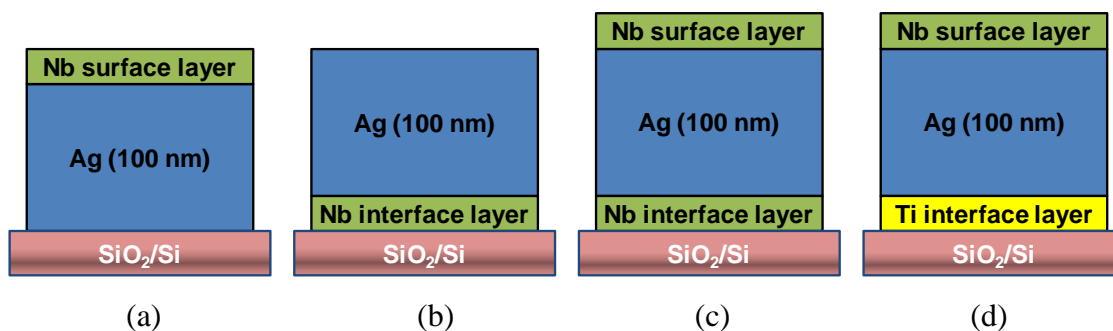


Fig. 4.1 Structure of the multilayered films deposited using RF magnetron sputtering. (a) Nb/Ag film, (b) Ag/Nb film, (c) Nb/Ag/Nb film, and (d) Nb/Ag/Ti film.

### 4.3 Ag film with Nb surface layer (Nb/Ag film)

#### 4.3.1 Surface morphology

The SEM micrographs of Nb (1~10 nm)/Ag films before and after annealing are shown in the Fig. 4.2. All of the as-deposited Nb (1~10 nm)/Ag films show very smooth surfaces. After annealing at 500 °C, they still show smooth surface morphology, except where there are a few small voids and hillocks. After annealing at 600 °C, although the Nb (1 nm)/Ag film is agglomerated as severely as the Ti (1 nm)/Ag film, its dewetted area is smaller than that of the pure Ag film. It is found that a 1-nm-thick Nb layer is not enough to suppress the agglomeration of the Ag film. The morphological stability is significantly improved by increasing the thickness of the Nb surface layer to 3 nm or above, and the Nb surface layers with the thicknesses of 5 nm and above appears to be more effective for agglomeration suppression judging from the number and area of voids formed after annealing at 600 °C.

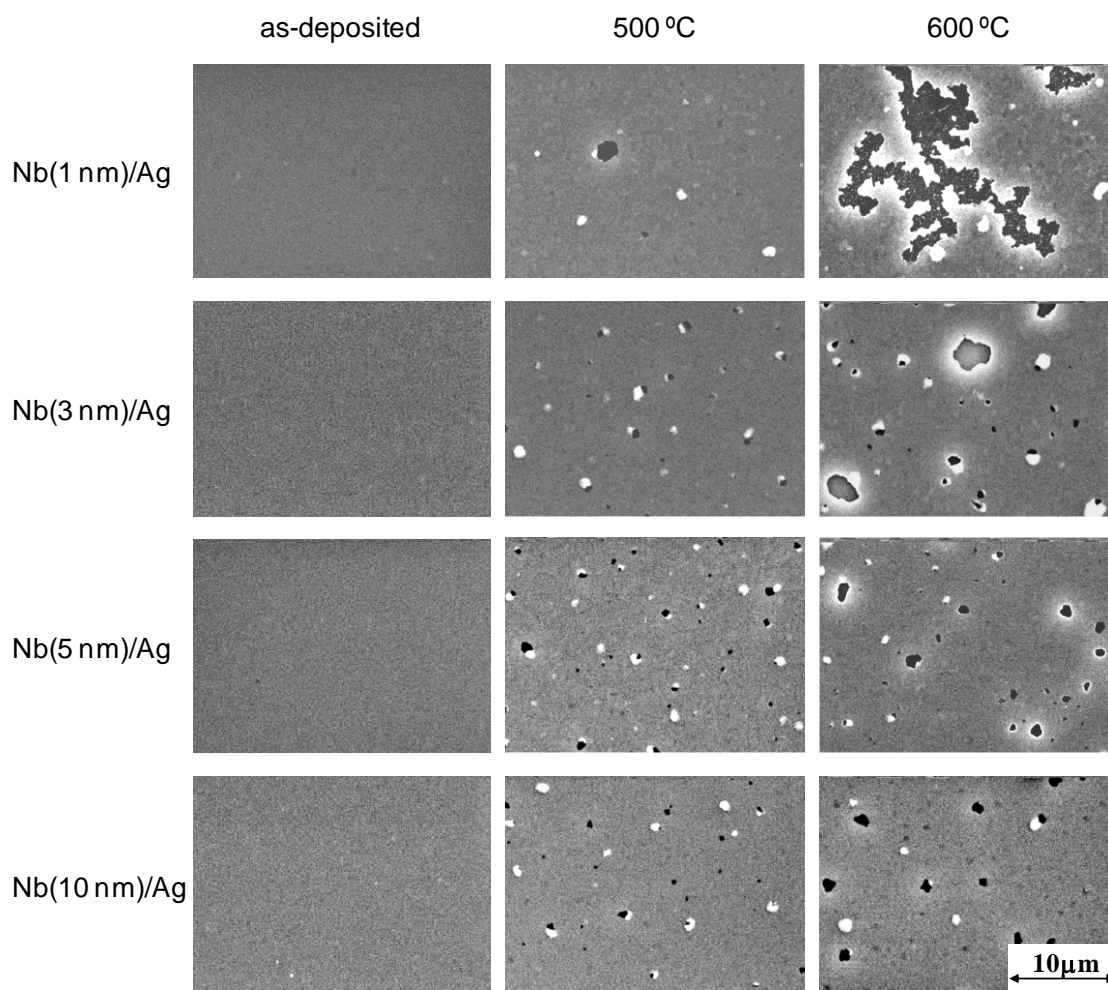


Fig. 4.2 SEM images of the Nb (1~10nm)/Ag films before and after annealing.

Table 4.1 The surface roughness of the Nb (1~10 nm)/Ag films after annealing at 500 °C and 600 °C.

Rms roughness (nm)		
	500 °C	600 °C
Nb (1 nm)/Ag	1.9	5.9
Nb (3 nm)/Ag	1.7	2.3
Nb (5 nm)/Ag	1.9	2.3
Nb (10 nm)/Ag	1.8	2.4

Table 4.1 lists the rms surface roughness of the Nb (1~10 nm)/Ag films after

annealing at 500 °C and 600 °C. The values further show that the agglomeration makes the surface roughness of the Nb (1 nm)/Ag film become larger after annealing at 600 °C, however, Nb (3~10 nm)/Ag films keep smooth after annealing at 600 °C. By comparison of the surface morphological stability of the Nb/Ag and Ti/Ag films, it is found that the effects of the Nb surface layers with the thickness of 5 nm and above on the agglomeration suppression are slightly better than those of the Ti surface layers judging from the smaller size of the voids.

#### 4.3.2 Electrical resistivity

Figure 4.3 shows the change in the resistivity of Nb (1~10 nm)/Ag films as a function of annealing temperature. Unlike the Ag-Nb alloy films studied previously,<sup>31)</sup> as shown in Fig 1.7, there is no effect of impurity scattering on the resistivity of the Nb (1~10 nm)/Ag films even after annealing at 600 °C, because of no existence of Ag-Nb solid solution or metallic compound in nature.<sup>113)</sup> Therefore, the resistivity of the Nb (1~10 nm)/Ag films is much lower than that of the Ag-Nb alloy films. The resistivity of the as-deposited Nb/Ag films increases slightly with increasing the Nb surface layer thickness, ranging from 2.8 to 3.0  $\mu\Omega$  cm, only because of a little higher bulk resistivity of Nb than that of Ag. However, the change in resistivity with increasing Nb surface layer thickness is found to be much smaller than that of Ti/Ag films by comparing with the previous results, as shown in Fig. 3.4. This is because the bulk resistivity of Nb is much lower than that of Ti as mentioned in Section 4.1. Therefore, it is considered that a material with lower bulk resistivity is more appropriate as the surface layers of the Ag thin films, such as Nb.

The resistivity of all the Nb (1~10 nm)/Ag films decreases after annealing at 500 °C, owing to the improvement in film crystallinity and the relatively smooth film surface. The resistivity of Nb (1 nm)/Ag film increases markedly after annealing at 600 °C, because the occurrence of large voids decreases the conduction area of electrons as a result of its poor thermal stability. However, the Nb (3~10 nm)/Ag films maintains the low resistivity even after annealing at 600 °C, and there is scarcely difference in resistivity between the Nb (3 nm)/Ag and Nb (5 nm)/Ag films. Therefore, from the standpoint of good morphological stability and low electrical resistivity, 5 nm is thought

to be the optimum thickness for the Nb surface layer.

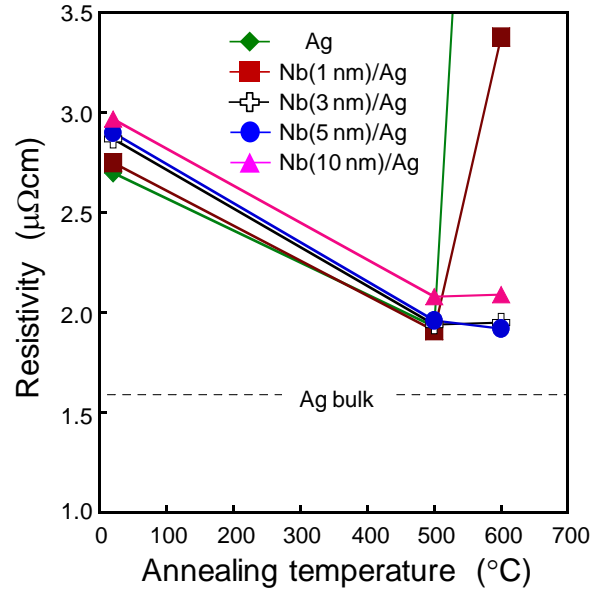


Fig. 4.3 Resistivity of the Ag (100 nm) and Nb (1~10 nm)/Ag films as a function of annealing temperature.

#### 4.3.3 Mechanism of agglomeration suppression caused by Nb surface layer

Similarly to the roles of aluminum or titanium surface layers on Ag films,<sup>69, 75, 78)</sup> the formation of the Nb oxide surface layer is considered to be the main cause for the suppression of Ag agglomeration. The chemical bonding states of the surface layer on the Nb (3 nm)/Ag films before and after annealing at 500 °C were analyzed by XPS, as shown in curves (a) and (b) of Fig. 4.4. The binding energy of the main peaks in both as-deposited and annealed samples is 207.4 eV, which is equal to the reference value of Nb 3d<sub>5/2</sub> in Nb<sub>2</sub>O<sub>5</sub> (207.5 eV).<sup>114)</sup> A few lower valence Nb oxides, such as NbO<sub>2</sub> and NbO, are also detected in the samples.<sup>114, 115)</sup> In addition, a weak peak belonging to the Nb metal<sup>114)</sup> only exists in the as-deposited film. The above results illustrate that most of Nb was oxidized by the natural oxidation before annealing, and the residual Nb was completely oxidized by the oxygen molecules adsorbed on the surface and the residual oxygen in the furnace during annealing. The Nb oxide surface layer is considered to contribute to preventing the drastic migration of Ag atoms during annealing, which

results in the agglomeration suppression.

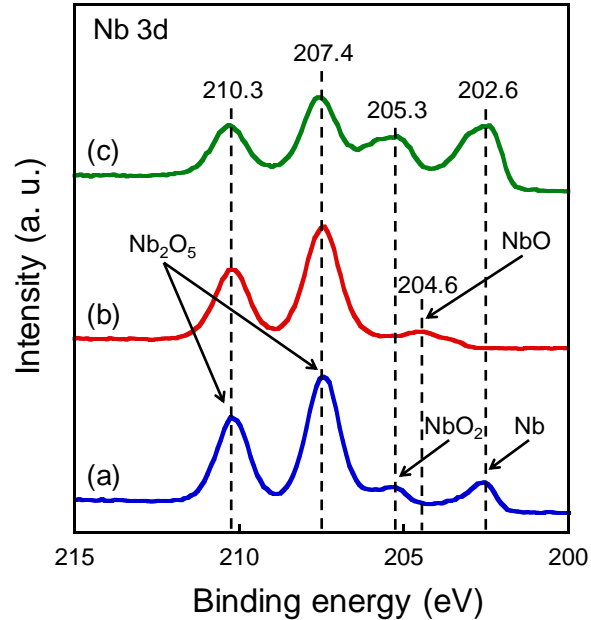


Fig. 4.4 Nb 3d XPS spectra for the surfaces of the films. (a) As-deposited Nb (3 nm)/Ag (100 nm) film, (b) Nb (3 nm)/Ag (100 nm) film annealed at 500 °C in the lamp-heating furnace, and (c) Nb (3 nm)/Ag (50 nm) film annealed at 450 °C in the sputtering chamber.

In order to make clear whether the Nb surface layer in metallic state can effectively suppress the agglomeration of the Ag film, series of extra experiments were executed. Firstly, a 60-nm-thick Nb film was prepared and annealed in the lamp-heating furnace under vacuum to investigate the morphological stability of the Nb thin film. Its SEM image is shown in Fig. 4.5. The result shows that the Nb film after annealing at 600 °C for 1 hour exhibits a quite smooth surface without any void or hillock. Here, we introduce a concept that cohesive energy is the amount of energy required to break the atoms of a solid into isolated atomic species,<sup>116)</sup> which is one of the important physical quantities to quantify the thermal stability of the materials.<sup>116-118)</sup> It is considered that the excellent thermal stability of the pure Nb film is attributed to the much larger cohesive energy of Nb (730 kJ/mol) than that of Ag (248 kJ/mol),<sup>119)</sup> which suggests the Nb atoms are much more difficult to separate from each other than Ag atoms at high temperature. On the basis of the above physical parameter, it is likely that the Nb metal

surface layer would have the same effect on agglomeration suppression as the Nb oxide surface layer, and oxidation might not be necessary for the Nb surface layer to suppress the agglomeration of the Ag film.

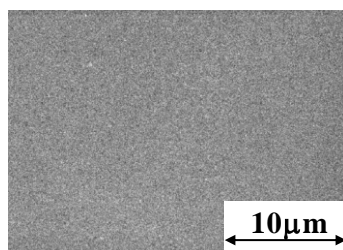


Fig. 4.5 SEM image of the Nb (60 nm) film after annealing at 600 °C.

Next, the additional experiment was designed to confirm the feasibility of the surface layer in metallic state in suppressing the agglomeration of the Ag film. The films of Ag (50 nm) and Nb (3 nm)/Ag (50 nm) were deposited at room temperature. After deposition, in order to prevent the oxidation of the thin Nb layer in air before annealing, the substrate was not taken out but consecutively heated at 450 °C (the extreme temperature of the heater) for 1 hour in the sputtering chamber with the evacuation of below  $1.8 \times 10^{-7}$  Torr. For comparison, another Nb (3 nm)/Ag (50 nm) film was normally deposited and exposed to air before annealing at 450 °C in the lamp-furnace. It is well known that the temperature of agglomeration occurrence decreases with decreasing Ag film thickness.<sup>62, 120)</sup> Because the annealing temperature was set to 450 °C owing to the limitation of the heater in the sputtering chamber, Ag film thickness was fixed to 50 nm to induce agglomeration. Curve (c) in Fig. 4.4 shows that there is a large amount of Nb metal in the surface layer of the Nb (3 nm)/Ag (50 nm) film after annealing in the sputtering chamber. The existence of Nb oxide peaks in the curve is considered to be the result of natural oxidation by exposure to air before XPS analysis. Therefore, it is considered that this Nb surface layer was mainly in metallic state during annealing.

Figure 4.6 shows the SEM images of the Ag (50 nm) and Nb (3 nm)/Ag (50 nm) films directly annealed in the sputtering chamber, and another Nb (3 nm)/Ag (50 nm)

film taken out of the chamber and annealed in the lamp-heating furnace. The Ag (50 nm) film is completely agglomerated after annealing at 450 °C. In contrast, the other Ag films with the Nb metal and Nb oxide surface layers, respectively, exhibit almost the same high thermal stability. It is indicated that the Nb surface layer in metallic state is also capable of suppressing the agglomeration of the underlying Ag film. Therefore, no matter what the state of Nb is, the Nb surface layer is found to be very effective for agglomeration suppression.

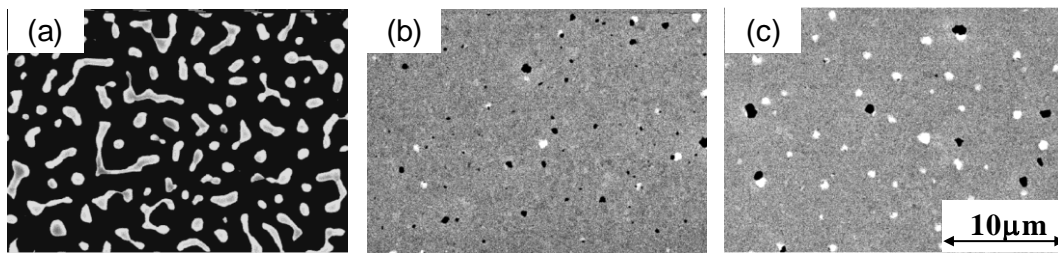


Fig. 4.6 SEM images of the films after annealing at 450 °C. (a) Ag (50 nm) film annealed in the sputtering chamber, (b) Nb (3 nm)/Ag (50 nm) film annealed in the sputtering chamber, and (c) Nb (3 nm)/Ag (50 nm) film annealed in the lamp-heat furnace.

#### 4.3.4 Crystal structure

Figure 4.7 shows XRD patterns of the as-deposited Nb (1~10 nm)/Ag films. All of Nb (1~10 nm)/Ag films show nearly the same XRD patterns as the pure Ag films. There is no distinct difference in the intensity, full width at half maximum, and position of the Ag(111) peaks. Just like the Ti surface layer, the deposition of Nb surface layer is confirmed to have no influence on the crystal structure of the underlying Ag films.

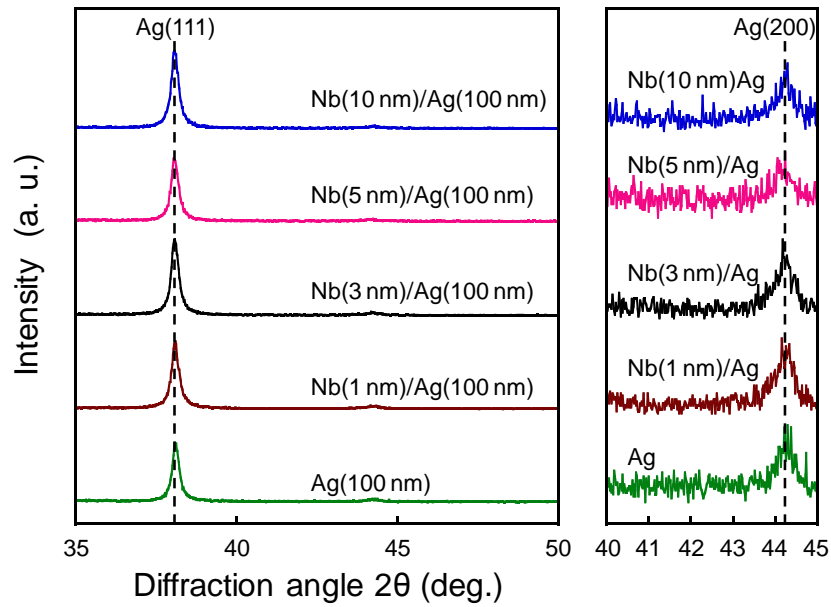


Fig. 4.7 XRD patterns of the as-deposited Ag (100 nm) and Nb (1~10 nm)/Ag films.

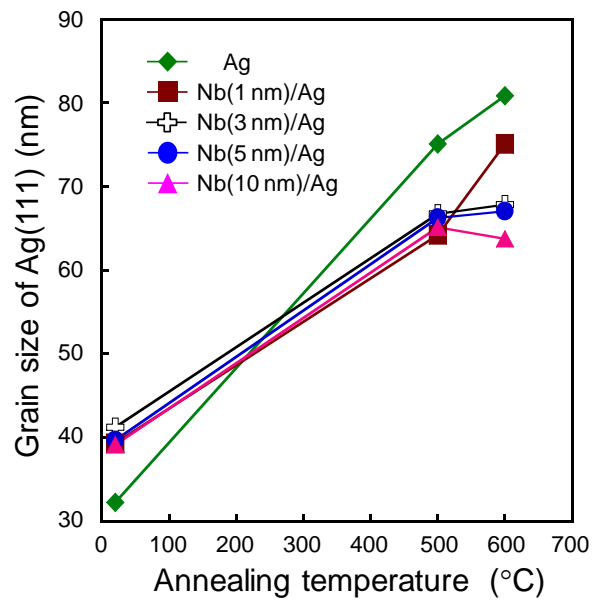


Fig. 4.8 Grain size of Ag(111) for the Ag (100 nm) and Nb (1~10 nm)/Ag films as a function of annealing temperature.

In order to determine the degree of Ag(111) grain growth in the Nb/Ag films, the grain size of Ag(111) in Ag (100 nm) film and Nb (1~10 nm)/Ag films as a function of

annealing temperature was compared. The result is shown in Figure 4.8. It is clear that the overgrowth of the Ag(111) grains during annealing could be suppressed by the Nb surface layers with the thickness of 3 nm and above. It is considered that the efficient suppression of the surface diffusion, owing to the Nb surface layers, has resulted in slowing down the mass transport, which limits the grain growth.

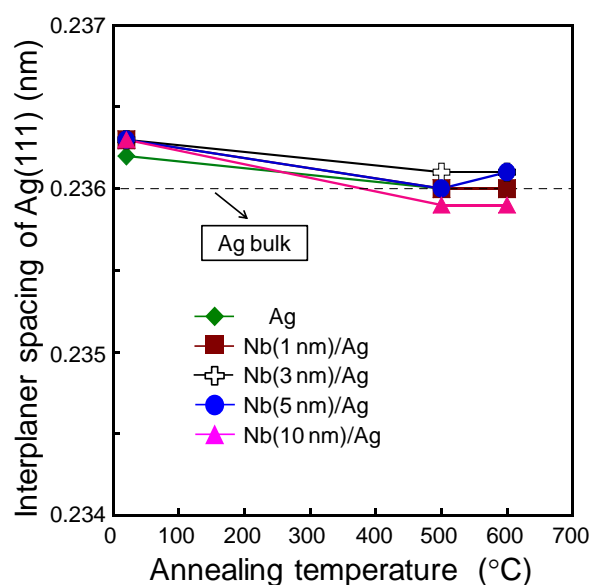


Fig. 4.9 Interplanar spacing of Ag(111) for the Ag (100 nm) and Nb (1~10 nm)/Ag films as a function of annealing temperature.

Then, the interplanar spacing of Ag(111) in the Nb/Ag films as a function of annealing temperature was investigated to make sure whether solution or reaction occurred between the Nb surface layers and the Ag films. As shown in Fig. 4.9, it is found that the interplanar spacing of Ag(111) for the Nb (1~10 nm)/Ag films barely change with increasing the annealing temperature as well as the Ag film. Therefore, as expected, the Nb surface layers have not dissolved in the Ag films.

In conclusion, the Nb surface layers show the similar effects on agglomeration suppression as the Ti surface layers, but the effect of the Nb surface layer on the resistivity is smaller than that of the Ti surface layer. Thus, Nb nano-layers are considered to be more appropriate for the surface layer of the Ag films. In addition, a 5-nm-thick Nb surface layer is proved to be optimum judging from the balance of good

thermal stability and low resistivity.

## **4.4 Ag film with Nb interface layer (Ag/Nb film)**

### **4.4.1 Surface morphology**

Figure 4.10 shows the SEM images of the Ag/Nb (1~10 nm) films before and after annealing. The surfaces of all the as-deposited films appear to be very flat. After annealing at 500 °C, the surfaces of all the films seem much rougher. However, it is difficult to find the existence of the voids in any Ag/Nb film. After annealing at 600 °C, the Ag/Nb (1~10 nm) films show high thermal stability because of the much fewer and smaller voids than the annealed Ag single layer film. Among the Ag/Nb (1~10 nm) films, the Ag/Nb (1 nm) film shows more voids than others, and Ag/Nb (3~10 nm) films exhibit nearly the same good surface morphology. Therefore, it is considered that a 1-nm-thick Nb interface layer is not enough to effectively suppress the agglomeration of the Ag films, but the Nb interface layer with 3 nm and above could greatly improve the thermal stability of the Ag films. However, as compared with Fig. 3.10, the size of the voids with diameter of approximately 6 nm in the Ag/Nb (3~10 nm) films is a little larger than that of the Ag/Ti (3~10 nm) films (approximately 3 nm of their diameter). It is suggested that the effect of the Ti interface layers is slightly better than that of the Nb interface layers.

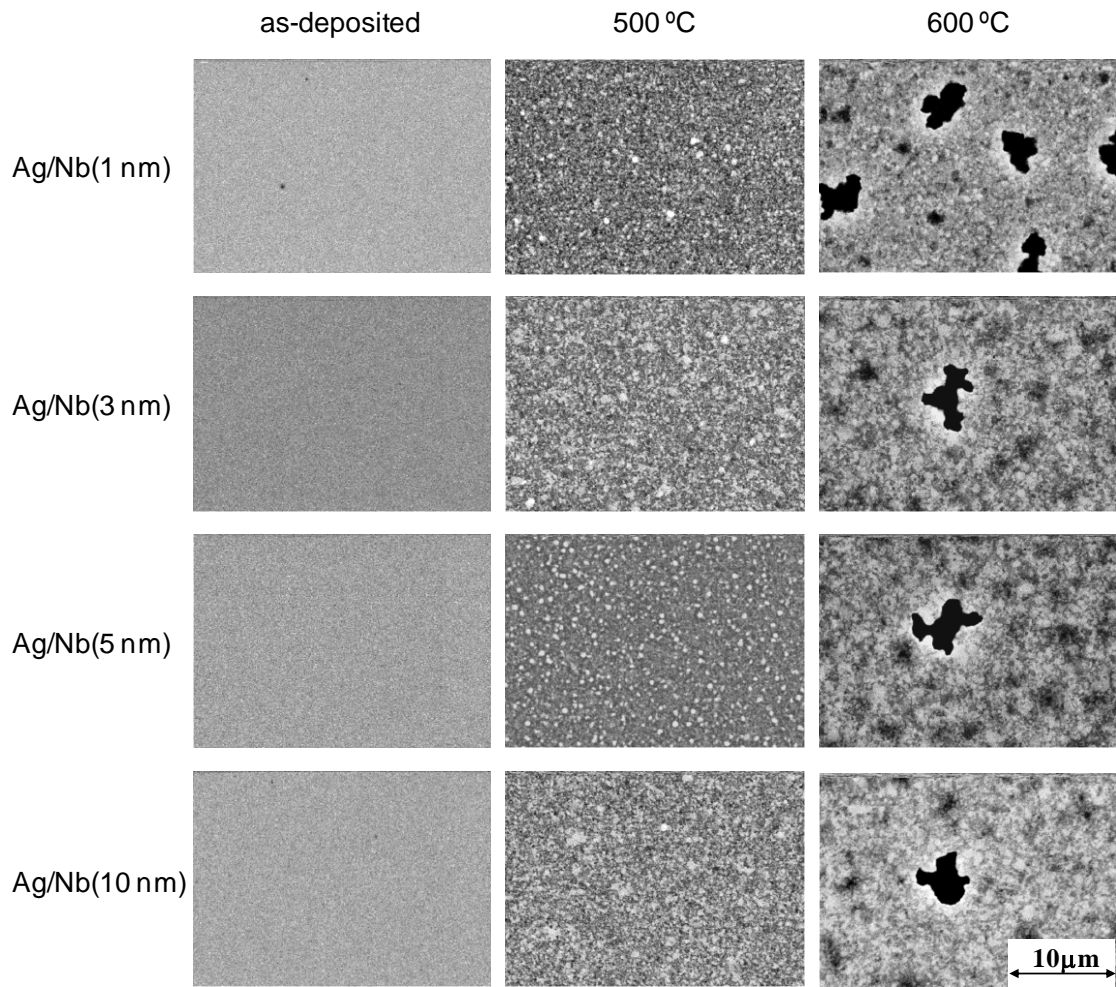


Fig. 4.10 SEM images of the Ag/Nb (1~10nm) films before and after annealing.

In addition, the rms roughness of the Ag/Nb (1~10 nm) films after annealing at 500 °C and 600 °C was investigated using AFM, as shown in Table 4.2. From the comparison with Table 4.1, it is found that the Ag/Nb (3~10 nm) films are much rougher than the Nb (3~10 nm)/Ag films, which indicates that the role of Nb surface layers in agglomeration suppression is more important than that of the Nb interface layers. On the other hand, according to the comparison with the Ti interface layer, as shown in Table 3.2, Ag/Nb (3~10 nm) films are a bit rougher than the Ag/Ti (3~10 nm) films. Therefore, the Ti nano-layer appears to be more suitable for the interface layer caused by its better effects on the improvement of the thermal stability of the Ag films.

Table 4.2 The surface roughness of the Ag/Nb (1~10 nm) films after annealing at 500 °C and 600 °C.

Rms roughness (nm)		
	500 °C	600 °C
Ag/Nb (1 nm)	5.4	5.2
Ag/Nb (3 nm)	3.9	5.5
Ag/Nb (5 nm)	4.2	5.4
Ag/Nb (10 nm)	3.7	5.6

#### 4.4.2 Electrical resistivity

Figure 4.11 shows the change in the resistivity of Ag/Nb (1~10 nm) films as a function of annealing temperature. The resistivity of the as-deposited Ag/Nb (1 nm) film shows almost the same resistivity to the as-deposited Ag film. However, the resistivity of the as-deposited Ag/Nb (3~10 nm) films is a little lower than that of the as-deposited Ag film, which is the same as the phenomenon described in Section 3.4.2. But the resistivity of the Ag/Nb (3~10 nm) films is a little higher than that of the Ag/Ti (3~10 nm) films, as shown in Fig. 3.11. The reason for the above phenomenon will be discussed in the next section.

After annealing at 500 °C, the resistivity of all the Ag/Nb (1~10 nm) films decreases due to their continuous surfaces and the improvement in the crystallinity. After annealing at 600 °C, the resistivity of the Ag/Nb (1~10 nm) films increased slightly to 2.2~2.4  $\mu\Omega$  cm owing to the slight agglomeration, and is higher than that of the corresponding Ti/Ag films (2.1~2.2  $\mu\Omega$  cm). Overall, the Nb interface layer is useful to achieve the low resistivity after annealing, but is a little inferior to the Ti interface layer.

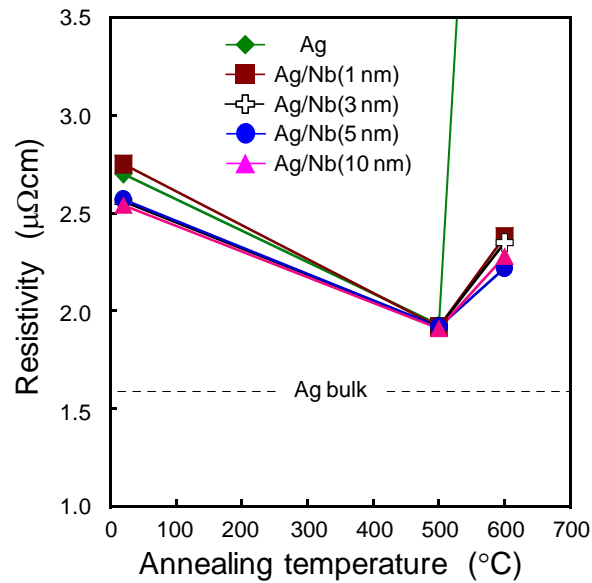


Fig. 4.11 Resistivity of the Ag (100 nm) and Ag/Nb (1~10 nm) films as a function of annealing temperature.

#### 4.4.3 Adhesion strength of Ag/Nb film to SiO<sub>2</sub> substrate

Nb possesses a large affinity to oxygen as well as Ti. Therefore, Nb interface layers have been also considered to be useful for the improvement of the adhesion between the films and the SiO<sub>2</sub> substrates. The critical delamination load of the as-deposited Ag/Nb films was investigated by the micro-scratch testing, and the result is shown in Fig. 4.12. It shows that the critical delamination load increases to approximately four times larger than that of the Ag film deposited on the SiO<sub>2</sub> substrate after inserting a Nb interface layer with the thickness of 1 nm or above. The result represents the promotion of the adhesion between the Ag films and the SiO<sub>2</sub> substrates owing to the Nb interface layers, and it is considered to be one of the causes for the improvement in the thermal stability of the Ag films.

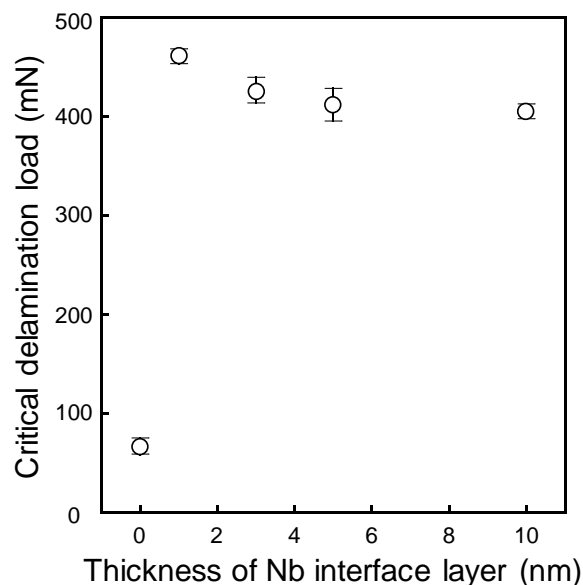


Fig. 4.12 Critical delamination load of the as-deposited Ag (100 nm) and Ag/Nb (1~10 nm) films.

#### 4.4.4 Crystal structure

Figure 4.13 shows XRD patterns of the as-deposited Nb (60 nm), Ag (100 nm) and Ag/Nb (1~10 nm) films. The Ag/Nb (1 nm) film shows the similar XRD pattern to the Ag film having both Ag(111) and Ag(200) peaks. However, the intensity of the Ag(200) peak reduces with increasing the thickness of the Nb interface layer, and it disappears completely with the Nb interface layer of 3nm and above, followed by the enhancement in the intensity of the Ag(111) peak. It is indicated that Nb interface layers with the thickness of 3 nm and above have significantly affected the atomic arrangement of the overcoating Ag films, and the Ag/Nb (3~10 nm) films show single orientation of Ag (111). The change in the intensity of the Ag(111) and Ag(200) of the Ag films with increasing the Nb interface layers is quite similar to that of the Ag/Ti films, as compared with Fig. 3.13. However, it was found that the Ag(111) peak intensity of the Ag/Nb (3~10 nm) films is lower than that of the Ag/Ti (3~10 nm) films.

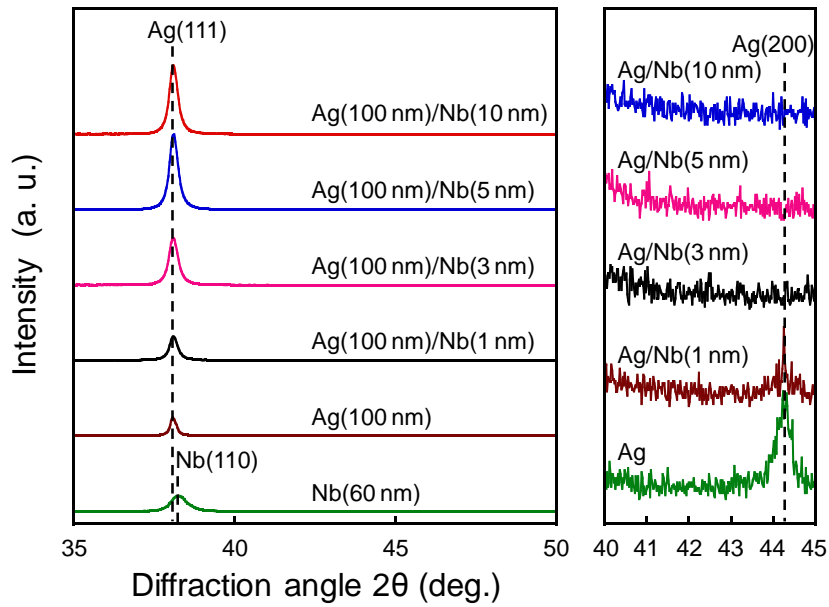


Fig. 4.13 XRD patterns of the as-deposited Ag (100 nm) and Ag/Nb (1~10 nm) films.

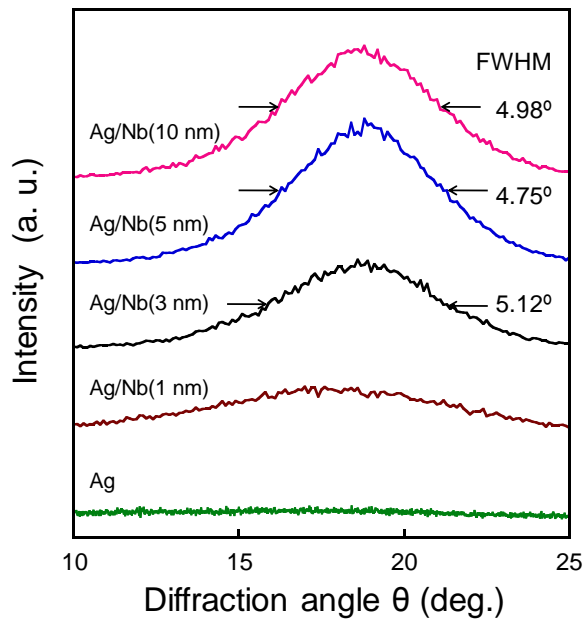


Fig. 4.14 XRD rocking curves of the as-deposited Ag (100 nm) and Ag/Nb (1~10 nm) films.

Then, the crystalline orientation of Ag(111) in the as-deposited Ag and Ag/Nb films was investigated using XRD rocking curve measurement, as shown in Fig. 4.14. The peaks for the Ag and Ag/Nb (1 nm) films are not outstanding. The Ag(111) peaks of the

Ag/Nb (3~10 nm) films abruptly become narrow and high, and the FWHM for those peaks are almost the same, but larger than that of the Ag(111) peaks in the Ag/Ti (3~10 nm). It is indicated that a 1-nm-thick Nb interface layer is not sufficient to completely change the crystalline orientation of the overlying Ag film, in contrast, the Nb interface layers with 3 nm and above can improve the crystalline orientation of Ag(111), but the effect is less than that of the Ti interface layers.

As the one cause for the agglomeration suppression, the improvement in the crystalline orientation of Ag(111) owing to the Nb interface layers have contributed to the improvement in the thermal stability of the Ag films. Meanwhile, the reduction of the resistivity of the as-deposited Ag/Nb (3~10 nm) films is also thought to be attributed to the improvement in the crystalline orientation of Ag(111). On the other hand, although the improvement in the adhesion of the Ag/Nb films is almost the same as the Ag/Ti films, the crystalline orientation of Ag(111) of the Ag/Ti (3~10 nm) films is higher than that of the Ag/Nb (3~10 nm) films, and thus the effect of the Nb interface layer on the thermal stability and resistivity are less than that of the Ti interface layer.

Next, the mechanism of the change in the crystalline orientation of Ag(111) caused by the Nb interface layer is discussed. The Nb (60 nm) film displays the single peak of Nb(110), which is the closest-packed plane of the Nb body-centered cubic (bcc) structure, as shown in Figure 4.13. Whereas, the Ag films has fcc structure, and its closest-packed plane is Ag(111). The epitaxial growth of fcc(111) on bcc(110) has been reported, though the atomic arrangement of the (110) plane is different to that of the (111) plane.<sup>121, 122)</sup>

Theoretical models using the rigid lattice approximation predict the epitaxial relationship between fcc(111) and bcc(110).<sup>123-125)</sup> Experimental investigations have usually found the predicted orientation,<sup>126)</sup> i.e., either the Nishiyama-Wassermann (NW)<sup>127, 128)</sup> or the Kurdjumov-Sachs (KS)<sup>129)</sup> epitaxial relationship, as shown in Fig. 4.15. Calculations of the interface energy, as a function of the atomic diameter ratio  $d_{\text{bcc}} / d_{\text{fcc}}$ , in the rigid lattice approximation, have found that the minima appears at those ratios where parallel atomic rows of the two lattice planes have exactly the same distance. For the NW case, the optimal ratio is at  $d_{\text{bcc}} / d_{\text{fcc}} = \sqrt{3} / 2 = 0.866$  or  $d_{\text{bcc}} / d_{\text{fcc}} = 3\sqrt{2} / 4 = 1.061$ , whereas for the KS case it is at  $d_{\text{bcc}} / d_{\text{fcc}} = 3\sqrt{6} / 8 = 0.919$ . For

atomic diameter ratios close to one of the minima, one usually takes on the corresponding orientation.<sup>126)</sup> Because the atomic diameters of Nb and Ag are 0.286 nm and 0.289 nm, respectively,<sup>130)</sup> and  $d_{\text{bcc}} / d_{\text{fcc}} = 0.286 / 0.289 = 0.990$  is closed to both 1.061 and 0.919, Ag(111) on Nb(110) is possible to grow in the way of NW or/and KS orientation. Therefore, the Nb interface layers have improved the crystalline orientation of Ag(111) of the Ag/Nb films. On the other hand, any three neighboring atoms form an equilateral triangle at the close-packed plane of Ti(0002) and Ag(111), as shown in Fig. 3.15, whereas three neighboring atoms form an isosceles triangle with a differently long base at the the closest-packed plane of Nb(110), as shown in Fig. 4.15. The overlap of Ag(111) on Ti(0002) is more coincident than that of the Ag(111) on Nb(110), so it is easier for Ag atoms to arrange in way of (111) plane on Ti(0002) than Nb(110) under the same deposition conditions. Consequently, the Ti interface layers are more effective in improving the crystalline orientation of Ag(111) of the Ag films, as compared with Fig. 3.14 and Fig. 4.14.

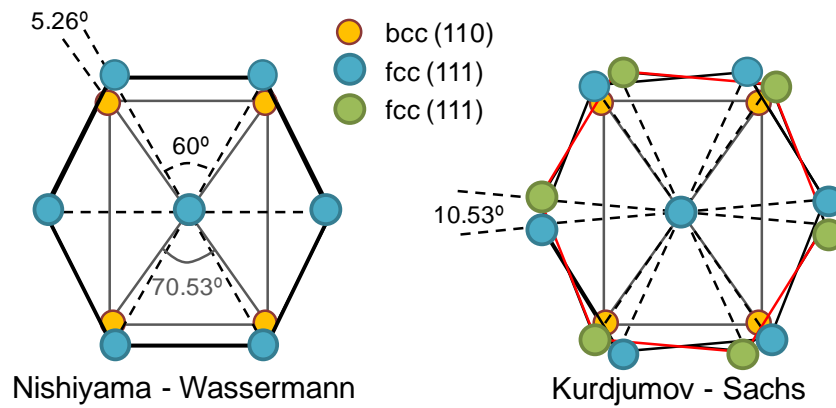


Fig. 4.15 NW and KS epitaxial relationship of fcc(111)/bcc(110) interface.

Figure 4.16 shows the grain size of Ag(111) in Ag/Nb (1~10 nm) films as a function of annealing temperature. It is found that the introduction of the Nb interface layers restrains the overgrowth of the Ag(111) grains, which contributes to the agglomeration suppression.

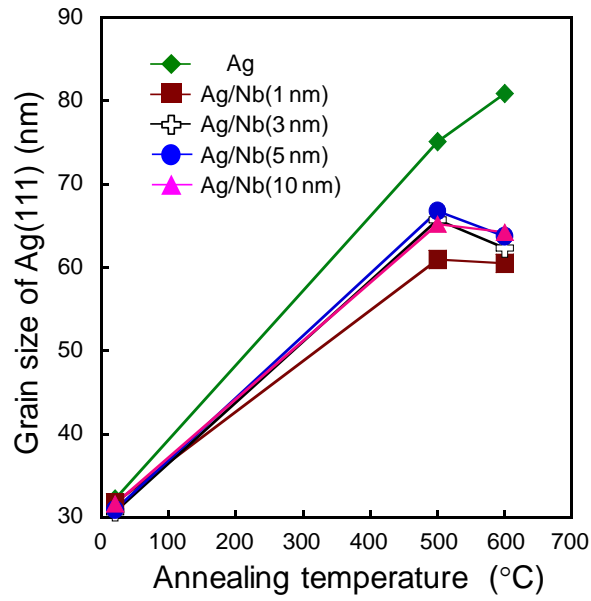


Fig. 4.16 Grain size of Ag(111) for the Ag (100 nm) and Ag/Nb (1~10 nm) films as a function of annealing temperature.

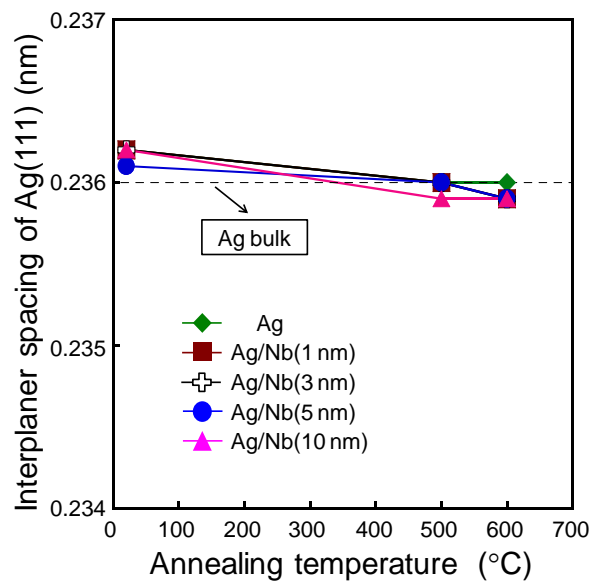


Fig. 4.17 Interplanar spacing of Ag(111) for the Ag (100 nm) and Ag/Nb (1~10 nm) films as a function of annealing temperature.

Figure 4.17 shows the interplanar spacing of Ag(111) for Ag/Nb (1~10 nm) films as a function of annealing temperature. The interplanar spacing of Ag(111) after annealing

hardly changes even after annealing at 600 °C by inserting the Nb interface layers. It is indicated that, just like the Nb surface layers, the Nb interface layers and the Ag layers do not react or form solid solution.

## **4.5 Nb/Ag/Nb triple-layer film**

The results above have shown that the 5-nm-thick Nb surface layer and the Nb interface layer with the thickness of 3 nm or above are able to suppress the agglomeration of the Ag films effectively. In this section, we discuss the thermal stability and the electrical resistivity of the triple-layer structure of Nb/Ag/Nb films.

### **4.5.1 Surface morphology**

Figure 4.18 shows the SEM images of the Nb (5 nm)/Ag/Nb (3 nm) and Nb (5 nm)/Ag/Nb (5 nm) films after annealing at 500 °C and 600 °C. It is observed that the surface morphology of the Nb (5 nm)/Ag/Nb (3 nm) and Nb (5 nm)/Ag/Nb (5 nm) films after annealing at 500 °C or 600 °C is almost the same. It is further proved that the Nb interface layers with the thickness of 3 nm and above show the similar effect on the improvement in thermal stability of the Ag films. After annealing at 500 °C, the Nb/Ag/Nb films exhibit smooth surfaces, except a few small voids. After annealing at 600 °C, a very few voids become a little larger, but the surfaces are basically kept very flat. After comparing to the surface morphology of the Nb/Ag (Fig. 4.2) and Ag/Nb (Fig. 4.10) double-layer films after annealing, it is found that the Nb/Ag/Nb triple-layer films show better thermal stability due to the fewer and smaller voids. Therefore, the combined effect of the Nb surface layer and interface layer is approved.

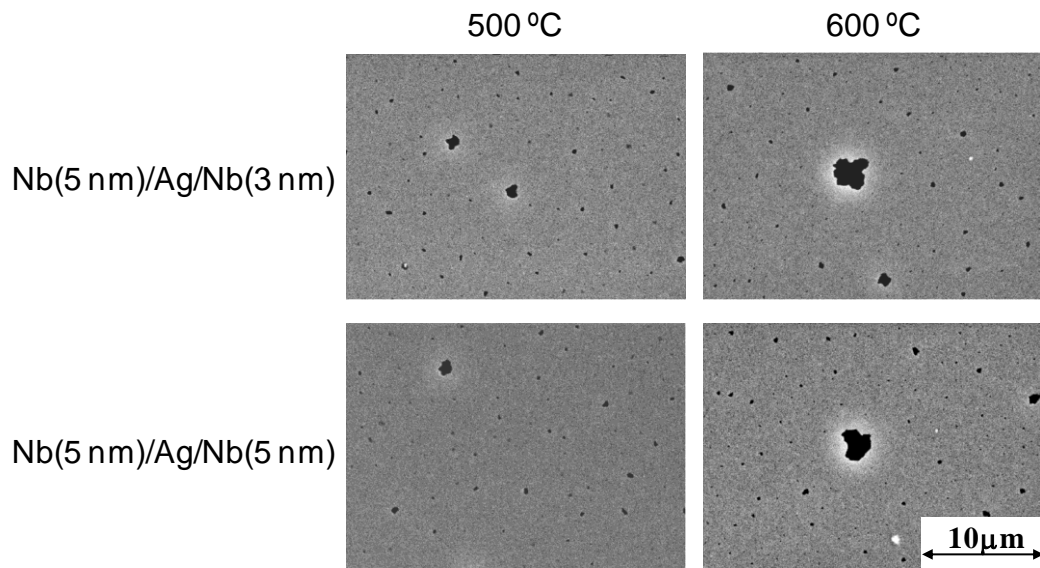


Fig. 4.18 SEM images of the Nb (5 nm)/Ag/Nb (3 nm) and Nb (5 nm)/Ag/Nb (5 nm) films after annealing at 500 °C and 600 °C.

#### 4.5.2 Electrical resistivity

The resistivity of the Nb (5 nm)/Ag/Nb (3 nm) and Nb (5 nm)/Ag/Nb (5 nm) films as a function of annealing temperature is shown in Fig. 4.19. It is found that the Nb (5 nm)/Ag/Nb (3 nm) and Nb (5 nm)/Ag/Nb (5 nm) films hold almost the same low resistivity before and after annealing. After annealing at 500 °C or 600 °C, their resistivity decreases to approximately 2.1  $\mu\Omega$  cm, owing to the good result of agglomeration suppression.

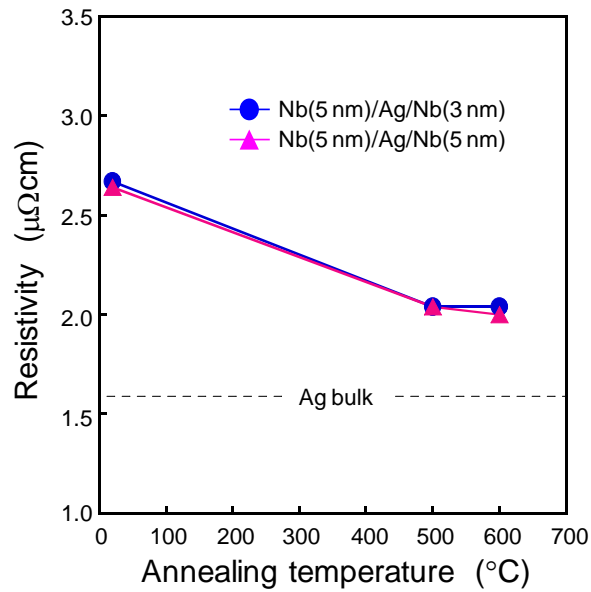


Fig. 4.19 Resistivity of the Nb (5 nm)/Ag/Nb (3 nm) and Nb (5 nm)/Ag/Nb (5 nm) films as a function of annealing temperature.

#### 4.6 Optimization for triple-layer structure

On the basis of the previous discussion, it has been discovered that Nb and Ti nano-layers are more suitable for surface layer and interface layer of the Ag film. The 5-nm-thick Nb surface layer and 3-nm-thick Ti interface layer have been confirmed to be sufficient for the improvement in the overall performance of the Ag films. Therefore, the Nb (5 nm)/Ag/Ti (3 nm) multilayered film has been prepared in this study. Although the Nb/Ag/Nb and Ti/AgTi films exhibit good surface morphology and low resistivity after annealing, the triple-layer structure of Nb/Ag/Ti is expected to display better effects on the improvement in thermal stability and the maintenance of the low resistivity.

The morphological stability and electrical resistivity of the Nb (5 nm)/Ag/Ti (3 nm), Nb (5 nm)/Ag/Nb (5 nm), and Ti (3 nm)/Ag/Ti (3 nm) films were evaluated and compared. Figure 4.20 shows the SEM images of the Nb (5 nm)/Ag/Ti (3 nm), Nb (5 nm)/Ag/Nb (5 nm), and Ti (3 nm)/Ag/Ti (3 nm) films after annealing at 600 °C, and Fig. 4.21 gives the resistivity of these triple-layer films as a function of annealing temperature. It is found that the Nb (5 nm)/Ag/Ti (3 nm) film shows the highest

morphological stability and the lowest resistivity in all the triple-layer films. Nb (5 nm)/Ag/Ti (3 nm) is confirmed to be the best combination. Therefore, it is considered that Ag films with different materials of more appropriate surface and interface layers could obtain a higher thermal stability and a lower electrical resistivity than Ag films with the same materials of surface and interface layers.

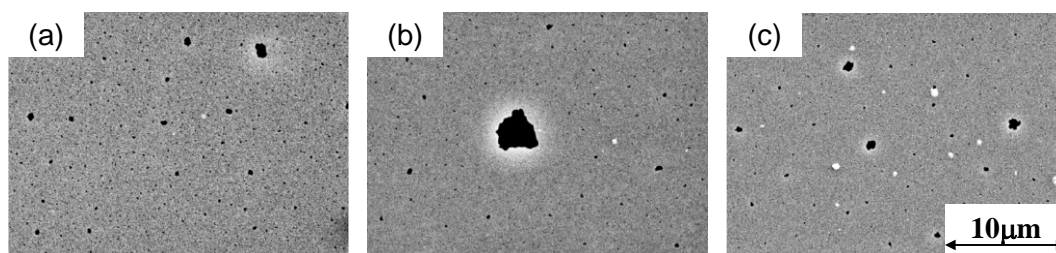


Fig. 4.20 SEM images of the triple-layer films after annealing at 600 °C. (a) Nb (5 nm)/Ag (100 nm)/Ti (3 nm), (b) Nb (5 nm)/Ag (100 nm)/Nb (5 nm), and (c) Ti (3 nm)/Ag (100 nm)/Ti (3 nm) films.

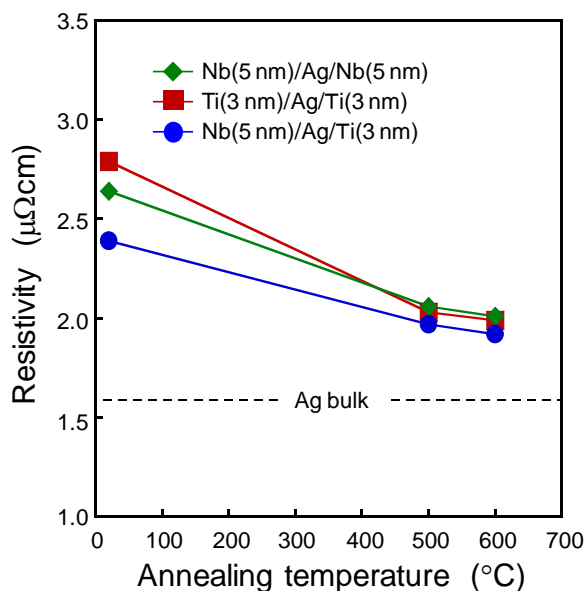


Fig. 4.21 Resistivity of the Nb (5 nm)/Ag/Nb (5 nm), Ti (3 nm)/Ag/Ti (3 nm), and Nb (5 nm)/Ag/Ti (3 nm) films as a function of annealing temperature.

## 4.7 Summary

The morphological stability of the Nb/Ag films is a little better than that of the Ti/Ag films. The Nb surface layer with lower bulk resistivity has smaller influence on the sheet resistance of the multilayered Ag film than the Ti surface layer. Therefore, the Nb surface layer is superior to the Ti surface layer. From the standpoint of thermal stability and electrical resistivity, the 5-nm-thick Nb layer is found to be an appropriate capping layer. In addition, it is confirmed that the Nb surface layer, regardless of the chemical state of metal or oxide, effectively suppresses the agglomeration of Ag film during annealing.

As well as the Ti interface layers, the Nb interface layers with the thickness of 3 nm and above could improve the adhesion of the Ag films on SiO<sub>2</sub> substrates and the crystalline orientation of Ag(111), which contribute to the low resistivity and relatively good thermal stability. However, the effect of the Nb interface layers is less than the Ti interface layers. Therefore, the Ti nano-layer is considered to be more appropriate for the interface layer.

The combined effect of the Nb surface layer and Nb interface layer on achieving both good thermal stability and low electrical resistivity has been approved. However, it is confirmed that the triple-layer structure of Nb (5 nm)/Ag/Ti (3 nm) is superior to Nb (5 nm)/Ag/Nb (5 nm) and Ti (3 nm)/Ag/Ti (3 nm) films. It is indicated that the different materials of more appropriate surface and interface layers could bring about a higher thermal stability and a lower electrical resistivity in Ag films than the same materials of surface and interface layers.

# Chapter 5 Effects of Pd Surface Layer and Interface Layer on Thermal Stability and Electrical Properties of Ag Thin Film

## 5.1 Introduction

Since the Nb surface layer in metallic state was proved to be effective in suppressing the agglomeration of the Ag films, the further study on the effects of various surface layers in metallic state on thermal stability and electrical properties of the Ag film has attracted more attentions. Pd with very low free energy of formation of oxide ( $\Delta_f G^\circ_{\text{PdO}} = -55.4 \text{ kJ/mol}$ )<sup>68)</sup> and low cohesive energy (730 kJ/mol)<sup>119)</sup>, was selected as surface layer in this study.

On the other hand, we want to investigate whether the crystalline orientation of Ag(111) can be improved by a Pd interface layer, owing to Pd with the same face-centered cubic crystal structure as Ag. In addition, we also want to confirm that the Pd interface layer would have little influence on the adhesion of the Ag film to the SiO<sub>2</sub> substrate, caused by the poor affinity of Pd to oxygen.

However, it is well known that Ag and Pd can form complete solid solution at high temperature, as the Ag-Pd binary phase diagram is shown in Fig. 5.1.<sup>131)</sup> Therefore, it is not sure that the multilayered structure of the Ag films with the Pd surface layers or interface layers can improve their thermal stability, and maintain the low resistivity. This chapter focuses primarily on describing the effect of high temperature solid solution on the thermal stability and resistivity of the Pd/Ag and Ag/Pd films. In addition, the effects of other properties of Pd are also discussed in some detail.

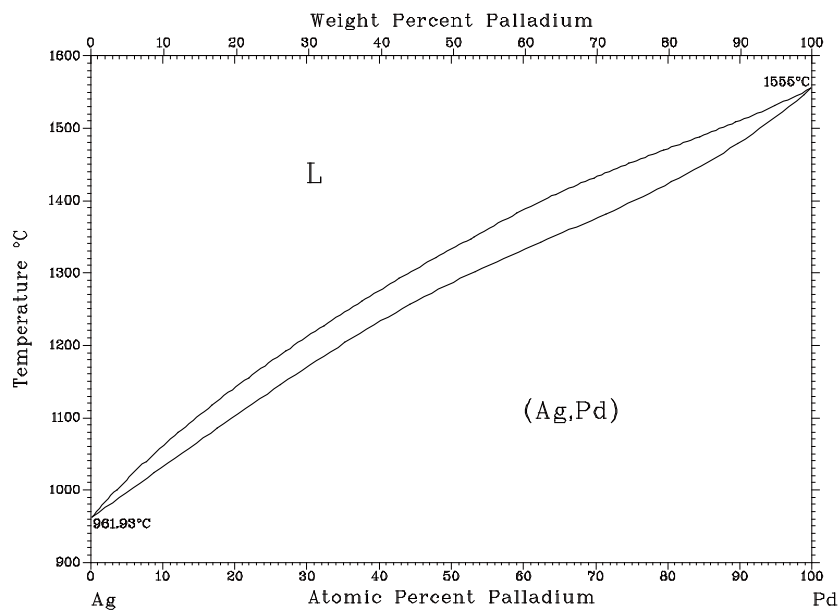


Fig. 5.1 Ag-Pd binary phase diagram. <sup>131)</sup>

## 5.2 Experimental procedure

The Pd (60 nm), Pd (1~5 nm)/Ag, and Ag/Pd (1~5 nm) films were deposited using RF magnetron sputtering, and then annealed under vacuum. The structure of the multilayered films is shown in Fig. 5.2. The preparation conditions, heat treatment conditions, and evaluation methods have been described in Chapter 2.

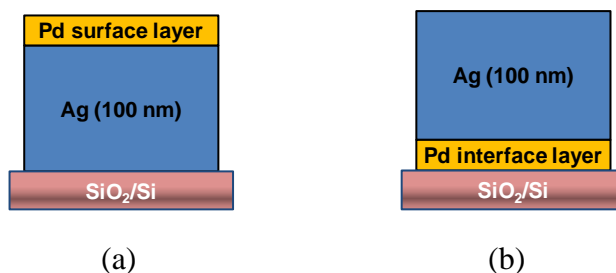


Fig. 5.2 Structure of the multilayered films deposited using RF magnetron sputtering. (a) Pd/Ag film, and (b) Ag/Pd film.

### 5.3 Ag film with Pd surface layer (Pd/Ag film)

#### 5.3.1 Surface morphology

The surface morphology of the Pd (1~5 nm)/Ag films before and after annealing were observed using SEM, as shown in the Fig. 5.3. The surfaces of as-deposited Pd/Ag films are very smooth as well as the as-deposited Ti/Ag and Nb/Ag films, as compared with Fig. 3.2 and Fig 4.2. However, after annealing at 500 °C, all the films exhibit similarly rough surfaces with a large amount of voids and hillocks. After annealing at 600 °C, the surfaces of all the Pd (1~5 nm)/Ag films shows growth of voids and hillocks, but they are still better than that of the Ag film. In addition, it is found that the surface morphology of the Pd/Ag films is not improved remarkably with any thickness of the Pd surface layer.

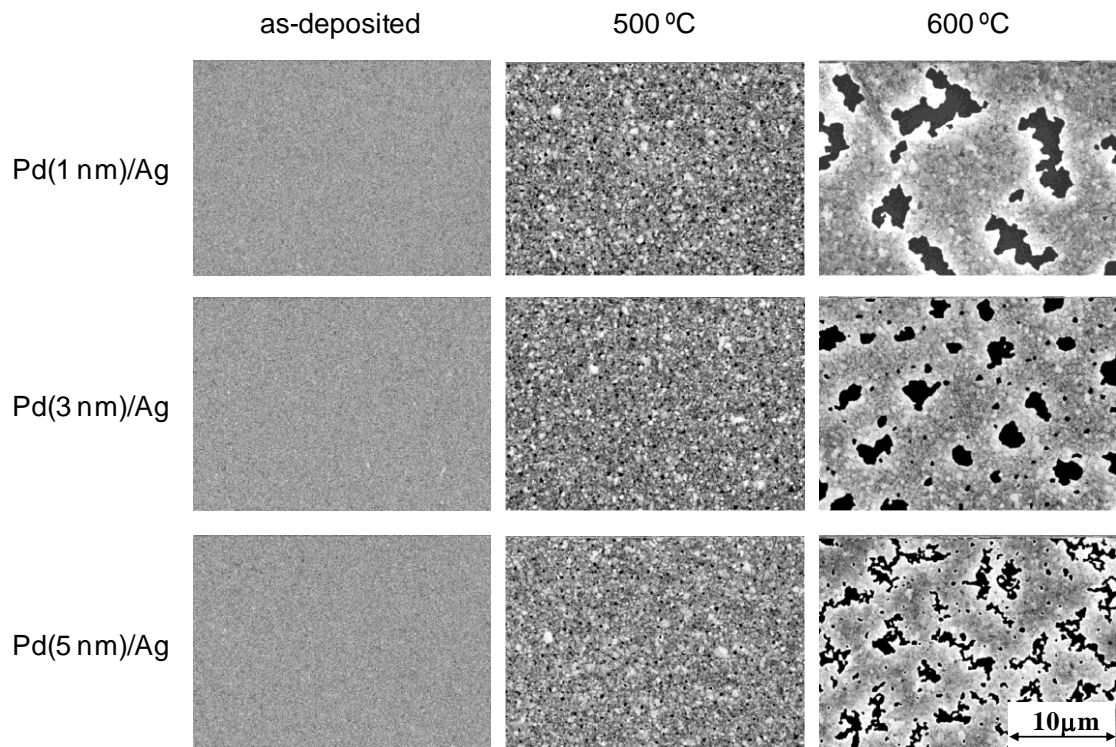


Fig. 5.3 SEM images of the Pd (1~5 nm)/Ag films before and after annealing.

The rms roughness of the surfaces of the Pd (5 nm)/Ag films after annealing at 500 °C and 600 °C was measured using AFM, and they were 8.4 nm and 20.1 nm,

respectively. The rough surfaces similar to those of the agglomerated Ag films further indicate the poor effect of the Pd surface layer on agglomeration suppression. These results demonstrate that the thermal stability of the Ag films is hardly improved satisfactorily by covering a Pd surface layer.

### 5.3.2 Electrical resistivity

The change in the resistivity of the Pd/Ag films as a function of annealing temperature is shown in Fig. 5.4. Although the resistivity of the as-deposited Pd (1~5 nm)/Ag films increases slightly with increasing the thickness of the Pd surface layer, they show the low values below  $3.0 \mu\Omega \text{ cm}$ . As compared with Fig 3.4, the thickness of the Pd surface layer has smaller influence on the resistivity of the as-deposited Ag films than the Ti surface layer. It is considered that the surface layer with low bulk resistivity, such as Pd ( $\rho = 10.8 \mu\Omega \text{ cm}$  at 293 K) and Nb ( $\rho = 12.5 \mu\Omega \text{ cm}$  at 293 K), is more appropriate for the maintenance of the low resistivity of the as-deposited Ag film.

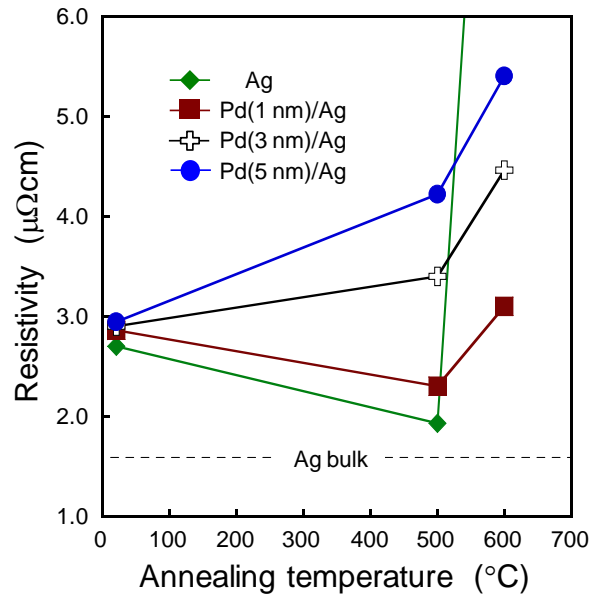


Fig. 5.4 Resistivity of the Ag (100 nm) and Pd (1~5 nm)/Ag films as a function of annealing temperature.

After annealing at 500 °C, all the Pd/Ag films show higher resistivity than the Ag single layer film, and the resistivity of the Pd/Ag films increases regularly with increasing the thickness of the Pd surface layer. After annealing at 600 °C, all the Pd/Ag films exhibit much higher resistivity, though they do not show the resistivity as high as that of the Ag film, owing to the slight improvement in the thermal stability. And the resistivity of the Pd/Ag films also increases regularly with increasing the thickness of the Pd surface layer. The increase of the resistivity of the Pd (1~5 nm)/Ag films with increasing the annealing temperature and the thickness of the Pd surface layer is considered to be mainly dependent on the Pd atoms dissolved in the Ag films, which cause the impurity scattering effect. The details about solid solution are described in the following.

### 5.3.3 Chemical bonding state of the surface

The chemical bonding state of the surface of the Pd (5 nm)/Ag film before and after annealing at 500 °C was investigated using XPS, as shown in Fig. 5.5. It is found that the positions of the main peaks do not shift after annealing, and the binding energy of Pd 3d<sub>5/2</sub> is 335.1 eV, which is the same as the reference value for Pd in metallic state.<sup>132)</sup> It is indicated that the Pd surface layer has not been oxidized before and after annealing, which is corresponding to the low Gibbs free energy for Pd oxide formation. Although we have already confirmed that some surface layer in metallic state can effectively suppress the agglomeration of the Ag film, such as Nb, it has been found that the Pd surface layer in metallic state is not very useful.

On the other hand, according to the further observations from Fig. 5.5, the obvious reduction of the intensity of the peaks after annealing at 500 °C illustrates the reduction of the amount of Pd at the surface, which ought to be caused by the solution of Pd in Ag film. The formation of the Ag-Pd solid solution would impair the ability of the Pd surface layer to agglomeration suppression, and increase the resistivity of the Ag film.

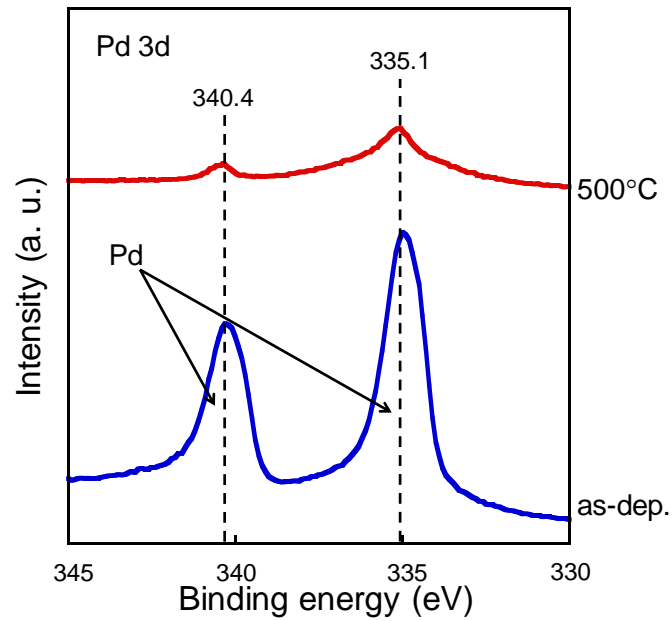


Fig. 5.5 Pd 3d XPS spectra for the surfaces of the Pd (5 nm)/Ag films before and after annealing at 500 °C.

### 5.3.4 Morphological stability of Pd

Figure 5.6 shows the SEM image of the Pd (60 nm) film before and after annealing at 600 °C. It is interesting that, although the Pd film does not agglomerate as severely as the pure Ag film, the much rougher surface than that of the annealed Nb film, as compared with Fig. 4.5 of the previous chapter, shows the poor morphological stability of Pd. The poor morphological stability weakens the capability of the Pd surface layer to suppress the surface diffusion of the Ag atoms.

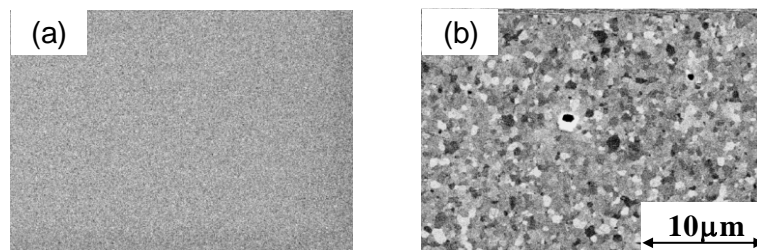


Fig. 5.6 SEM images of the as-deposited Pd (60 nm) film (a) and the one after annealing at 600 °C (b).

By comparison with the cohesive energy of Ag, Nb, and Pd and their morphological stability, as shown in Fig. 1.3, Fig. 4.5, and Fig. 5.6, respectively, the relationship between the cohesive energy and the morphological stability could be made clear. The cohesive energy of Pd (376 kJ/mol) is a little higher than that of Ag (248 kJ/mol), but much lower than that of Nb (730 kJ/mol).<sup>119)</sup> Correspondingly, the morphological stability of Pd is better than that of Ag, but much worse than that of Nb. Therefore, it is considered that a surface layer in a metallic state with low cohesive energy is difficult to keep flat and continuous at high temperature, which is useless to suppress the agglomeration of Ag. This point would be helpful to select suitable materials for the surface layers of the Ag films.

### **5.3.5 Solid solubility of Pd in Ag film**

In order to study the solid solubility of Pd in Ag as a function of annealing temperature, the interplanar spacing of Ag(111) for the pure Ag (100 nm) and Pd (1~5 nm)/Ag films before and after annealing is investigated using XRD, as shown in Fig. 5.7. The interplanar spacing of Ag(111) for the as-deposited pure Ag and Pd (1~5 nm)/Ag films is almost the same. However, the sharp decrease of the interplanar spacing of Ag(111) in the Pd/Ag films is observed with increasing the annealing temperature and the thickness of the Pd surface layers. Because Pd has the same face-centered cubic structure as Ag, and the interplanar spacing of Pd(111) (0.225 nm)<sup>133)</sup> is smaller than that of Ag(111) (0.236 nm)<sup>2)</sup>, the decrease of the interplanar spacing of Ag(111) indicates that the Pd surface layers has been largely dissolved into the Ag films.

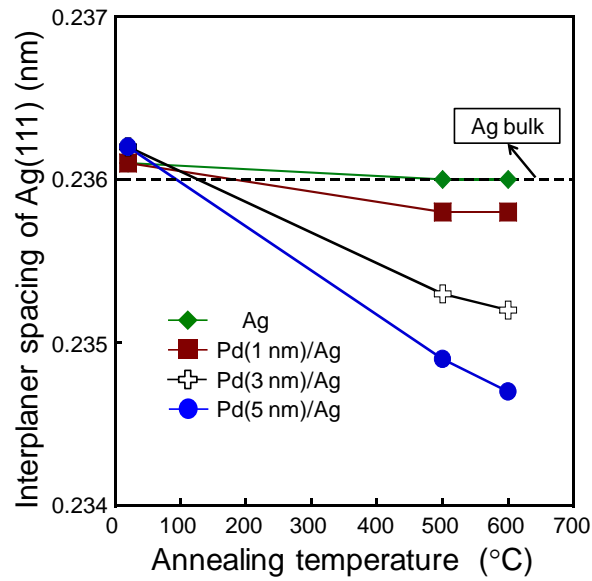


Fig. 5.7 Interplanar spacing of Ag(111) for the Ag (100 nm) and Pd (1~5 nm)/Ag films as a function of annealing temperature.

For binary systems forming a continuous series of solid solutions, the lattice parameter ( $a_{\text{solid solution}}$ ) can be calculated from Vegard's law:<sup>134)</sup>

$$a_{\text{solid solution}} = x_{\text{Pd}}a_{\text{Pd}} + (1 - x_{\text{Pd}}) a_{\text{Ag}} \quad (5.1)$$

where  $x_{\text{Pd}}$  is the mole fraction of Pd,  $a_{\text{Pd}}$  is the lattice parameter of Pd, and  $a_{\text{Ag}}$  is the lattice parameter of Ag, respectively. The concentration of Pd dissolved in Ag after annealing at 500 °C and 600 °C has been calculated from Eq. 5.1. As shown in Table 5.1, after annealing, the concentration of Pd increases significantly with increasing the thickness of the Pd surface layer.

Table 5.1 Concentration (at. %) of Pd dissolved in Ag for the Pd (1~5 nm)/Ag films after annealing at 500 °C and 600 °C.

	Pd concentration (at.%)	
	500 °C	600 °C
Pd (1 nm)/Ag	1.8	1.8
Pd (3 nm)/Ag	6.4	7.3
Pd (5 nm)/Ag	10.0	11.8

The formation of the solid solution induces the large decrease of the amount of Pd at the surface, and further lowers the performance of the Pd surface layers in agglomeration suppression. Meanwhile, it is clear that the change of the resistivity for the Pd/Ag films is in substantial agreement on the change of the Pd concentration in the Ag films after annealing, as compared with Fig. 5.4 and Table 5.1. The effect of solid solution on resistivity seems to be the main factor for the change in the resistivity of the Pd/Ag films as a function of annealing temperature.

## **5.4 Ag film with Pd interface layer (Ag/Pd film)**

### **5.4.1 Surface morphology**

Figure 5.8 shows the SEM images of the Ag/Pd (1~5 nm) films before and after annealing. All of the as-deposited films show very flat surface. After annealing at 500 °C, a lot of small voids and hillocks form, which make the surfaces very rough. The rms roughness of the Ag/Pd (5 nm) film after annealing at 500 °C was 8.2 nm, which is the same as the Pd (5 nm)/Ag film after annealing at 500 °C. After annealing at 600 °C, the development of the agglomeration brings about the growth of the voids and hillocks. In addition, it is difficult to observe any improvement in thermal stability with increasing the thickness of the Pd interface layer. Although the Ag/Pd (1~5 nm) films have not agglomerated as seriously as the pure Ag film after annealing at 600 °C, the effect of the Pd interface layer on agglomeration suppression is much worse than the Ti and Nb interface layers, as compared with Fig. 3.10 and Fig. 4.10.

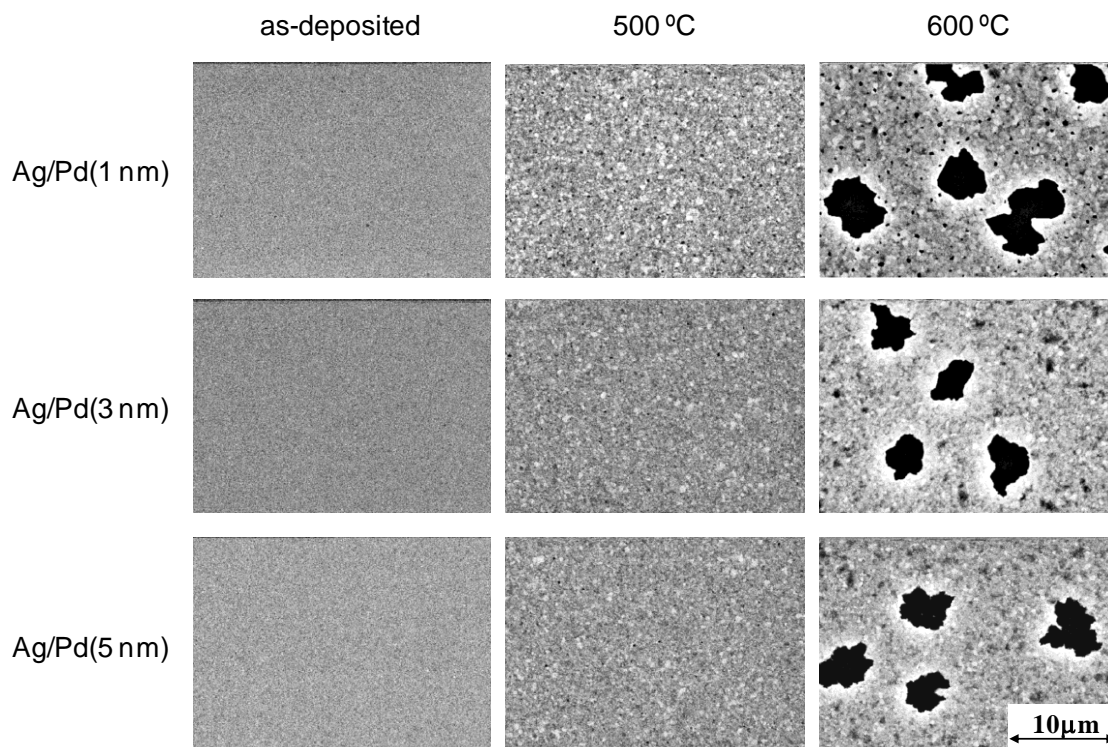


Fig. 5.8 SEM images of the Ag/Pd (1~5 nm) films before and after annealing.

#### 5.4.2 Electrical resistivity

Figure 5.9 shows the electrical resistivity of the pure Ag (100 nm) and Ag/Pd (1~5 nm) films as a function of annealing temperature. The as-deposited Ag/Pd (1~5 nm) films show almost the same resistivity to the as-deposited pure Ag film. After annealing at 500 °C, the resistivity of Ag/Pd (1 nm) film reduces, but is a little higher than that of the pure Ag film. After annealing at 600 °C, the resistivity of all the Ag/Pd (1~5 nm) films continue to increase remarkably. As expected, the resistivity of the Ag/Pd films increases significantly with increasing the thickness of the Pd interface layer and the annealing temperature, and the change in the resistivity of the Ag/Pd films is nearly the same as that of Pd/Ag films. Therefore, it is considered that the poor thermal stability of the Ag/Pd films and the high solid solubility of Pd in Ag have strong influence on the resistivity of the Ag/Pd films.

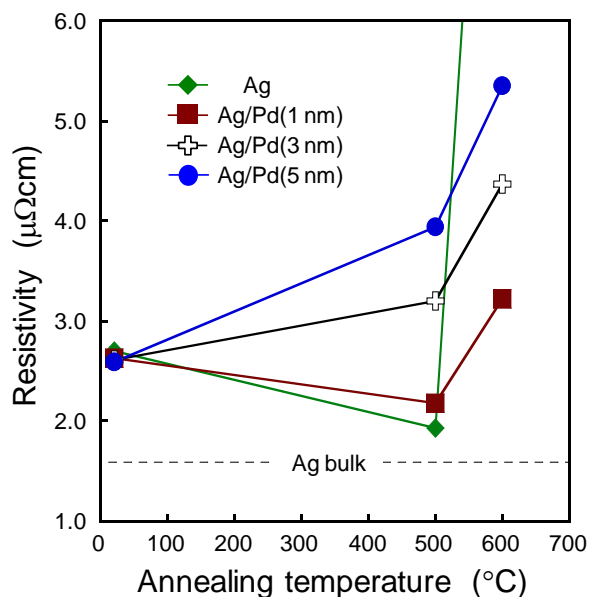


Fig. 5.9 Resistivity of the Ag (100 nm) and Ag/Pd (1~5 nm) films as a function of annealing temperature.

#### 5.4.3 Adhesion strength of Ag/Pd film to SiO<sub>2</sub> substrate

The adhesion strength of the as-deposited pure Ag (100 nm) and Ag/Pd (1~5 nm) films on the SiO<sub>2</sub> substrates was evaluated using micro-scratch test, and the results are shown in Fig 5.10. It is found that the adhesion is not enhanced at all by inserting a Pd interface layer. It is considered to be related to the poor adhesion of Pd on SiO<sub>2</sub>.<sup>135)</sup> It is well known that the interfacial bonding will be weak if the film and substrate materials have such different bonding character (covalent, ionic, or metallic) that they do not easily bond to each other.<sup>136)</sup> As mentioned above, Pd is difficult to be oxidized as well as Ag, owing to their low free energy of formation of oxide. Therefore, unlike the Ti interface layer, the Pd interface layer hardly forms strong covalent bonds to the SiO<sub>2</sub> substrate. The poor adhesion of the Ag/Pd films on the SiO<sub>2</sub> substrates is one of the reasons for their poor thermal stability.

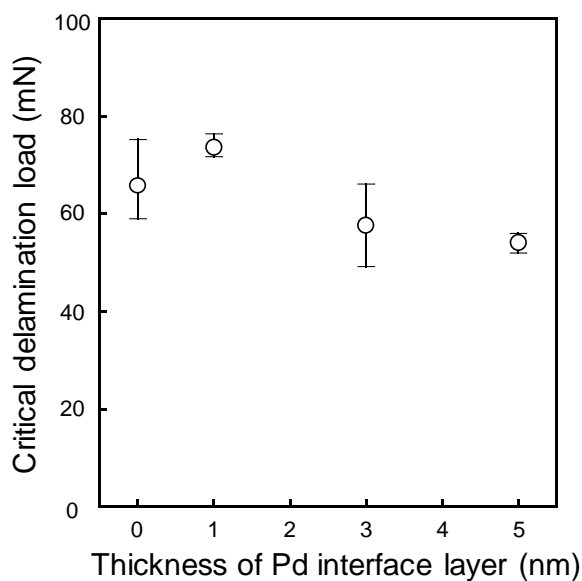


Fig. 5.10 Critical delamination load of the as-deposited Ag (100 nm) and Ag/Pd (1~5 nm) films.

#### 5.4.4 Crystalline orientation of Ag(111) for Ag/Pd film

The crystalline orientation of Ag(111) for the as-deposited Ag/Pd (1~5 nm) films was investigated using XRD rocking curve analysis, as shown in Fig. 5.11. With inserting the Pd interface layers, the peaks of Ag(111) are still not clearly observed in the patterns. It is indicated that the crystalline orientation of Ag(111) is not improved by the Pd interface layers under the deposition conditions of this study, though both Ag and Pd are in fcc structure, and the mismatch of the interplanar spacing of Ag(111) and Pd(111) is 4.9%,<sup>2, 133)</sup> which is not very large.<sup>137)</sup> Consequently, the Pd interface layer scarcely influences the crystalline orientation of Ag(111) of the overlying Ag films, which is not helpful for agglomeration suppression.

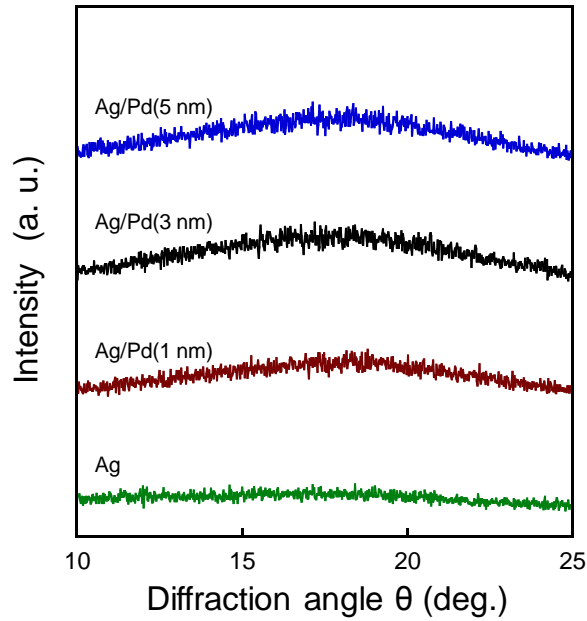


Fig. 5.11 XRD rocking curves of the as-deposited Ag (100 nm) and Ag/Pd (1~5 nm) films.

#### 5.4.5 Solid solubility of Pd in Ag film

Finally, the investigation of the interplanar spacing of Ag(111) for the Ag/Pd (1~5 nm) films before and after annealing was carried out by XRD analysis, as shown in Fig. 5.12. The as-deposited Ag/Pd (1~5 nm) films exhibit almost the same interplanar spacing of Ag(111) as that of the as-deposited pure Ag film. However, the sharp reduction in the interplanar spacing of Ag(111) of the Ag/Pd films is also observed with increasing the thickness of the Pd interface layers and the annealing temperature, and the changing trend is almost the same as that of Pd/Ag films.

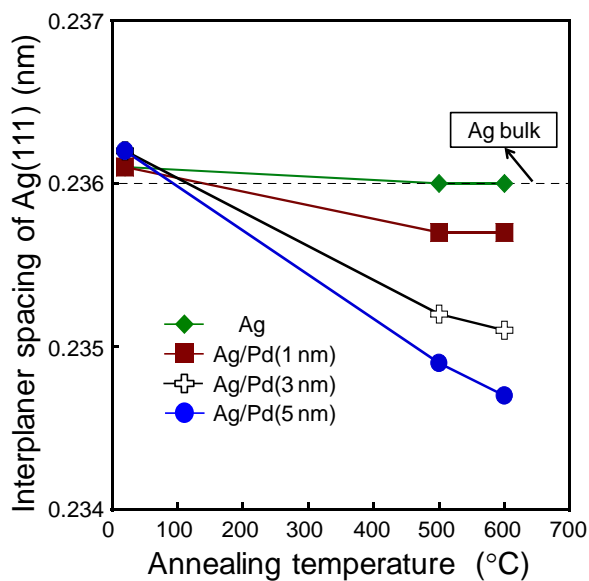


Fig. 5.12 Interplanar spacing of Ag(111) for the Ag (100 nm) and Ag/Pd (1~5 nm) films as a function of annealing temperature.

The concentration of the dissolved Pd in Ag for the Ag/Pd films after annealing at 600 °C has been calculated on the basis of Vegard's law, and the results is listed in Table 5.2. The dissolved Pd atoms make little contribution to agglomeration suppression, and remarkably increase the resistivity because of the impurity scattering effect.

Table 5.2 Concentration (at. %) of Pd dissolved in Ag for the Pd (1~5 nm)/Ag films after annealing at 500 °C and 600 °C.

	Pd concentration (at.%)	
	500 °C	600 °C
Ag/Pd (1 nm)	2.7	2.7
Ag/Pd (3 nm)	7.3	8.1
Ag/Pd (5 nm)	10	11.8

## 5.5 Summary

The poor morphological stability of the Pd film is attributed to its low free energy for the oxide formation and low cohesive energy, which lower the capability of the Pd surface layer to suppress the agglomeration of the Ag film. The ease of the formation of solid solution with Ag decreases the effect of the surface layer on the agglomeration suppression, and remarkably increases the resistivity after high temperature heat treatment. Therefore, Pd is not appropriate for the surface layer of the Ag film.

Both the adhesion of the Ag film to the SiO<sub>2</sub> substrate and the crystalline orientation of Ag(111) are not improved by inserting a Pd interface layer, which lead to no obvious improvement in thermal stability of the Ag films. After annealing, the dissolved Pd atoms in Ag coming from the interface layer make the resistivity increase abruptly. Therefore, Pd is also not suitable for the interface layer of the Ag film.



# Chapter 6 Effects of Ni Surface Layer and Interface Layer on Thermal Stability and Electrical Properties of Ag Thin Film

## 6.1 Introduction

Previously, the usefulness of Ag-Ni alloy films in agglomeration suppression has been reported by our group.<sup>32)</sup> However, the impurity scattering effect causes a significant increase of the resistivity. Therefore, the fabrication of multilayered structure of the Ag film with Ni surface layer or/and interface layer is proposed. Ag-Ni is representative of an insoluble binary alloy system, as shown in Fig. 6.1,<sup>138)</sup> and the resistivity of bulk Ni ( $\rho = 6.84 \mu\Omega \text{ cm}$  at 293 K) is relatively close to that of bulk Ag ( $\rho = 1.59 \mu\Omega \text{ cm}$  at 293 K),<sup>3)</sup> which is advantageous for Ni as the surface layer of the Ag film. However, it is worth noting that, unlike Ti and Nb, Ni with very low free energy of formation of NiO ( $\Delta_f G^\circ = -211.7 \text{ kJ/mol}$ )<sup>68)</sup> is difficult to form oxide passivation surface layer. Although Nb surface layer in metallic state has been confirmed to effectively suppress the agglomeration of the Ag film, and the cohesive energy of Ni (428 kJ/mol) is higher than that of Ag (248 kJ/mol),<sup>119)</sup> it is questionable whether the Ni metallic surface layer could effectively suppress the agglomeration of the Ag film as well as the Nb metallic surface layer.

On the other hand, both Ni and Ag crystals belong to fcc structure,<sup>139)</sup> and the bulk interplanar spacing of Ni(111) and Ag(111) is 0.2034 and 0.2359 nm, respectively.<sup>2, 140)</sup> Although the mismatch of the interplanar spacing between Ag(111) and Ni(111) is approximately 18%, the possibility for the epitaxial growth of Ag(111) on the interface layer of Ni(111) has been confirmed by some research groups.<sup>141-144)</sup> Therefore, the enhancement of the orientation of Ag(111) owing to the Ni interface layer has been ever expected in this study, which would improve the thermal stability and lower the resistivity.

To reveal the effects of the Ni surface layer and interface layer on the thermal stability and the electrical resistivity of the Ag film, the Ni/Ag and Ag/Ni films were prepared for investigation in this chapter.

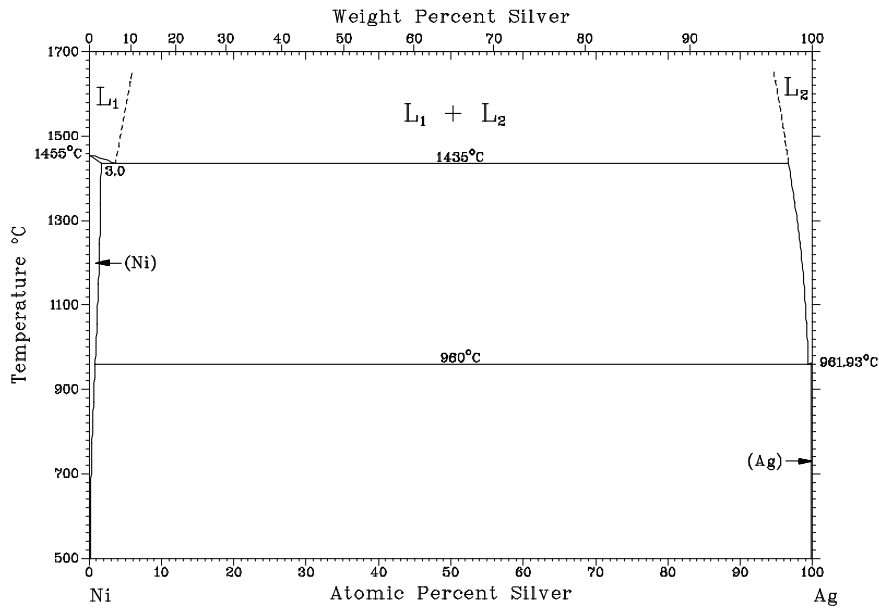


Fig. 6.1 Ag-Ni binary phase diagram. <sup>138)</sup>

## 6.2 Experimental procedure

The Ni (60 nm), Ni (1~5 nm)/Ag and Ag/Ni (1~5 nm) films were deposited using RF magnetron sputtering. Because the magnetic Ni was more difficult to form plasma than ordinary metal in magnetron sputtering, <sup>145)</sup> the sputtering power and Ar gas pressure were raised to 100 W and  $2.8 \times 10^{-2}$  Torr, respectively, and the distance between the Ni target and substrate was shortened to 40 mm. Then, annealing was carried out under vacuum. Finally, various evaluations were carried out as before. The structure of these double-layer films deposited in this study is shown in Fig. 6.2.

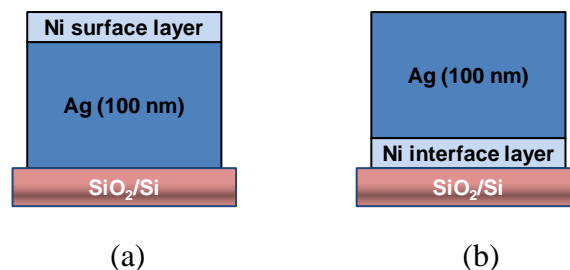


Fig. 6.2 Structure of the multilayered films deposited using RF magnetron sputtering. (a) Ni/Ag film, and (b) Ag/Ni film.

## 6.3 Ag film with Ni surface layer (Ni/Ag film)

### 6.3.1 Surface morphology

Figure 6.3 shows the SEM image of the Ni (1~10 nm)/Ag films before and after annealing. The surfaces of all the films are as smooth as the surfaces of the Ag films with other surface layers showed in previous chapters. However, after annealing at 500 °C, all the Ni (1~10 nm)/Ag films show almost the same rough surfaces owing to the formation of many small voids and hillocks after annealing at 500 °C.

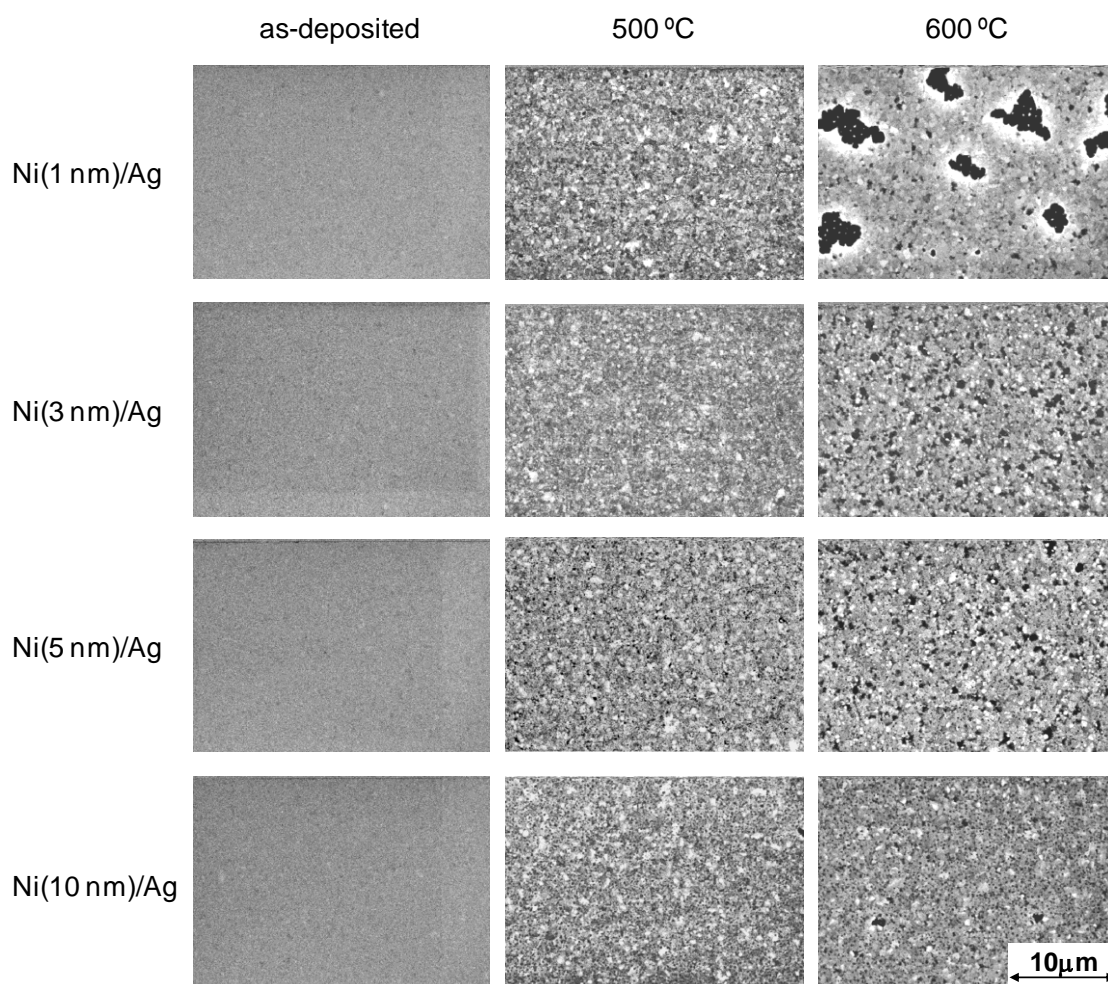


Fig. 6.3 SEM images of the Ni (1~10 nm)/Ag films before and after annealing.

With increasing the annealing temperature to 600 °C, the Ni (1~10 nm)/Ag films show further growth of the voids and hillocks. Specifically, the diameter of the voids at

the surface of the Ni (1 nm)/Ag film varies from about 3 nm to 7 nm, which are much larger than the voids in other Ni/Ag films. It is considered that the 1-nm-thick Ni surface layer is too thin to form continuous protective layer for agglomeration suppression. When the thickness of the Ni surface layers is increased to 3 nm and above, the surface morphology becomes better judging from the smaller voids. However, even with a 10-nm-thick Ni surface layer, there are still a large amount of small voids and hillocks occurred.

The rms surface roughness of the Ni (5 nm)/Ag films after annealing at 500 °C and 600 °C were measured using AFM, which were 4.5 nm and 13.3 nm, respectively. The rough surfaces of the annealed Ni (5 nm)/Ag films further indicate the poor effect of the Ni surface layer on agglomeration suppression.

Because the Ni (1~10 nm)/Ag films have not agglomerated as severely as the pure Ag film, the agglomeration of the Ag films is considered to be suppressed to some extent owing to the Ni surface layers. However, as compared with the effects of the Ti and Nb surface layers, as shown in Fig. 3.2 and Fig. 4.2, the thermal stability of the Ag films is not effectively improved using the Ni surface layers.

### **6.3.2 Electrical resistivity**

Figure 6.4 shows the change in the resistivity of the Ag (100 nm) and Ni (1~10 nm)/Ag films as a function of annealing temperature. It is found that the resistivity of the as-deposited Ni (1~10 nm)/Ag films is almost the same, and close to that of the as-deposited Ag film. It is considered that the Ni surface layer has little influence on the resistivity of the as-deposited Ag film due to its low bulk resistivity. The resistivity of the Ni (1~10 nm)/Ag films decreases to approximately 2.1  $\mu\Omega$  cm after annealing at 500 °C, owing to the improvement in the crystallinity of the Ag films, no occurrence of serious agglomeration, and difficulty in the formation of solid solution. After annealing at 600 °C, the resistivity of the Ni (1 nm)/Ag film rises to 3.0  $\mu\Omega$  cm, caused by its poorer morphological stability than other Ni/Ag films, as shown in Fig. 6.3. Because of some improvement in the morphological stability with increasing the thickness of the Ni surface layers, the resistivity of the Ni (3~10 nm)/Ag films rises to only approximately 2.3  $\mu\Omega$  cm. However, as discussed in the previous chapters, the Ti (3~10 nm)/Ag and

Nb (3~10 nm)/Ag films can obtain the lower resistivity after annealing at 500 °C and 600 °C, which suggests that the Ni surface layer is less effective on the maintenance of the low resistivity after annealing.

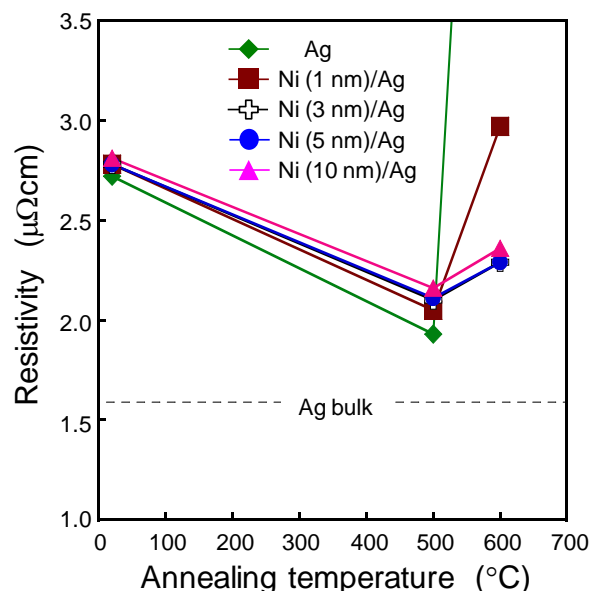


Fig. 6.4 Resistivity of the Ag (100 nm) and Ni (1~10 nm)/Ag films as a function of annealing temperature.

### 6.3.3 Chemical bonding state of the surface

The chemical bonding state for the surface of the Ni (5 nm)/Ag films before and after annealing at 500 °C was investigated by using XPS, and the XPS spectra are shown in Fig. 6.5. The spectra show that the main peaks of Ni 2P<sub>3/2</sub> and Ni 2P<sub>1/2</sub> for both the as-deposited Ni (5 nm)/Ag film and the annealed Ni (5 nm)/Ag film are the same, and the binding energies are 852.6 eV and 869.8 eV, respectively, which are the same as the reference values for the Ni in metallic state.<sup>132)</sup> The as-deposited Ni (5 nm)/Ag film exhibits two small peaks, and the binding energies for them are 856.0 eV and 861.1 eV, which belong to Ni<sub>2</sub>O<sub>3</sub> and NiO, respectively, according to the reference values.<sup>115, 132)</sup> As compared to the peak intensity for Ti oxide and Nb oxide in the XPS spectra for the as-deposited Ti (3 nm)/Ag film and Nb (3 nm)/Ag film, the peak intensity for the Ni oxide is very weak, so it could be said that the Ni surface layer is difficult to be oxidized.

Then, it is found that these small peaks for Ni oxide disappeared after annealing. It has been reported that the oxides  $\text{Ni}_3\text{O}_4$ ,  $\text{Ni}_2\text{O}_3$  and  $\text{NiO}$  exist only at high oxygen pressure.<sup>146)</sup> F. Maglia *et al.* have confirmed that the decomposition of 30~40-mg-weighty  $\text{NiO}$  single crystal can be achieved in a vacuum at temperatures as low as 330 °C without using reducing agent, and at temperature below 500 °C the decomposition proceeds immediately.<sup>147)</sup> Therefore, it is considered that the small amount of Ni oxide in the surface layer has completely decomposed during vacuum heat treatment in this study. The above results indicates that the Ni (5 nm)/Ag film has mainly remained in metallic state during annealing.

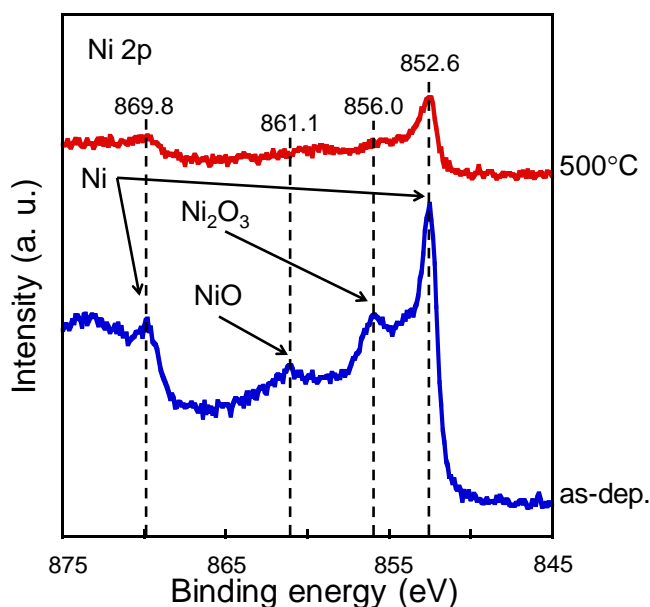


Fig. 6.5 Ni 2p XPS spectra for the surfaces of the Ni (5 nm)/Ag films before and after annealing at 500 °C.

On the other hand, figure 6.5 shows that the peak intensity for metal Ni reduces after annealing, which is representative of a reduction in the amount of Ni at the surface. It is well known that it is difficult for Ni and Ag to form solid solution, which is also proved in section 6.3.5. In addition, Fig. 6.4 shows that there is no impurity scattering effect on the resistivity of the Ni (1~10 nm)/Ag films after annealing at 500 °C. it means Ni atoms have not entered deep into the Ag layer. Therefore, it is considered that the interdiffusion of Ni and Ag atoms only occurred in a small region around the interface

between the Ni surface layer and the Ag film. Then, the concentration of Ni at the surface was decreased, which leads to the reduction of the peak intensity for metal Ni.

As a result of the above analysis, the Ni surface layer mainly remains in the metallic state during annealing, and Ni oxide at the surface of the Ag films would have little effect on agglomeration suppression, owing to the ease of thermal decomposition for Ni oxide in a vacuum, so metal Ni is responsible for the change in the thermal stability of the Ag films. In addition, it is considered that the interdiffusion between the metal Ni and Ag occurs in a very small region during annealing. The diffusion decreases the amount of Ni at the surface layer, which would weaken the role of the Ni surface layer in suppressing the agglomeration of Ag.

#### 6.3.4 Cohesive energy and morphological stability of Ni

In this section, a reason for the inapplicability of the metallic Ni surface layer for agglomeration suppression is studied from the relationship between cohesive energy and morphological stability of Ni.

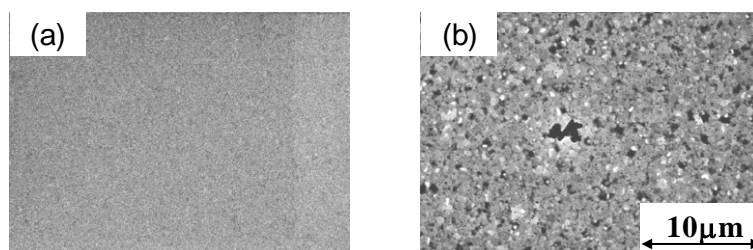


Fig. 6.6 SEM images of the as-deposited Ni (60 nm) film (a) and the one after annealing at 600 °C (b).

Figure 6.6 shows the SEM image of the Ni (60 nm) film before and after annealing at 600 °C. The as-deposited Ni film is very smooth. After annealing at 600 °C, it displays scraggly surface with many small voids and hillocks, although it is not agglomerated as severely as the pure Ag film. The low cohesive energy of 428 kJ/mol is confirmed not to be high enough for metal to avert the agglomeration completely at the annealing temperature of 600 °C, though the higher cohesive energy of Ni (428 kJ/mol) than that

of Ag (248 kJ/mol) leads to the better morphological stability of Ni. It is indicated that the low cohesive energy of Ni leads to the easy migration of Ni atoms at high temperature and a poor morphological stability, which is disadvantageous for agglomeration suppression.

### 6.3.5 Crystal structure

Figure 6.7 shows XRD patterns of the as-deposited Ag (100 nm) and Ni (1~10 nm)/Ag films. The Ni (1~10 nm)/Ag films show almost the same crystal structure as the Ag film, which are consist of the main peak of Ag(111) and the sub-peak of Ag(200). The intensity, FWHM, and position of the Ag(111) peaks basically remain unchanged with increasing the thickness of the Ni surface layers. Therefore, the deposition of Ni surface layer has no influence on the crystal structure of the underlying Ag films.

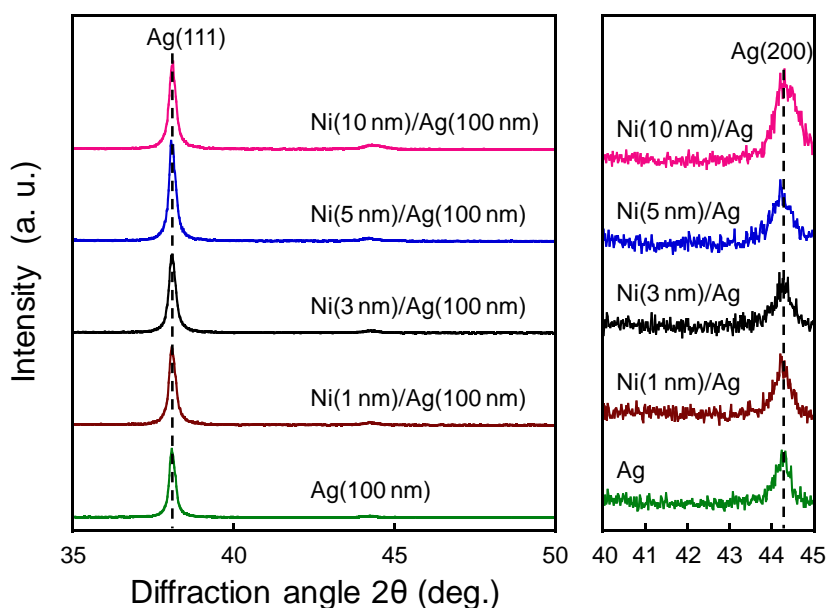


Fig. 6.7 XRD patterns of the as-deposited Ag (100 nm) and Ni (1~10 nm)/Ag films.

In order to confirm that no solid solution formed in the Ni/Ag films, the interplanar spacing of Ag(111) in the Ag (100 nm) and Ni (1~10 nm)/Ag films as a function of annealing temperature was investigated, as shown in Fig. 6.8. It is found that the interplanar spacing of Ag(111) for all the Ag and the Ni (1~10 nm)/Ag films shows almost the same value before and after annealing, and thus the different marks almost

coincide with each other. The result accounts for the inexistence of Ag-Ni solid solution in the Ni/Ag films, and it is consistent with the expectation in the previous sections.

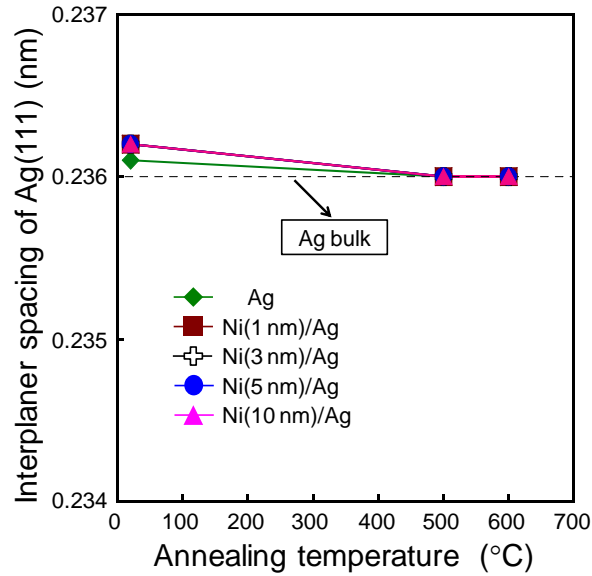


Fig. 6.8 Interplanar spacing of Ag(111) for the Ag (100 nm) and Ni (1~10 nm)/Ag films as a function of annealing temperature.

## 6.4 Ag film with Ni interface layer (Ag/Ni film)

### 6.4.1 Surface morphology

In order to evaluate the effects of the Ni interface layers on the thermal stability of the overlying Ag films, the change in the surface morphology of the Ag/Ni (1~10 nm) films was investigated using SEM analysis, and the images are shown in Fig. 6.9. As expected, the as-deposited Ag/Ni (1~10 nm) films show very smooth surface. After annealing at 500 °C, the surfaces of all the Ag/Ni (1~10 nm) films become rougher with the existence of a large amount of small voids and hillocks. It seems that there is no significant difference in the surface morphology of the Ag/Ni films after annealing at 500 °C with increasing the thickness of the Ni interface layer. After annealing at 600 °C, many voids in the Ag/Ni (1 nm) film become larger with their diameter increasing to 3~5 nm caused by further agglomeration. With increasing the thickness of the Ni interface layer to 3 nm and above, there is no obvious change in the surface morphology,

except that the voids become a little smaller.

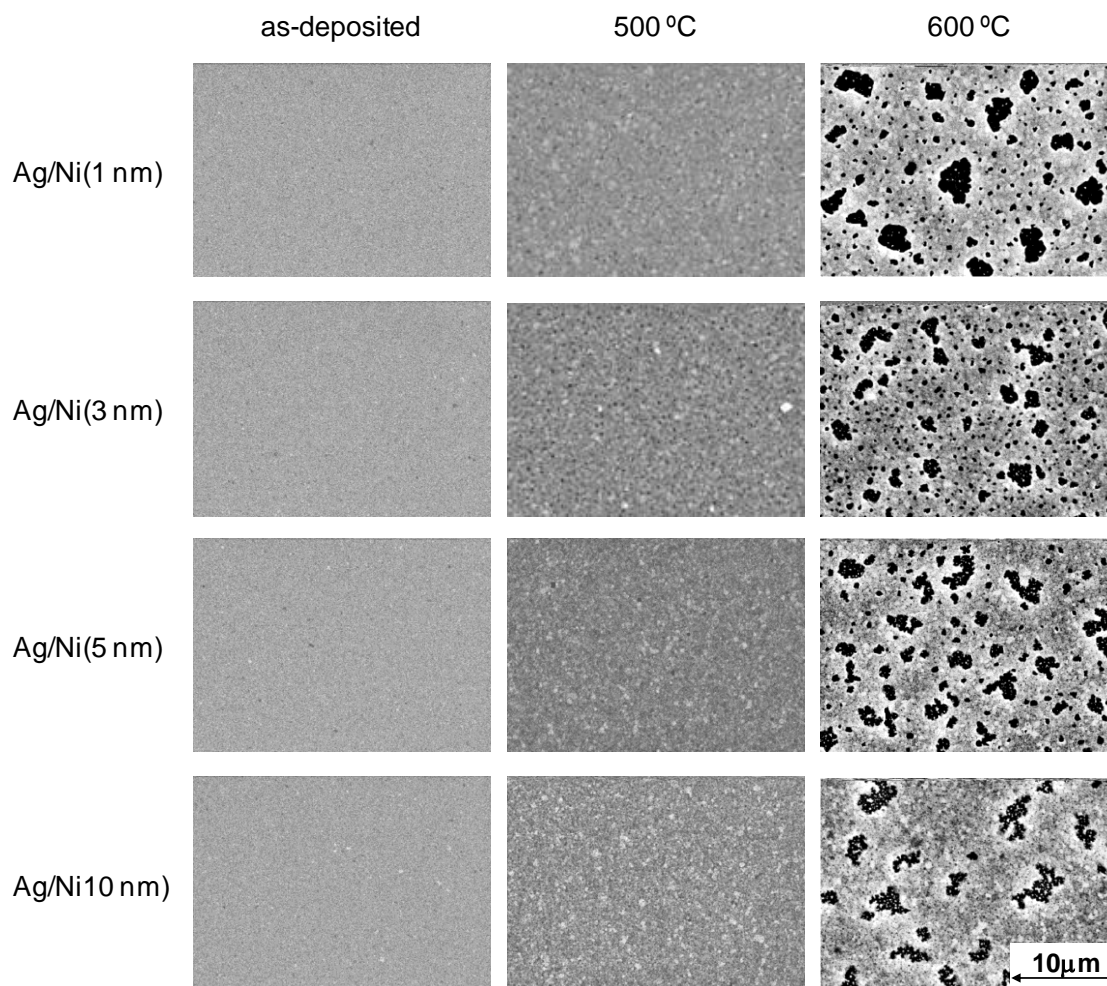


Fig. 6.9 SEM images of the Ag/Ni (1~10 nm) films before and after annealing.

As compared with the severely agglomerated Ag film after annealing at 600 °C, some improvement in the thermal stability of the Ag films owing to the Ni interface layer could be recognized. However, in comparison with the effect of the Ti and Nb interface layers, as shown in Fig. 3.10 and Fig. 4.10, the Ni interface layer has less effect on the agglomeration suppression. The causes are analyzed in later sections.

#### 6.4.2 Electrical resistivity

Figure 6.10 shows the change in the resistivity of the Ag (100 nm) and Ag/Ni (1~10

nm) films as a function of annealing temperature. The resistivity of the as-deposited Ag/Ni (1~10 nm) films shows almost the same value to that of the as-deposited Ag film. It is apparent that, unlike the Ti and Nb interface layers, the introduction of the Ni interface layers has no influence on the resistivity of the Ag films. After annealing at 500 °C, the resistivity of all the films decreases to about 2.0  $\mu\Omega$  cm. This is because the crystallinity of the Ag films has been improved, and the small voids caused by agglomeration have not made the films discontinuous.

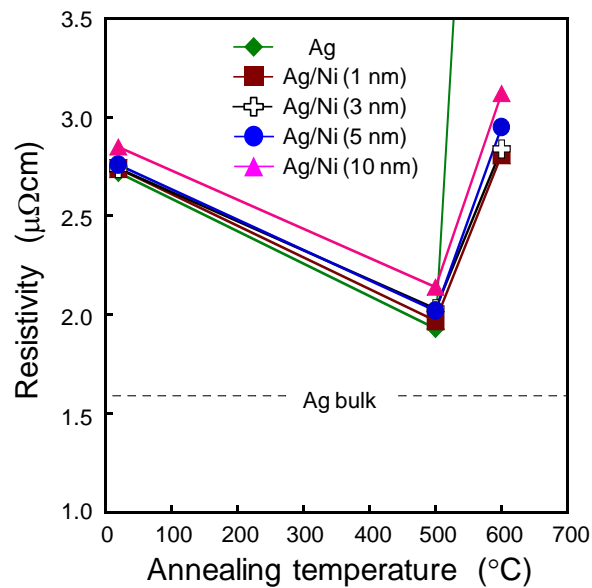


Fig. 6.10 Resistivity of the Ag (100 nm) and Ag/Ni (1~10 nm) films as a function of annealing temperature.

However, after annealing at 600 °C, the resistivity of all the Ag/Ni (1~10 nm) films increases to approximately 3.0  $\mu\Omega$  cm, owing to their common poor morphological stability with many large voids occurrence. However, the resistivity of the Ag/Ni (1~10 nm) films after annealing at 600 °C does not reach to the high value of the annealed pure Ag film, caused by a certain degree of improvement in agglomeration suppression by inserting the Ni interface layers, as mentioned in the above section.

### 6.4.3 Adhesion strength of Ag/Ni film to SiO<sub>2</sub> substrate

Figure 6.11 shows the change in the critical delamination load for the as-deposited Ag/Ni (1~10 nm) films deposited on SiO<sub>2</sub> substrates as a function of the thickness of the Ni interface layers. The results show that the adhesion strength becomes four times stronger than that of the pure Ag film with inserting a 1-nm-thick Ni interface layer, and the adhesion strength continues to increase to about six times stronger than that of the pure Ag film with increasing the thickness of the Ni interface layers to 3 nm and above. The great improvement in the adhesion contributes to the agglomeration suppression, so the Ag/Ni films have not agglomerated as severely as the pure Ag film after annealing.

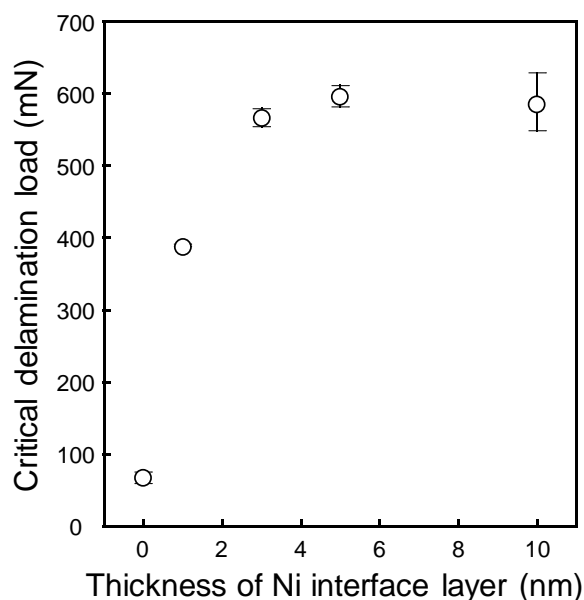


Fig. 6.11 Critical delamination load of the as-deposited Ag (100 nm) and Ag/Ni (1~10 nm) films.

It has been reported previously that the Ni interface layer has good effect on the improvement in the adhesion of the metal film and SiO<sub>2</sub> substrate.<sup>148)</sup> Although Ni with low Gibbs free energy for oxide formation is difficult to be oxidized, the Gibbs free energy for NiO formation is less than zero, which ensures the possibility of NiO formation. The sputtered Ni atoms are given enormous energy by RF magnetron sputtering.<sup>149)</sup> It is likely that, in the moment of the collision of the sputtered Ni atoms

with the SiO<sub>2</sub> substrate, the bond between Ni and O is formed. Moreover, the power for sputtering Ni was increased to 100 W, and it is much larger than the sputtering power for Ti and Nb, hence the degree of the reaction between Ni and SiO<sub>2</sub> is higher, which leads to the larger adhesion strength for the Ag/Ni (3~10 nm) films on SiO<sub>2</sub> substrates than that for the Ag/Ti and Ag/Nb films.

#### 6.4.4 Crystal structure

Figure 6.12 shows XRD patterns of the as-deposited Ni (60 nm), Ag (100 nm) and Ag/Ni (1~10 nm) films. The as-deposited pure Ni film mainly show the orientation of Ni(111). However, the Ag/Ni films do not show the single orientation of Ag(111), and the position and intensity of the peaks for Ag(111) and Ag(200) does not change with increasing the thickness of the Ni interface layers. It is indicated that the Ni interface layers have no influence on the crystal structure of the overlying Ag films in this study.

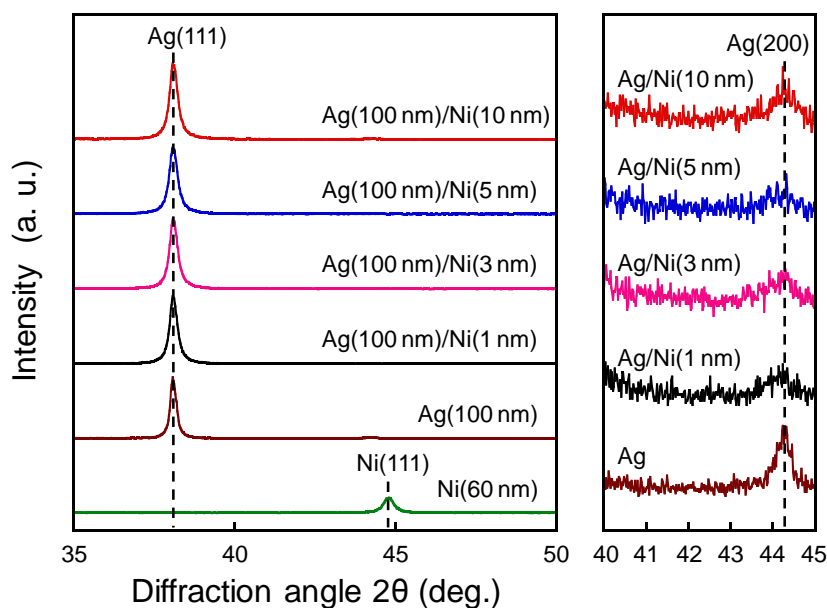


Fig. 6.12 XRD patterns of the as-deposited Ni (60 nm), Ag (100 nm), and Ag/Ni (1~10 nm) films.

The crystalline orientation of Ag(111) in the as-deposited Ag and Ag/Ni films was further evaluated by XRD rocking curve test, as shown in Fig. 6.13. Because there is no

sharp peak for Ag(111) in any curve, the crystalline orientation of Ag(111) has not been improved by the Ni interface layers. It has been reported that the epitaxial growth is very dependent on substrate temperature, degree of vacuum, and especially lattice mismatch.<sup>137)</sup> Since the lattice constant of Ag is 18% over that of Ni, a very strict deposition condition is required. Therefore, under the experimental condition of this study, it is impossible for the Ni interface layers to enhance the crystalline orientation of Ag(111). Owing to the combined effects of the enhancement in the adhesion strength and crystalline orientation of Ag(111), the Ag/Ti films have shown much higher thermal stability than the Ag/Ni films.

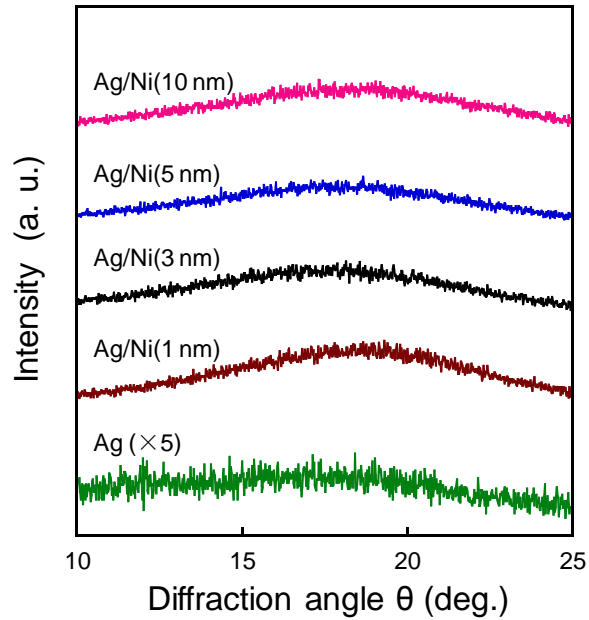


Fig. 6.13 XRD rocking curves of the as-deposited Ag (100 nm) and Ag/Ni (1~10 nm) films.

In order to make sure whether solid solution formed in the Ag/Ni (1~10 nm) films, the interplanar spacing of Ag(111) in the Ag/Ni films as a function of annealing temperature was investigated, as shown in Fig. 6.14. It is found that the interplanar spacing of Ag(111) for the Ag/Ni (1~10 nm) films scarcely changes with increasing the annealing temperature as well as the pure Ag film. Therefore, as expected, the Ni interface layers have not formed a solid solution with the Ag films. Consequently, it is difficult for Ni atoms in the interface layer to dissolve in the Ag film to disturb the

growth of Ag grains and to increase the resistivity of the Ag film.

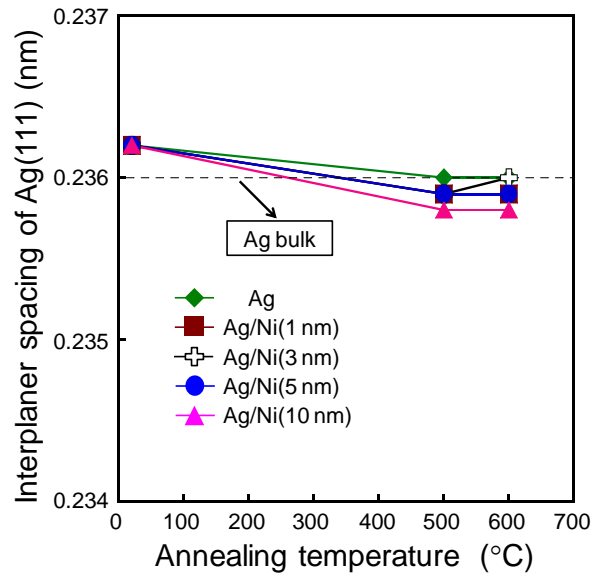


Fig. 6.14 Interplanar spacing of Ag(111) for the Ag (100 nm) and Ag/Ni (1~10 nm) films as a function of annealing temperature.

## 6.6 Summary

The Ni surface layer remains in metallic state during annealing caused by the low free energy for Ni oxide formation. However, the morphological stability of metal Ni is poor owing to its low cohesive energy, which is disadvantageous for suppressing the agglomeration of the Ag films. Therefore, the effect of the Ni surface layer is less than those of the Ti and Nb surface layers.

The Ni interface layers can improve the adhesion of the Ag films to the SiO<sub>2</sub> substrates, which contributes to the improvement in the thermal stability of the Ag films. However, the Ni interface layers can not induce an epitaxial growth of Ag(111) in this study. Therefore, the effect of the Ni interface layers on the improvement in the thermal stability of the Ag films is inferior to the Ti interface layers. Caused by the relatively poor thermal stability of the Ag/Ni films, the resistivity of the Ag/Ni films rises to 3.0  $\mu\Omega$  cm after annealing at 600 °C.

# **Chapter 7 Appropriate Surface Layer and Interface Layer for Structure-Modification of Ag Thin Film**

## **7.1 Introduction**

On the basis of the results of the previous chapters, it is possible to make clear what categories of the metal are appropriate for the surface and interface layers of the Ag films to improve the morphological stability of the Ag thin films as well as maintain their low resistivity. The properties and the effects of various surface and interface layers have been made a comparison, and then the essential properties for the metal materials suited as surface layer or interface layer of the Ag thin film are summarized in this chapter.

## **7.2 Appropriate surface layers**

### **7.2.1 Comparison of surface layers**

The primary role of the surface layer is to inhibit the surface diffusion of the Ag films during annealing, which contributes to the agglomeration suppression. Therefore, good morphological stability is essential for the surface layers. We compare the morphological stability of the pure metal films with the thickness of about 60 nm, which have been described in the previous chapters. Figure 7.1 shows the SEM images and the rms surface roughness of the 60-nm-thick Ag, Pd, Ni, Ti, and Nb films after annealing at 600 °C in a vacuum. The agglomerating level of the Ag film is the highest among all the films. Although the Pd and Ni films did not agglomerate as severely as the Ag film, the Pd and Ni films with the similarly irregular and rough surface show poor morphological stability. However, the Ti and Nb films show very smooth surface morphology after annealing.

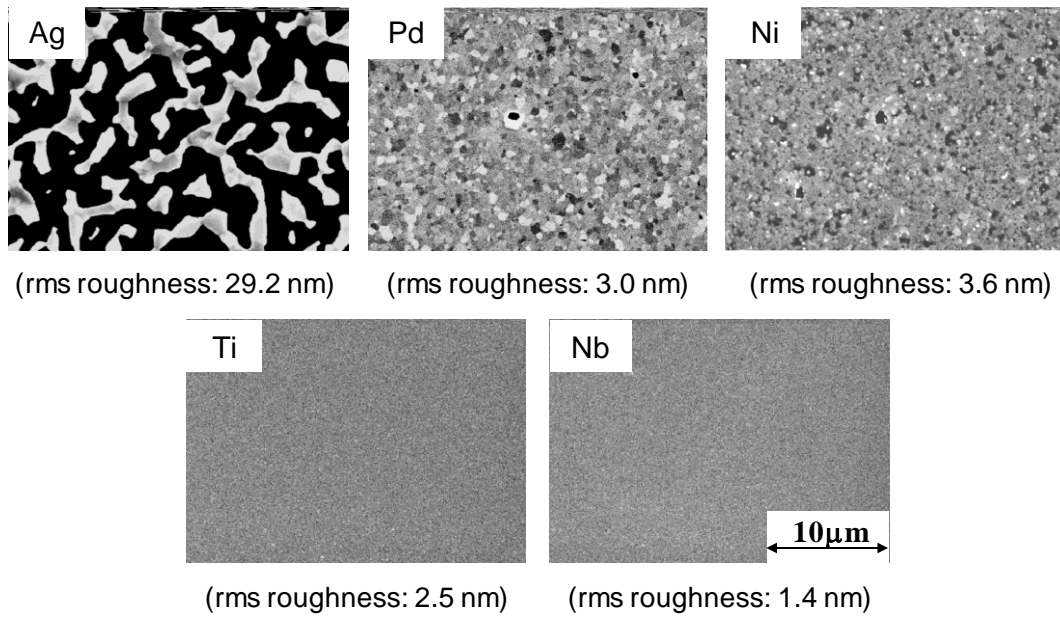


Fig. 7.1 SEM images and rms roughness of the 60-nm-thick Ag, Pd, Ni, Ti, and Nb films after annealing at 600 °C.

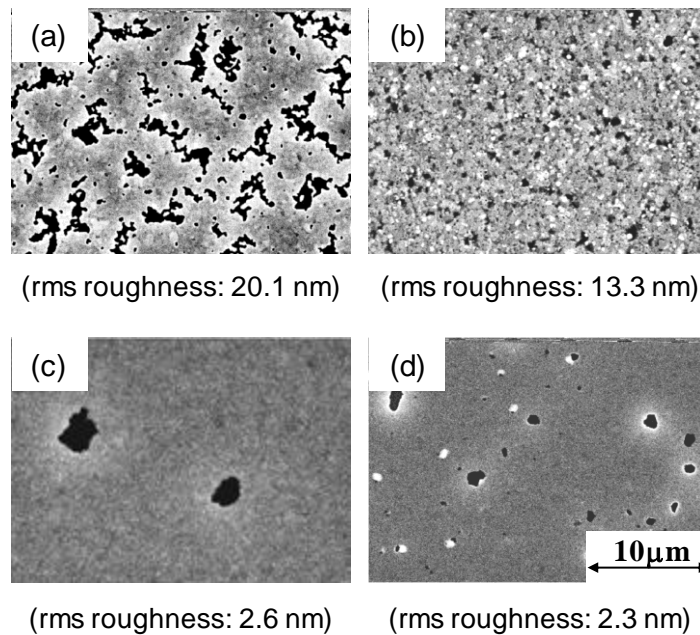


Fig. 7.2 SEM images and rms roughness of Ag (100 nm) films with various surface layers (5 nm) after annealing at 600 °C. (a) Pd, (b) Ni, (c) Ti, and (d) Nb.

Next, the effects of different surface layers on the thermal stability of Ag thin films

are compared. Figure 7.2 shows the SEM images and the rms surface roughness of the Pd (5 nm)/Ag, Ni (5 nm)/Ag, Ti (5 nm)/Ag, and Nb (5 nm)/Ag films after annealing at 600 °C. It is clear that the morphologically stable Ti and Nb are appropriate for the surface layers of the Ag films because of the effective suppression of the Ag agglomeration. On the contrary, the Pd and Ni surface layers are found to be less effective in agglomeration suppression.

The reasons for the above results are discussed according to the analysis of the properties of different metals. The important properties of metals which were used as surface layers of the Ag films are listed in Table 7.1.<sup>3, 68, 119, 150</sup> These properties are considered to be closely related to the improvement of thermal stability and the maintenance of low resistivity of the Ag film according to the analysis in the previous chapters.

Table 7.1 Properties of Ag, Pd, Ni, Ti, and Nb.

	Ag	Pd	Ni	Ti	Nb
Cohesive energy (kJ/mol)	248	376	428	468	730
Gibbs free energy of formation of oxide (kJ/mol)	-5.6 (AgO <sub>0.5</sub> )	-55.4 (PdO)	-211.7 (NiO)	-884.5 (TiO <sub>2</sub> )	-883.1 (NbO <sub>2.5</sub> )
Maximum solid solubility in Ag (at.%)		100	0.3	5	0
Bulk resistivity at 293 K (μΩ cm)	1.59	10.8	6.84	42.0	12.5

Firstly, it is easy to understand that the formation of solid solution with Ag would reduce the thickness of the surface layer, and then weaken the effect of the surface layer on agglomeration suppression. Because Pd can form complete solid solution with Ag, the Pd surface layer can not adequately suppress the agglomeration of the Ag film. Next, as compared with Fig. 7.2 and Table 7.1, it is discovered that the metal with low Gibbs free energy for oxide formation and low cohesive energy shows poor morphological stability, which is disadvantageous for agglomeration suppression. It has been confirmed that the metal thin films with low Gibbs free energy for oxide formation, such as the Pd and Ni, is difficult to be oxidized by natural oxidation, and remains in the

metallic state during vacuum heat treatment. Therefore, there are no thermally stable passivation layers formed to protect their surfaces. In addition, the low cohesive energy results in the ease of the migration of atoms at high temperature, which promotes the agglomeration. Therefore, those metal films with low Gibbs free energy for oxide formation and low cohesive energy are not stable at high temperature, and they are not suitable for the surface layers to protect the Ag film from agglomeration. According to the references (68) and (119), it is interesting that those metals with low Gibbs free energy for oxide formation generally do not present high cohesive energy.

As shown in Table 7.1, the cohesive energy of Ti is not very high, however, the Ti nano-surface layer has been proved to be very easy to form the thermally stable oxide passivation layer even before annealing, owing to its large free energy for oxide formation. The passivation layer contributes to maintain the good surface morphology of the Ag film at high temperature. Therefore, just like Al,<sup>(69)</sup> Ti with large free energy for oxide formation is also appropriate for the surface layer of the Ag film. It is worth noting that the Nb surface layer in either metallic state or oxide state can effectively suppress the agglomeration of the Ag film, which has been confirmed in Chapter 4. Table 7.1 shows that Nb has both large free energy for oxide formation and high cohesive energy. It is suggested that the Nb surface layer, regardless of the chemical state of metal or oxide, can keep stable at high temperature, which is beneficial to agglomeration suppression. In conclusion, the metals with large Gibbs free energy for oxide formation or high cohesive energy are suitable for the surface layers of the Ag films.

Low resistivity is another important feature for the modified Ag films with surface layers. The effects of different surface layers on the resistivity of Ag thin films are compared. Figure 7.3 shows the resistivity of the Pd (5 nm)/Ag, Ni (5 nm)/Ag, Ti (5 nm)/Ag, and Nb (5 nm)/Ag films as a function of annealing temperature. The resistivity of the as-deposited Pd/Ag, Ni/Ag, and Nb/Ag films is very close to that of the as-deposited Ag film. As conjunction with Table 7.1, it is apparent that the surface layers with low bulk resistivity have little influence on the resistivity of as-deposited films. The resistivity of the Pd/Ag film increases remarkably with increasing the annealing temperature caused by the impurity scattering effect owing to the dissolved

Pd atoms. After annealing at 600 °C, the Ti/Ag and Nb/Ag films keep the same level of low resistivity of the films after annealing at 500 °C. On the contrary, the Pd/Ag and Ni/Ag films show high resistivity. It is clear that, after annealing, the maintenance of the low resistivity is attributed to the improvement in the thermal stability of the Ag films with the appropriate surface layers.

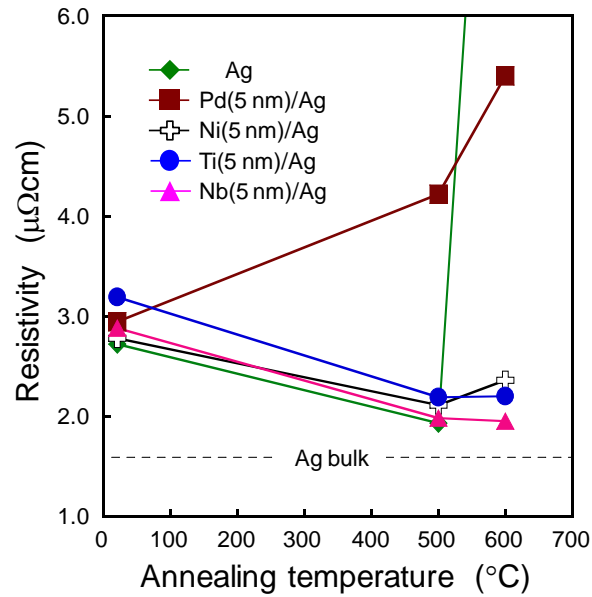


Fig. 7.3 Resistivity of the Ag (100 nm), Pd (5 nm)/Ag (100 nm), Ni (5 nm)/Ag (100 nm), Ti (5 nm)/Ag (100 nm), and Nb (5 nm)/Ag (100 nm) films as a function of annealing temperature.

### 7.2.2 Prediction of appropriate surface layer

The properties mentioned in Table 7.1 are considered to be useful to predict the suitable metal surface layers for the Ag films. As a result of the analysis in the above section, the surface layer with large free energy for oxide formation or high cohesive energy, and low solid solubility in Ag could effectively prevent the underlying Ag film from agglomeration and keep the low resistivity during annealing. Based on the investigation of these properties for all the metals throughout periodic table of elements, the metals which have been encircled in the periodic table, as shown in Fig. 7.4, are supposed to be capable of acting as good surface layers for the improvement in the

thermal stability of the underlying Ag films. In addition, among these candidates, the ones with low bulk resistivity have an advantage on reducing the influence on the low sheet resistance of the Ag film.

Li 158 LiO <sub>0.5</sub> -281 60	Be 320 BeO -580 0.3	← Maximum solid solubility with Ag (at.%) →										B 561 BO <sub>x</sub> > 0 0
Na 107 NaO <sub>0.5</sub> -188 1	Mg 145 MgO -569 29.3	← Cohesive energy (kJ/mol) →										Al 327 AlO <sub>1.5</sub> -791 20.4
		← Gibbs free energy of oxide of formation (kJ/mol) →										
K 90.1 KO <sub>0.5</sub> -160 0	Ca 178 CaO -604 0	Sc 376 ScO <sub>1.5</sub> -910 10.4	Ti 468 TiO <sub>2</sub> -885 4.7	V 512 VO <sub>2.5</sub> -570 0	Cr 395 CrO <sub>1.5</sub> -529 0	Mn 282 MnO <sub>2</sub> -465 43.6	Fe 413 FeO <sub>1.5</sub> -371 0	Co 424 CoO -214 0.8	Ni 428 NiO -212 0.3	Cu 336 CuO -130 14.0	Zn 130 ZnO -318 40.2	Ga 271 GaO <sub>1.5</sub> -499 19
Rb 82.2 RbO <sub>0.5</sub> -150 0	Sr 166 SrO -560 0	Y 422 YO <sub>1.5</sub> -908 1.3	Zr 603 ZrO <sub>2</sub> -1043 0.1	Nb 730 NbO <sub>2.5</sub> -883 0	Mo 658 MoO <sub>3</sub> -668 0.15	Tc 661 TcO <sub>x</sub> > 0 2.5	Ru 650 RuO <sub>x</sub> > 0 0	Rh 554 RhO <sub>1.5</sub> -132 0	Pd 376 PdO -55.4 100	Ag 284 AgO <sub>0.5</sub> -5.6 -	Cd 112 CdO -228 42.2	In 243 InO <sub>1.5</sub> -415 21
Cs 77.6 CsO <sub>0.5</sub> -154 0	Ba 183 BaO -520 0	La 431 LaO <sub>1.5</sub> -853 0	Hf 621 HfO <sub>2</sub> -1088 0	Ta 782 TaO <sub>2.5</sub> -956 0	W 859 WO <sub>3</sub> -764 0	Re 775 ReO <sub>x</sub> > 0 0	Os 788 OsO <sub>x</sub> > 0 0	Ir 670 IrO <sub>x</sub> > 0 0.3	Pt 564 PtO <sub>x</sub> > 0 40.6	Au 368 AuO <sub>x</sub> > 0 100	Hg 65 HgO -58 37.3	Tl 182 TlO <sub>1.5</sub> -106 9.5

Fig. 7.4 Cohesive energy, Gibbs free energy of formation of oxide, and maximum solid solubility with Ag of the metals.

## 7.2.3 Verification of the prediction

W is selected as the surface layer of the Ag film to verify the correctness of the prediction in the last. This is because Ag-W system has been found to exhibit practically complete immiscibility in both liquid and solid states,<sup>151)</sup> and W possesses large free energy for oxide formation ( $\Delta_f G^\circ_{\text{WO}_3} = -764$  kJ/mol),<sup>68)</sup> high cohesive energy (859 kJ/mol),<sup>119)</sup> and low bulk resistivity ( $\rho = 5.3 \mu\Omega$  cm at 293 K).<sup>3)</sup>

### 7.2.3.1 Experimental procedure

The experimental procedure is similar to that of Chapter 4. The pure W (60 nm) and W (5 nm)/Ag (100 nm) films were prepared using RF magnetron sputtering. The as-deposited films were preserved in an air desiccator before annealing. Annealing was conducted at 500 or 600 °C in a lamp-heating furnace for 1 h after evacuation to below  $1.0 \times 10^{-6}$  Torr. In addition, a W (5 nm)/Ag (50 nm) film was deposited using RF magnetron sputtering at room temperature. After deposition, the substrate was not taken out from the sputtering chamber, but sequentially heated to 450 °C (the extreme temperature of the heater fixed to the sputtering chamber) and kept for 1 hour in the evacuation of below  $1.8 \times 10^{-7}$  Torr. Then, the surface morphology of the films was observed by SEM and AFM to evaluate the thermal stability of the W/Ag films, and the electrical resistivity was measured by the four-point probe method.

### 7.2.3.2 Results and discussion

Figure 7.5 shows the SEM images of the W (60 nm) film after annealing at 600 °C, and the W (5 nm)/Ag (100 nm) films before and after annealing. After annealing at 600 °C, the W film still shows very smooth surface morphology. The result of AFM analysis shows that the rms value of the annealed W film is as small as 1.8 nm. Therefore, the good morphological stability of W could be used to confirm the viewpoint that the morphological stability is closely related with free energy for oxide formation and cohesive energy.

The Ag film with 5-nm-thick W surface layer exhibited flat surface before annealing, and only some small voids formed after annealing at 500 °C. Even after annealing at 600 °C, the W (5 nm)/Ag (100 nm) film showed good surface morphology. The rms surface roughness of the W (5 nm)/Ag (100 nm) films after annealing at 500 °C and 600 °C has been measured to be 1.7 nm and 1.9 nm, respectively. Therefore, the excellent effect of the W surface layer on the improvement in the thermal stability of the Ag films is confirmed. In this case, the formation of W oxide passivation layer is considered to play the leading role in suppressing the agglomeration of the Ag film.

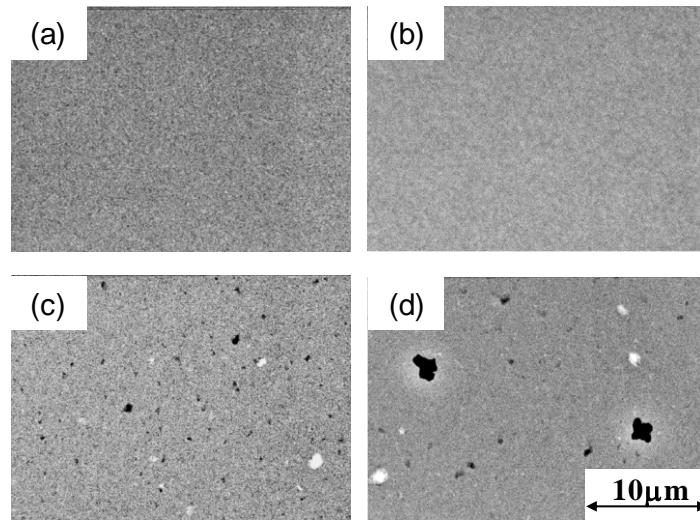


Fig. 7.5 SEM images of (a) W (60 nm) film after annealing at 600 °C, (b) as-deposited W (5 nm)/Ag (100 nm) film, (c) W (5 nm)/Ag (100 nm) film after annealing at 500 °C, and (d) W (5 nm)/Ag (100 nm) film after annealing at 600 °C.

Figure 7.6 shows the SEM images of the Nb (5 nm)/Ag (50 nm) and W (5 nm)/Ag (50 nm) films after annealing in sputtering chamber at 450 °C. The W (5 nm)/Ag (50 nm) film shows a significant improvement in thermal stability as well as the Nb (5 nm)/Ag (50 nm) film. As described in Chapter 4, the evacuation of below  $1.8 \times 10^{-7}$  Torr can prevent the metal thin film from oxidation in the sputtering chamber, even if the temperature is increased to 450 °C. Therefore, it is considered that, just like the Nb surface layer, the W surface layer kept in metallic state during annealing in sputtering chamber, and effectively suppressed the agglomeration of the Ag film.

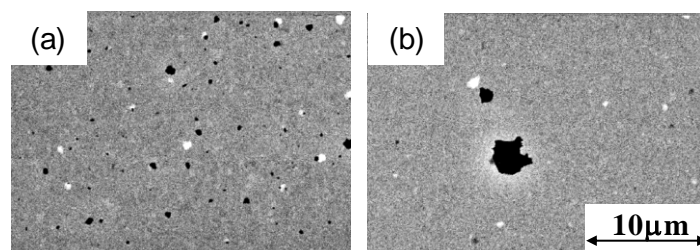


Fig. 7.6 SEM images of the (a) Nb (5 nm)/Ag (50 nm) and (b) W (5 nm)/Ag (50 nm) films after annealing in sputtering chamber at 450 °C.

Figure 7.7 shows the resistivity of the Ag (100 nm) and W (5 nm)/Ag (100 nm) films as a function of annealing temperature. The resistivity of the as-deposited W (5 nm)/Ag film is almost the same as that of the as-deposited Ag film, which is attributed to the low bulk resistivity of W. After annealing at 500 °C, the resistivity of the W (5 nm)/Ag film drops to appropriately 2.0  $\mu\Omega$  cm, mainly owing to the improvement in the crystallinity of Ag. The resistivity of the W (5 nm)/Ag film after annealing at 600 °C is maintained as low as 2.0  $\mu\Omega$  cm, because of the agglomeration suppression caused by the W surface layer.

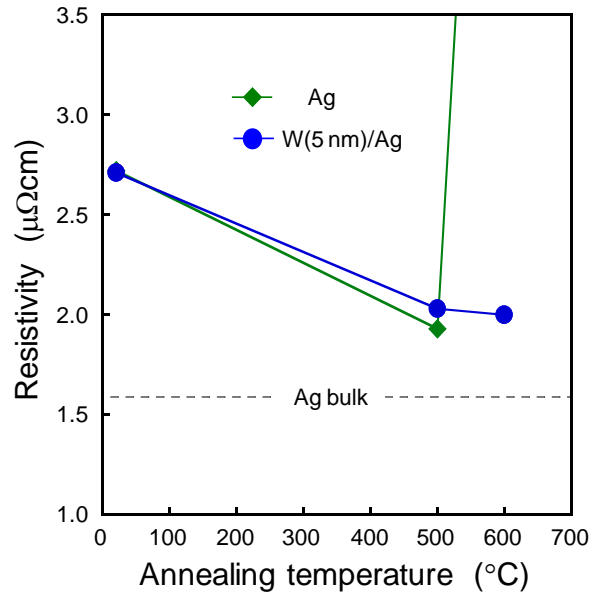


Fig. 7.7 Resistivity of the Ag (100 nm) and W (5 nm)/Ag (100 nm) films after annealing at 600 °C.

#### 7.2.4 Summary

It is considered that the metals with high cohesive energy or large free energy of formation of oxide, and low solid solubility in Ag are appropriate as the surface layers of the Ag films for agglomeration suppression. In addition, the surface layers with low bulk resistivity have little influence on the sheet resistance of the multilayered films. Moreover, the results of using W as the surface layer of Ag film have successfully verified the correctness of the above hypothetical theory.

## 7.3 Appropriate interface layers

### 7.3.1 Comparison of interface layers

Figure 7.8 shows the SEM images and the rms roughness of the Ag/Pd (5 nm), Ag/Ni (5 nm), Ag/Nb (5 nm), and Ag/Ti (5 nm) films after annealing at 600 °C. By comparison, it is found that the largest voids are formed in the Ag/Pd (5 nm) film after annealing at 600 °C, and thus the Ag/Pd (5 nm) film shows the worst surface morphology. Although the size of the voids occurring at the Ag/Ni (5 nm) film is less than a quarter of the size of the voids in the annealed Ag/Pd (5 nm), there are many voids distributed at the surface of the Ag/Ni (5 nm). The Ni interface layer can not effectively suppress the agglomeration of the Ag film. The surface morphology of the Ag films after annealing at 600 °C is improved by introducing the Ti or Nb interface layer. Especially, when the Ti interface layer is inserted, the voids become much fewer and smaller, and the rms surface roughness of the annealed Ag/Ti (5 nm) film is the lowest.

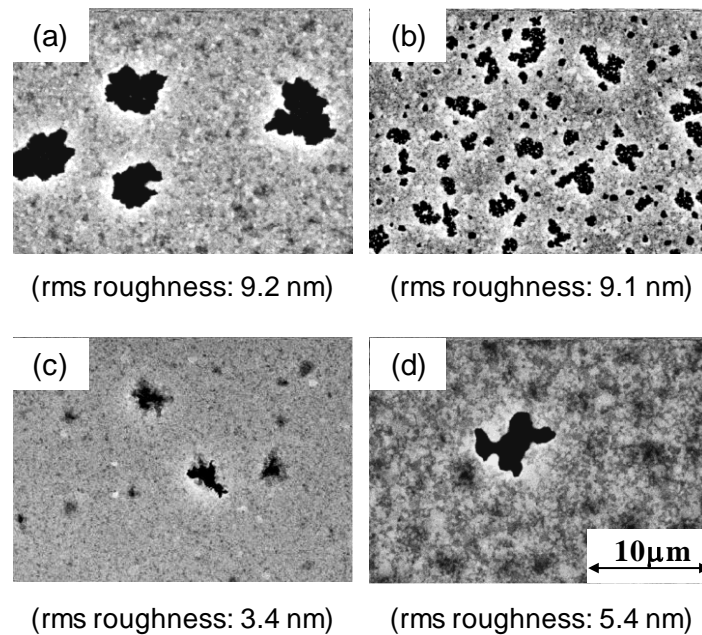


Fig. 7.8 SEM images and rms roughness of Ag (100 nm) films with various interface layers (5 nm) after annealing at 600 °C. (a) Pd, (b) Ni, (c) Ti, and (d) Nb.

Based on the analysis of the previous chapters, it has been considered that there are

two important roles for the interface layer in improving the thermal stability of the Ag films. One is to improve the adhesion of the Ag film to the SiO<sub>2</sub> substrate, and the other is to enhance the crystalline orientation of Ag(111).

Figure 7.9 shows the critical delamination load of the as-deposited Ag/Pd (5 nm), Ag/Ni (5 nm), Ag/Nb (5 nm), and Ag/Ti (5 nm) films, which is used to evaluate the adhesion of the Ag films to the SiO<sub>2</sub> substrates. The Ti, Nb, and Ni interface layers greatly improve the adhesion between the Ag films and the SiO<sub>2</sub> substrates. However, the Pd interface layer had no effect on the adhesion strength of the Ag film. Indeed, the film adhesion correlates well with the free energy for oxide formation.<sup>67)</sup> The novel metals such as Ag and Pd have weak oxides, while Ti, Nb, and Ni have strong ones. Therefore, the Ti, Nb, or Ni interface layer could form both strong metallic bonds to the Ag film and strong covalent bonds to the SiO<sub>2</sub> substrate, and then improve the adhesion of the Ag film to the SiO<sub>2</sub> substrate and decrease the interfacial energy. On the other hand, the larger adhesion of the Ag/Ni film than those of the Ag/Ti and Ag/Nb films is considered to be caused by the higher sputtering power for the deposition of the Ni interface layer, as explained in Chapter 6 in detail.

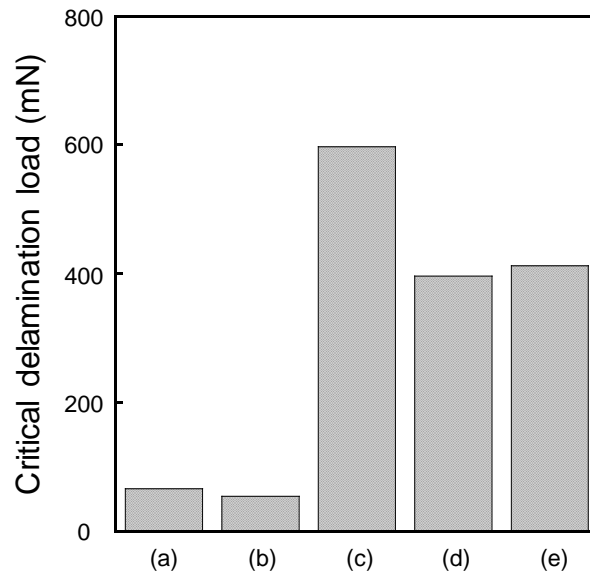
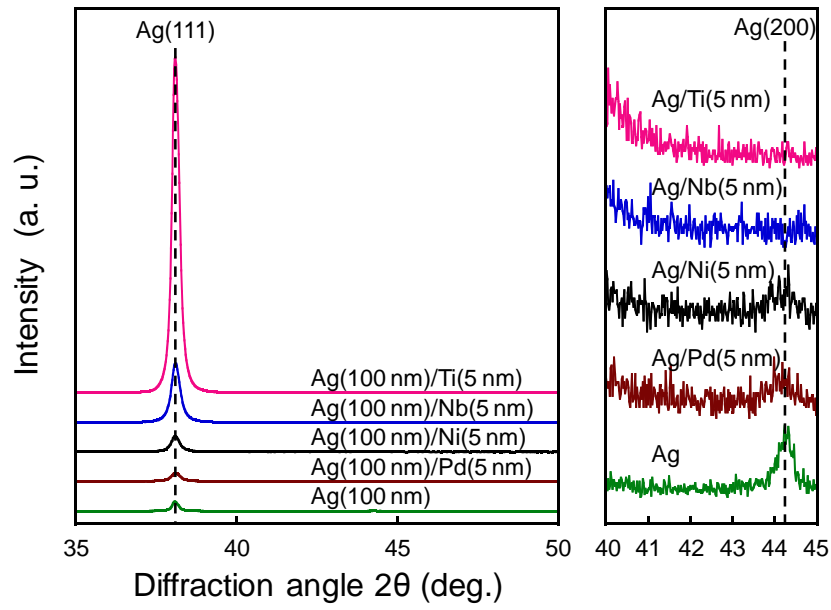
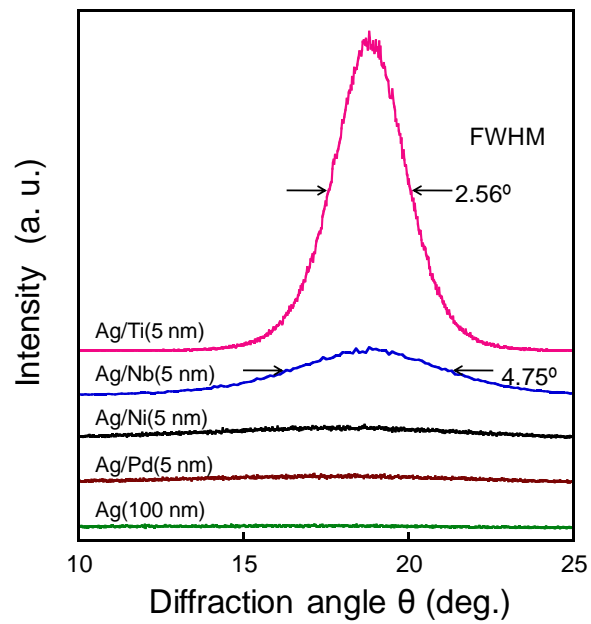


Fig. 7.9 Critical delamination load of the as-deposited (a) Ag (100 nm), (b) Ag (100 nm)/Pd (5 nm), (c) Ag (100 nm)/Ni (5 nm), (d) Ag (100 nm)/Ti (5 nm), and (e) Ag (100 nm)/Nb (5 nm) films.



(a)



(b)

Fig. 7.10 (a) XRD patterns and (b) XRD rocking curves of the as-deposited Ag (100 nm), Ag (100 nm)/Pd (5 nm), Ag (100 nm)/Ni (5 nm), Ag (100 nm) /Nb (5 nm), and Ag (100 nm)/Ti (5 nm) films.

Figure 7.10 shows (a) XRD patterns and (b) XRD rocking curves for Ag(111) of the

as-deposited Ag(100 nm), Ag/Pd (5 nm), Ag/Ni (5 nm), Ag/Nb (5 nm), and Ag/Ti (5 nm) films. It is found that the Ag/Nb (5 nm) and Ag/Ti (5 nm) films show the single orientation of Ag(111), in contrast, the Ag/Pd (5 nm) and Ag/Ni (5 nm) films exhibit the orientations of Ag(111) and Ag(200) as well as the Ag film. The FWHM of the XRD rocking curves is used to evaluate the crystalline orientation of the Ag films. The smaller FWHM is, the higher crystalline orientation of Ag(111) is. Therefore, it is found that the Ag/Ti (5 nm) and Ag/Nb (5 nm) films show very high crystalline orientation of Ag(111), in particular, the Ag/Ti (5 nm) exhibits the highest one.

There are three base types of crystal structures for metals, which are face-centered cubic (fcc), body-centered cubic (bcc), and hexagonal close-packed (hcp).<sup>139)</sup> Ag, Pd, and Ni belong to fcc structure, Ti belongs to hcp structure, and Nb belongs to bcc structure. Although Pd and Ni have the same crystal structure as Ag, the mismatch of lattice constant is too large for Pd(111) or Ni(111) of the interface layers to improve the crystalline orientation of Ag(111) under the deposition condition of this study. The closest-packed planes of fcc(111) and hcp(0002) show the same atomic arrangement that any three neighboring atoms closely link and form an equilateral triangle. As calculated in Chapter 3, the mismatch of axial length for Ag(111) and Ti(0002) is only 1.9%, and hence it is easy for Ag(111) to arrange on Ti(0002). Therefore, the Ag/Ti film shows high crystalline orientation of Ag(111). On the other hand, because the atomic arrangement on the closest-packed planes of fcc(111) and bcc(110) is different, it is difficult for fcc(111) to arrange on bcc(110) unless they meet well with the Nishiyama-Wassermann (NW) or Kurdjumov-Sachs (KS) relationship, which has been described in detail in Chapter 4. As a result, the Nb interface has some effect on the improvement in the crystalline orientation of Ag(111).

Figure 7.11 shows the resistivity of the Ag/Pd (5 nm), Ag/Ni (5 nm), Ag/Nb (5 nm), and Ag/Ti (5 nm) films as a function of annealing temperature. Generally speaking, the introduction of the interface layer would not affect the resistivity of the overcovering Ag film before annealing. However, it has been found that the resistivity of the as-deposited films, such as the Ag/Nb (5 nm) and Ag/Ti (5 nm) films, decreases slightly with enhancing the crystalline orientation of Ag(111). The Ag/Pd (5 nm) film shows a significant increase of the resistivity with increasing the annealing temperature, owing

to the impurity scattering effect caused by the formation of Ag-Pd solid solution. Because the Ag/Ni (5 nm), Ag/Nb (5 nm), and Ag/Ti (5 nm) films kept very continuous and the crystallinity of the Ag films became better after annealing at 500 °C, their resistivity reduces abruptly. After annealing at 600 °C, the resistivity of the Ag films with various interface layers changes with the effects of the interface layers on agglomeration suppression. The Ag/Ti (5 nm) and Ag/Nb (5 nm) films exhibit the lowest resistivity after annealing at 600 °C.

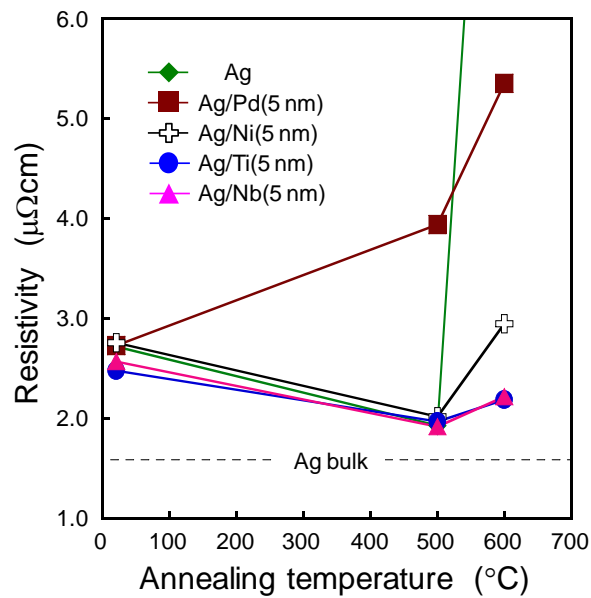


Fig. 7.11 Resistivity of the Ag (100 nm), Ag (100 nm)/Pd (5 nm), Ag (100 nm)/Ni (5 nm), Ag (100 nm)/Ti (5 nm), and Ag (100 nm)/Nb (5 nm) films as a function of annealing temperature.

### 7.3.2 Summary

The appropriate interface layers of the Ag films, such as the Ti nano-layer, not only improve the adhesion of the Ag films to the SiO<sub>2</sub> substrates, but also enhance the crystalline orientation of Ag(111), which are useful for the improvement in the thermal stability of the Ag films. In addition, the improvement in the crystalline orientation of Ag(111) can lead to a slight reduction in the resistivity of the Ag films.

## **Chapter 8 Research Summary and Conclusion**

The general objective of this research work was to suppress the agglomeration of the Ag thin film and maintain its characteristic low resistivity simultaneously, by modifying the structure of Ag thin film with nano-surface layer and/or nano-interface layer. This dissertation has described the effects of Ti, Nb, Pd, and Ni as the surface layer or the interface layer on the thermal stability and the electrical resistivity of the Ag thin films, and concluded what categories of metallic materials are suitable for them. In this chapter, each chapter is summarized, and this research is concluded.

### **8.1 Research summary**

In Chapter 1, the eager expectation of applying the Ag thin films in electronic devices, the problem about the agglomeration of the Ag thin film, and the mechanism and previous solution of Ag agglomeration have been described in detail.

Although the previous solution of alloying Ag films with other metallic elements has improved the thermal stability of the Ag films, the low resistivity was often sacrificed caused by the impurity scattering effect. Therefore, the structural modification of the Ag film with extra thin surface layer and interface layer is expected to achieve both high thermal stability and low resistivity simultaneously.

In Chapter 3, the effects of Ti surface layer and interface layer on the thermal stability and electrical properties of the Ag thin film have been discussed. The Ti surface layer with the thickness of 3 nm has been confirmed to suppress the agglomeration of the Ag film effectively and maintain the low resistivity after annealing at high temperature. The Ti nano-surface layer can easily form passivation layer by natural oxidation, which contributes to effectively suppressing the surface diffusion of the underlying Ag film. Ti is difficult to form solid solution with Ag, which leads to no impurity scattering effect. In addition, the minimum thickness of 3 nm is thin enough and the nano-layer does not affect the resistivity of the body part of Ag. The Ti interface layers with the thickness of 3 nm and above not only improve the adhesion between Ag films and SiO<sub>2</sub> substrates, but also induce the growth of (111) single oriented Ag film, which is considered to be

preferable to improve the thermal stability of the Ag films. Finally, the triple-layer film of Ti (3 nm)/Ag/Ti (3 nm) has been confirmed to be superior to the double-layer films, owing to the combined effect of the Ti surface layer and interface layer.

In Chapter 4, the effects of Nb surface layer and interface layer and the comparison with Ti layers have been discussed. The Nb nano-layer is also easy to form oxide passivation layer by natural oxidation, which is beneficial to the agglomeration suppression. Moreover, the Nb nano-layer in metallic state has been confirmed to have extremely high morphological stability, and it can suppress the agglomeration of the Ag film effectively. The Nb surface layer with low bulk resistivity has very small influence on the sheet resistance of the multilayered Ag film. Therefore, the Nb surface layer is superior to the Ti surface layer, and 5-nm-thick Nb layer has been proved to be an appropriate surface layer. The Nb interface layers with the thickness of 3 nm and above could improve both the adhesion of the Ag films on SiO<sub>2</sub> substrates and the crystalline orientation of Ag(111), which contributes to the improvement in the thermal stability. However, the effect of the Nb interface layers is poorer than the Ti interface layers.

Finally, although the combined effect of the Nb surface layer and interface layer has been approved, the triple-layer structure of Nb (5 nm)/Ag/Ti (3 nm) has been confirmed to be superior to Nb (5 nm)/Ag/Nb (5 nm) and Ti (3 nm)/Ag/Ti (3 nm) films in achieving both good morphological stability and low electrical resistivity. It is indicated that the different materials of more appropriate surface and interface layers can promote a higher thermal stability and a lower resistivity than the same materials of surface and interface layers.

In Chapter 5, the effects of Pd surface layer and interface layer have been discussed. The ease of the formation of Ag-Pd solid solution leads to the significant increase of the resistivity after annealing at high temperature. The Pd surface layer shows poor morphological stability owing to its low free energy of formation of oxide and low cohesive energy, so it has little influence on the agglomeration suppression. The Pd interface layer can not improve the adhesion of the Ag film to the SiO<sub>2</sub> substrate and the crystalline orientation of Ag(111), which result in no obvious improvement in thermal stability. Therefore, Pd is not suitable for the surface layer and the interface layer of the Ag film.

In Chapter 6, the effects of Ni surface layer and interface layer on the thermal stability and electrical properties of the Ag thin film have been discussed. The Ni surface layer remains in metallic state during annealing due to the low free energy for Ni oxide formation. The morphological stability of the metal Ni film is poor owing to the low cohesive energy of Ni. Therefore, the Ni surface layers have failed to adequately suppress the agglomeration of the Ag films. The Ni interface layer can improve the adhesion of the Ag film to the SiO<sub>2</sub> substrate, but can not enhance the crystalline orientation of Ag(111). Therefore, the effect of the Ni interface layer on the improvement in the thermal stability of the Ag films is inferior to the Ti and Nb interface layers.

In Chapter 7, it has been confirmed that the metals with large cohesive energy or large free energy of formation of oxide, low solid solubility in Ag, and low bulk resistivity are appropriate as the surface layers of the Ag films. The appropriate interface layers of the Ag films should not only improve the adhesion of the Ag films to the SiO<sub>2</sub> substrates, but also enhance the crystalline orientation of Ag(111), such as the Ti interface layer.

## **8.2 Conclusion**

This dissertation has presented a better solution of modifying the Ag film with both appropriate surface layer and interface layer for obtaining high thermal stability and low resistivity simultaneously. So far, Nb (5 nm)/Ag/Ti (3 nm) has been confirmed to be the optimum film structure caused by the combined effect of the most appropriate surface layer and interface layer in this study. More importantly, this dissertation has also proposed a theoretical basis for the efficient selection of the appropriate surface layer and interface layer of the Ag film.



## References

- 1) B. Ro: *KiKinzoku no Kagaku* (Chemistry of Noble Metal) (Nikkan Kogyo Shinbunsha, Tokyo, 1987) p. 125 [in Japanese].
- 2) International Centre for Diffraction Data (ICDD), Powder Diffraction File (PDF)-2, Release 2009, reference code 00-089-3722.
- 3) The Chemical Society of Japan: *Kagaku Binran* (Handbook of Chemistry). 4th ed. Vol. 2. (Maruzen, Tokyo, 1993) p. 490 [in Japanese].
- 4) A. Ozaki, M. Nakahara, I. Yasumori, T. Ishimori, and I. Iida: *Kikinzoku Genso no Kagaku to Oyo* (Chemistry and Application of Precious Metal) (Kodansha, Tokyo, 1988) p. 27 [in Japanese].
- 5) Y. Aoshima, M. Miyazaki, K. Sato, Y. Akao, S. Takaki, and K. Adachi: *Jpn. J. Appl. Phys.* **39** (2000) 4884.
- 6) E. Bertran, C. Corbella, M. Vives, A. Pinyol, C. Person, and I. Porqueras: *Solid State Ionics* **165** (2003) 139.
- 7) K. H. Choi, H. J. Nam, J. A. Jeong, S. W. Cho, H. K. Kim, J. W. Kang, D. G. Kim, and W. J. Cho: *Appl. Phys. Lett.* **92** (2008) 223302-1.
- 8) J. A. Jeong, and H. K. Kim: *Sol. Energy Mater. Sol. Cells* **93** (2009) 1801.
- 9) J. A. Jeong, Y. S. Park, and H. K. Kim: *J. Appl. Phys.* **107** (2010) 023111-1.
- 10) Y. Y. Choi, K. H. Choi, H. Lee, H. Lee, J. W. Kang, and H. K. Kim: *Sol. Energy Mater. Sol. Cells* **95** (2011) 1615.
- 11) Y. Zeng, L. Chen, Y. L. Zou, P. A. Nyugen, J. D. Hansen, T. L. Alford: *Materials letters* **45** (2000) 157.
- 12) T. L. Alford, P. Nguyen, Y. Zeng, and J. W. Mayer: *Microelectron. Eng.* **55** (2001) 383.
- 13) M. Hauder, W. Hansch, J. Gstöttner, and D. Schmitt-Landsiedel: *Solid- State Electron.* **47** (2003) 1227.
- 14) W. H. Lee, B. S. Cho, B. J. Kang, J. Y. Kim, and J. G. Lee: *Journal of the Korean Physical Society* **40** (2002) 110.
- 15) O. Akhavan, A. Azarm, A. Z. Moshfegh, and M. A. Bahrevar: *Appl. Surf. Sci.* **252** (2006) 5335.

- 16) S. Strehle, S. Menzel, J. W. Bartha, K. Wetzig: *Microelectron. Eng.* **87** (2010) 180.
- 17) M. Fahland, P. Karlsson, and C. Charton: *Thin Solid Films* **392** (2001) 334.
- 18) M. Girtan: *Sol. Energy Mater. Sol. Cells* **100** (2012) 153.
- 19) A. Rizzo, M. A. Tagliente, M. Alvisi, and S. Scaglione: *Thin Solid Films* **396** (2001) 29.
- 20) X. Sun, and J. Shao: *Appl. Surf. Sci.* **253** (2006) 2093.
- 21) J. C. C. Fan, F. J. Bachner, G. H. Foley, and P. M. Zavracky: *Appl. Phys. Lett.* **25** (1974) 693.
- 22) R. J. Martín-Palma, L. Vázquez, J. M. Martínez-Duart, and Malats-Riera: *Sol. Energy Mater. Sol. Cells* (1998) 55.
- 23) C. Charton, and M. Fahland: *Surf. Coatings Technol.* **174-175** (2003) 181.
- 24) E. Ando, S. Suzuki, N. Aomine, M. Miyazaki, and M. Tada: *Vacuum* **59** (2000) 792.
- 25) Y. Tachibana, K. Kusunoki, and H. Ohsaki: *Vacuum* **74** (2004) 555.
- 26) S. H. Park, K. S. Lee, and A. S. Reddy: *Solid State Sci.* **13** (2011) 1984.
- 27) K. Kato, H. Omoto, and A. Takamatsu: *Thin Solid Films* **520** (2012) 4139.
- 28) J. H. Son, Y. H. Song, H. K. Yu, and J. L. Lee: *Appl. Phys. Lett.* **95** (2009) 062108.
- 29) K. Sugawara, M. Kawamura, Y. Abe and K. Sasaki: *Microelectron. Eng.* **84** (2007) 2476.
- 30) K. Sugawara, Y. Minamide, M. Kawamura, Y. Abe, and K. Sasaki: *Vacuum* **83** (2009) 610.
- 31) Y. Minamide, M. Kawamura, Y. Abe, and K. Sasaki: *Vacuum* **84** (2010) 657.
- 32) M. Kawamura, M. Yamaguchi, Y. Abe, and K. Sasaki: *Microelectron. Eng.* **82** (2005) 277.
- 33) J. Nakai, Y. Tauchi, H. Fujii, T. Satou, T. Onishi, and K. Takagi: *Kobe Steel Engineering Reports* **52** (2002) 12 [in Japanese].
- 34) A. Elshabini-Riad, and F. D. Barlow: *Thin Film Technology Handbook* (McGraw-Hill, New York, 1997) p. 9-1.
- 35) R. Yamamoto: *Taso Hakumaku to Zairyo Kaihatsu* (Multilayer Thin Film and Material Development) (Shiemushi, Tokyo, 2002) pp. 94-100 [in Japanese].
- 36) M. Mashita, and M. Yoshida: *Hakumaku Kougaku Handobukku* (Handbook of Film Technology) (Kodansha, Tokyo, 1998) p. 382 [in Japanese].

- 37) M. Mashita, T. Hata, and I. Kojima: *Zukai Hakumaku Gijyutsu* (Thin Film Technology Illustrated) (Baifukan, Tokyo, 1999) pp.135-138 [in Japanese].
- 38) S. P. Murarka: *Metallization Theory and Practice for VLSI and ULSI* (Butterworth-Heinemann, Massachusetts, 1993) pp. 2-6.
- 39) K. Maeda: *Hajimete no Handotai Nano Purosesu* (Beginner's Book for semiconductor nano-process) (Kogyo Chosakai, Tokyo, 2000) p.193 [in Japanese].
- 40) A. K. Sinha, J. A. Cooper, and H. J. Levinstein, IEEE Trans. Electron Devices Letter **EDL 3** (1982) 90.
- 41) M. M. Mitan, T. L. Alford, and J. W. Mayer: Thin Solid Films **434** (2003) 258.
- 42) M. Hauder, W. Hansch, J. Gstöttner, and D. Schmitt-Landsiedel: Microelectron. Eng. **60** (2002) 51.
- 43) S. P. Murarka, and S. W. Hymes: Crit. Rev. Solid State Mater. Sci. **20** (1995) 87.
- 44) G. J. Exarhos, and X. D. Zhou: Thin Solid Films **515** (2007) 7025.
- 45) M. Mashita, T. Hata, and I. Kojima: *Zukai Hakumaku Gijyutsu* (Thin Film Technology Illustrated) (Baifukan, Tokyo, 1999) pp.163-169 [in Japanese].
- 46) The 166th Committee on Photonic and Electronic Oxide of JSPS: *Tomei Dodenmaku no Gijyutsu* (Transparent Conducting Film Technology) (Ohmsha, Tokyo, 1999) pp. 15-45 [in Japanese].
- 47) H. Han, D. Adams, J. W. Mayer, and T. L. Alford: J. Appl. Phys. **98** (2005) 083705.
- 48) M. Bender, W. Seelig, C. Daube, H. Frankenberger, B. Ocker, and J. Stollenwerk: Thin Solid Films **326** (1998) 67.
- 49) K. H. Choi, J. Y. Kim, Y. S. Lee, and H. J. Kim: Thin Solid Films **341** (1999) 152.
- 50) Y. S. Jung, Y. W. Choi, H. C. Lee, and D. W. Lee: Thin Solid Films **440** (2003) 278.
- 51) A. Klöppel, B. Meyer, and J. Trube: Thin Solid Films **392** (2001) 311.
- 52) Y. Guan, M. A. Matin, and T. M. Stephen: Electron. Lett. **39** (2002) 826.
- 53) C. Cuillén, and J. Herrero: Opt. Commun. **282** (2009) 574.
- 54) D. R. Sahu, S. Y. Lin, and J. L. Huang: Appl. Surf. Sci. **252** (2005) 7509.
- 55) C. Cuillén, and J. Herrero: Phys. Status Solid A **207** (2010) 1563.
- 56) C. Cuillén, and J. Herrero: Thin Solid Films **520** (2011) 1.
- 57) S. K. Sharma, and J. Spitz: Thin Solid Films **56** (1979) L 13.

- 58) S. K. Sharma, and J. Spitz: *Thin Solid Films* **65** (1980) 339.
- 59) S. K. Sharma, and J. Spitz: *J. Mater. Sci.* **16** (1981) 535.
- 60) R. Dannenberg, E. A. Stach, J. R. Groza, and B. J. Dresser: *Thin Solid Films* **370** (2000) 54.
- 61) R. Dannenberg, E. Stach, J. R. Groza, and B. J. Dresser: *Thin Solid Films* **379** (2000) 133.
- 62) H. C. Kim, T. L. Alford, and D. R. Allee: *Appl. Phys. Lett.* **81** (2002) 4287.
- 63) T. L. Alford, L. Chen, and K. S. Cadre: *Thin Solid Films* **429** (2003) 248.
- 64) K. S. Gadre, and T. L. Alford: *J. Appl. Phys.* **93** (2003) 919.
- 65) Z. Wang, X. Cai, Q. Chen, and P. K. Chu: *Thin Solid Films* **515** (2007) 3146.
- 66) H. C. Kim, N. D. Theodore, and T. L. Alford: *J. Appl. Phys.* **95** (2004) 5180.
- 67) C. H. F. Peden, K. B. Kidd, and N. D. Shinn: *J. Vac. Sci. Technol.* **A9** (1991) 1518.
- 68) The Chemical Society of Japan: *Kagaku Binran* (Handbook of Chemistry) (Maruzen, Tokyo, 2003) 5th ed., Vol. 2, pp. 291-300 [in Japanese].
- 69) M. Kawamura, Y. Inami, Y. Abe, and K. Sasaki: *Jpn. J. Appl. Phys.* **47** (2008) 8917.
- 70) D. L. Smith: *Thin-Film Deposition: Principles and practice* (McGraw-Hill, Boston, 1995) pp. 170-177.
- 71) T. L. Alford, D. Adams, T. Laursen, and B. M. Ullrich: *Appl. Phys. Lett.* **68** (1996) 3251.
- 72) H. C. Kim and T. L. Alford: *J. Appl. Phys.* **94** (2003) 5393.
- 73) E. E. Glickman, V. Bogush, A. Inberg, Y. Shacham-Diamand, and N. Croitoru: *Microelectron. Eng.* **70** (2003) 495.
- 74) S. H. Cha, H. C. Koo, and J. J. Kim: *J. Electrochem. Soc.* **152** (2005) C388.
- 75) M. Kawamura, Z. Zhang, R. Kiyono, and Y. Abe: *vacuum* **87** (2013) 222.
- 76) N. Sawaki: *Denshi Tsushin Zairyo Kogaku* (Electronic Communication Materials Engineering) (Baifukan, Tokyo, 1995) p. 38 [in Japanese].
- 77) K. Miyake: *Hakumaku no Kiso Gijyutu* (Basic Technology of Thin Films) (Asakurasyoten, Tokyo, 1968) p. 23 [in Japanese].
- 78) M. Kawamura, D. Fukuda, Y. Inami, Y. Abe, and K. Sasaki: *J. Vac. Sci. Technol. A* **27** (2009) 975.
- 79) H. Kobayashi, and N. Hosokawa: *Buhin Debaisu no tame no Hakumaku Gijyutsu*

- Nyumon* (Introduction to Thin-Film Technology for Component and Device) (Sogodenshi Shuppansha, Tokyo, 1992) pp. 195-202 [in Japanese].
- 80) S. Berg, H. O. Blom, T. Larsson, and C. Nender: *J. Vac. Sci. Technol.* **A 5 (2)** (1987) 202.
- 81) D. Depla, and R. D. Gryse: *Surface and Coatings Technol.* **183** (2004) 190.
- 82) D. L. Smith: *Thin-Film Deposition: Principles and practice* (McGraw-Hill, Boston, 1995) p. 559.
- 83) H. Kobayashi, and N. Hosokawa: *Buhin Debaisu no tame no Hakumaku Gijyutsu Nyumon* (Introduction to Thin-Film Technology for Component and Device) (Sogodenshi Shuppansha, Tokyo, 1992) p.126 [in Japanese].
- 84) H. Kobayashi, and N. Hosokawa: *Buhin Debaisu no tame no Hakumaku Gijyutsu Nyumon* (Introduction to Thin-Film Technology for Component and Device) (Sogodenshi Shuppansha, Tokyo, 1992) p.134 [in Japanese].
- 85) H. Naganuma, Y. Kubo, and S. Nakahama: *Aluminum Finishing Society of KinKi* **146** (1990) 7 [in Japanese].
- 86) M. Kato: *X-Sen Bunko Bunseki* (X-ray Spectroscopic Analysis) (Uchidarokakuho, Tokyo, 1998) pp. 213-219 [in Japanese].
- 87) J. I. Goldstein, D. E. Newbury, P. Echlin, D. C. Joy, C. Fiori, and E. Lifshin: *Scanning Electron Microscopy and X-ray Microanalysis* (Plenum Press, New York, 1981) p. 3.
- 88) S. Morita: *Genshikanryoku Kenbikyo no Subete* (All for Atomic Force Microscope) (Kogyochosakai, Tokyo, 1995) p. 22 [in Japanese].
- 89) The Japan Society of Applied Physics / Molecular Electronics and Bioelectronics: *Yukibunshi no STM / AFM* (STM / AFM for Organic Molecules) (Kyoritz, Tokyo, 1993) pp. 26-36 [in Japanese].
- 90) D. L. Smith: *Thin-Film Deposition: Principles and practice* (McGraw-Hill, Boston, 1995) p. 576.
- 91) H. Kobayashi, and N. Hosokawa: *Buhin Debaisu no tame no Hakumaku Gijyutsu Nyumon* (Introduction to Thin-Film Technology for Component and Device) (Sogodenshi Shuppansha, Tokyo, 1992) p.151 [in Japanese].
- 92) The Surface Science Society of Japan: *X-Sen Kodenshi Bunkoho* (X-ray

- Photoelectron Spectroscopy) (Maruzen, Tokyo, 1998) p. 5 [in Japanese].
- 93) S. Baba, A. Kikuchi, and A. Kinbara: *J. Vac. Sci. Technol.* **A5** (1987) 1860.
- 94) A. Guinier: *X-Ray Diffraction in Crystals, Imperfect Crystals, and Amorphous Bodies* (Dover Publications, New York, 1994) p.95.
- 95) P. Scherrer: *Gött Nachr* **2** (1918) 98.
- 96) B. D. Cullity, and S. R. Stock: *Elements of X-Ray Diffraction* (Prentice Hall, New Jersey, 2001) 3th ed. p. 170.
- 97) D. L. Smith: *Thin-Film Deposition: Principles and practice* (McGraw-Hill, Boston, 1995) p. 249.
- 98) H. Toraya, H. Hibino, T. Ida, and N. Kuwano: Annual Report of the Ceramics Research Laboratory Nagoya Institute of Technology **2** (2002) 31 [in Japanese].
- 99) The Chemical Society of Japan: *Kagaku Binran* (Handbook of Chemistry) (Maruzen, Tokyo, 1993) 4th ed., Vol. 2, p. 291-293 [in Japanese].
- 100) E. Z. Luo, S. Heun, M. Kennedy, J. Wollschlager, M. Henzler: *Phys. Rev. B* **49** (1994) 4858.
- 101) J. F. Moulder, W. F. Stickle, P. E. Sobol, and K. D. Bomben: *Handbook of X-ray photoelectron spectroscopy* (Perkin-Elmer, Eden Prairie, 1992) p. 231.
- 102) T. B. Massalski, H. Okamoto, P. R. Subramanian, and L. Kacprzak: *Binary Alloy Phase Diagrams* (ASM International, Ohio, 1990) Vol. 1, p. 106.
- 103) Y. Li, X. Sun, H. Li, S. Wang, and Y. Wei: *Powder Technol.* **25** (2009) 149.
- 104) G. F. Malgas, D. Adams, T. L. Alford, and J. W. Mayer: *Thin Solid Films* **467** (2004) 267.
- 105) M. Mashita, and M. Yoshida: *Hakumaku Kougaku Handobukku* (Handbook of Film Technology) (Kodansha, Tokyo, 1998) p. 380 [in Japanese].
- 106) S. Gonda, Y. Nakai, E. Maruyama, and K. Wasa: *Hakumaku no Sakusei Hyoka to Sono Oyo Gijyutu* (Handbook of Preparation, Evaluation, and Application of Films) (Koji Tekunosisutemu, Tokyo, 1986) p. 28
- 107) A. Elshabini-Riad, and F. D. Barlow: *Thin Film Technology Handbook* (McGraw-Hill, New York, 1998) p.3-11.
- 108) International Centre for Diffraction Data (ICDD), Powder Diffraction File (PDF)-2, Release 2009, reference code 00-089-5009.

- 109) J. A. Venables: *Introduction to Surface and Thin Film Processes* (Cambridge University Press, Cambridge, 2000) p. 199.
- 110) M. Arbab: *Thin Solid Films* **381** (2001) 15.
- 111) Y. Tsuda, H. Omoto, K. Tanaka and H. Ohsaki: *Thin Solid Films* **502** (2006) 223.
- 112) Y. Zeng, Y. L. Zou, and T. L. Alford: *Thin Solid Films* **307** (1997) 89.
- 113) M. R. Baren: *Bull. Alloy Phase Diagrams* **10** (1989) 640.
- 114) J. F. Moulder, W. F. Stickle, P. E. Sobol, and K. D. Bomben: *Handbook of X-ray Photoelectron Spectroscopy* (Perkin-Elmer, Eden Prairie, MN, 1992) p. 229.
- 115) Surface Science Society of Japan: *X-Sen Kodenshi Bunkoho* (X-ray Photoelectron Spectroscopy) (Maruzen, Tokyo, 1998) p. 219 [in Japanese].
- 116) S. C. Vanithakumari, and K. K. Nanda: *Phys. Lett. A* **372** (2008) 6930.
- 117) W. H. Qi: *Mater. Lett.* **60** (2006) 1678.
- 118) G. S. Chang, J. H. Son, T. G. Kim, K. H. Chae, C. N. Whang, J. I. Jeong, Y. P. Lee: *Thin Solid Films* **341** (1999) 234.
- 119) C. Kittel: *Introduction to Solid State Physics* (Wiley, New Caledonia, 2005) 8th ed., p. 50.
- 120) S. K. Sharma, and J. Spitz: *Thin Solid Films* **56** (1979) L17.
- 121) H. Jiang, T. J. Klemmer, J. A. Barnard, W. D. Doyle, and E. A. Payzant: *Thin Solid Films* **315** (1998) 13.
- 122) O. Hellwig, K. Theis-Bröhl, G. Wilhelmi, A. Stierle, and H. Zabel: *Surf. Sci.* **398** (1998) 379.
- 123) Y. Gotoh, M. Uwaha, and I. Arai: *Appl. Surf. Sci.* **33** (1988) 443.
- 124) E. Bauer, and J. Van der Merwe: *Phys. Rev. B* **33** (1986) 3657.
- 125) R. Ramirez, A. Rahman, and I. Schuller: *Phys. Rev. B* **30** (1984) 6208.
- 126) Y. Gotoh, and H. Fukuda: *Surf. Sci.* **223** (1989) 315.
- 127) G. Wassermann: *Arch. Eisenhüttenwesen* **126** (1933) 647.
- 128) Z. Nishiyama: *Sci. Rep. Tohoku Univ.* **23** (1934) 638.
- 129) G. Kurdjumov, and G. Sachs: *Z. Phys.* **64** (1930) 325.
- 130) C. Kittel: *Introduction to Solid State Physics* (Wiley, New Caledonia, 2005) 8th ed., p. 21.
- 131) T. B. Massalski, H. Okamoto, P. R. Subramanian, and L. Kacprzak: *Binary Alloy*

- Phase Diagrams* (ASM International, Ohio, 1990) Vol. 1, p. 74.
- 132) J. F. Moulder, W. F. Stickle, P. E. Sobol, and K. D. Bomben: *Handbook of X-ray Photoelectron Spectroscopy* (Perkin-Elmer, Eden Prairie, MN, 1992) p. 230.
- 133) International Centre for Diffraction Data (ICDD), Powder Diffraction File (PDF)-2, Release 2009, reference code 00-089-4897.
- 134) M. Lukaszewski, K. Klimek, and A. Czerwiński: *J. Electroanal. Chem.* **637** (2009) 13.
- 135) S. T. Marshall, S. K. Satija, B. D. Vogt, and J. W. Medlin: *Appl. Phys. Lett.* **92** (2008) 153503.
- 136) D. L. Smith: *Thin-Film Deposition: Principles and practice* (McGraw-Hill, Boston, 1995) p.199.
- 137) T. Asamaki: *Chobisai Kako no Kiso* (Fundamentals of Microfabrication) (Nikkan Kogyo Shinbunsha, Tokyo, 2001) pp. 115-120 [in Japanese].
- 138) T. B. Massalski, H. Okamoto, P. R. Subramanian, and L. Kacprzak: *Binary Alloy Phase Diagrams* (ASM International, Ohio, 1990) Vol. 1, p. 65.
- 139) O. Nittono: *Zairyo no Kagaku to Kogaku 1* (Materials Science and Engineering An Introduction) (Baifukan, Tokyo, 2002) 5th ed., pp. 40-43 [in Japanese].
- 140) International Centre for Diffraction Data (ICDD), Powder Diffraction File (PDF)-2, Release 2009, reference code 00-087-0712.
- 141) C. Chambon, A. Coati, and Y. Garreau: *Surf. Sci.* **602** (2008) 2363.
- 142) J. Zhang, H. Xin, and X. Wei: *Appl. Surf. Sci.* **246** (2005) 14.
- 143) E. Hristova, V. G. Grigoryan, and M. Springborg: *Surf. Sci.* **603** (2009) 3339.
- 144) J. H. Son, Y. H. Song, H. K. Yu, and J. L. Lee: *Appl. Phys. Lett.* **95** (2009) 062108.
- 145) Y. Okayama, K. Takesako, H. Kose, and K. Kawabata: 46th Union Conference on Vacuum, 2006, p. 159 [in Japanese].
- 146) Y. Levinsky: *Pressure Dependent Phase Diagrams of Binary Alloys* (ASM International, Ohio, 1997) Vol. 2, pp. 1450-1459.
- 147) F. Maglia, G. Spinolo, and U. Anselmi-Tamburini: *Solid State Sci.* **11** (2009) 1686.
- 148) K. Miyake: *Hakumaku no Kiso Gijyutu* (Basic Technology of Thin Films) (Asakurasyoten, Tokyo, 1968) p. 261 [in Japanese].
- 149) T. Asamaki: *Chobisai Kako no Kiso* (Fundamentals of Microfabrication) (Nikkan

Kogyo Shinbunsha, Tokyo, 2001) p. 222 [in Japanese].

150) T. B. Massalski, H. Okamoto, P. R. Subramanian, and L. Kacprzak: *Binary Alloy Phase Diagrams* (ASM International, Ohio, 1990) Vol. 1, pp. 61-106.

151) T. B. Massalski, H. Okamoto, P. R. Subramanian, and L. Kacprzak: *Binary Alloy Phase Diagrams* (ASM International, Ohio, 1990) Vol. 1, p. 113.



## **Achievements of this research**

### **Journal Papers**

- 1) M. Kawamura, Z. Zhang, R. Kiyono, and Y. Abe: “Thermal stability and electrical properties of Ag-Ti films and Ti/Ag/Ti films prepared by sputtering”, *Vacuum* **87** (2013) 222.
- 2) Z. Zhang, M. Kawamura, Y. Abe, and K. H. Kim: “Effects of Nb surface and Ti interface layers on thermal stability and electrical resistivity of Ag thin films”, *Jpn. J. Appl. Phys.* **51** (2012) 085802.
- 3) Z. Zhang, M. Kawamura, Y. Abe, and K. H. Kim: “Important properties for surface layer of Ag film”, submitted to *Jpn. J. Appl. Phys.*

### **International Conference**

- 1) M. Kawamura, Z. Zhang, R. Kiyono, and Y. Abe: “Thermal stability and electrical properties of Ag-Ti films and Ti/Ag/Ti films prepared by sputtering”, 11th International Symposium on Sputtering & Plasma Processes, Kyoto, Japan (2011.7)
- 2) Z. Zhang, M. Kawamura, Y. Abe, and K. H. Kim: “Comparison of thermal stability and electrical resistivity of Ag thin films with different nano-surface layers”, International Union of Materials Research Society-International Conference in Asia 2012, Busan, Korea (2012.8)

### **Domestic Conference**

- 1) Z. Zhang, M. Kawamura, Y. Abe, and K. H. Kim: “Morphological stability and electrical property of Ag thin films with Ti nano-layers”, 表面技術協会・第124回講演大会, 名古屋 (2011.9)

2) Z. Zhang, M. Kawamura, Y. Abe, and K. H. Kim: “Nb 及び Ti ナノレイヤーを積層させた高安定 Ag 薄膜構造の最適化”, 表面技術協会・第 126 回講演大会, 室蘭 (2012.9)

## Others

1) Y. Matsumura, Z. Zhang, M. Kawamura, Y. Abe, and K. H. Kim: “Nb ナノレイヤーを積層させた Ag 薄膜の作製とその熱的安定性”, 化学系学協会北海道支部・2012 年冬季研究発表会, 札幌 (2012.2)

2) Y. Matsumura, M. Okitsu, Z. Zhang, M. Kawamura, Y. Abe, and K. H. Kim: “Nb ナノレイヤーを表面に積層させた Ag 薄膜の作製とその熱的安定性”, 表面技術協会・第 126 回講演大会, 室蘭 (2012.9)

## Acknowledgments

I would like to start by thanking Professor Midori Kawamura, my thesis supervisor, for the valuable and constant support that she has given me in the past two years. Professor Kawamura received me into her lab, Electronic Materials Laboratory in Kitami institute of Technology, when I was in a dilemma on continuing my doctoral study two years ago. She has patiently taught me a lot from the first day of working in her lab, given me much advice about my research, and always encouraged me to try my best to graduate in time. In the last few months, she has carefully corrected my dissertation, and provided many valuable comments for me, which contributed to the smooth completion of my dissertation. Professor Kawamura is very kind to people, and conscientious about her work. Her attitude towards life and work will have a profound impact on my later life. I have felt honored to study under Prof. Kawamura.

I am grateful to Professor Yoshio Abe, my vice-supervisor. Professor Abe is an academically rigorous and experienced scientist. He has always shared his experience with me, and given me a lot of suggestions on my research reports and publications. Moreover, the help and support from him are also indispensable for the completion of my dissertation. I have been really lucky to learn so much from Prof. Abe.

I would also like to thank the rest of my thesis committee for their support. Professor Shinji Watanabe, Professor Keijiro Hiraga, and Associate Professor Hidenobu Itoh have provided me with invaluable advice and comments on my research.

This work would not have been possible without the support of Professor Kiyoshi Aoki, Associate Professor Kazuhiro Ishikawa, Assistant Professor Hideto Yanagisawa, Assistant Professor Kyung Ho Kim, and the technicians of Instrumental Analysis Center, Mr. Misao Yamane, Mr. Sho Tokuda, and Mr. Hideaki Tokuni. Thank you very much for your support. In addition, I want to express my thanks to my research group for their hard work. They have helped me to accumulate a treasure trove of data and experience and save a lot of valuable time for the writing of this dissertation.

Finally, I would like to deeply thank Ms. Tokiko Murayama, my Japanese friend, for everything she has done for my family. Thanks also to my mother and aunts, Tianyan Zheng, Lihua Tang, and Tianjie Zheng for taking good care of my baby in Japan during

my busiest months. In particular, I sincerely thank my wife, Ning Li, for her unending support and love.